Thèse présentée par

SAMUEL MEULÉ

Université du Québec à Rimouski

UNIVERSITÉ LAVAL

McGill

pour l'obtention du grade de

DOCTEUR DE L'UNIVERSITÉ DE LA MÉDITERRANÉE
SPÉCIALITÉ SCIENCES DE L'ENVIRONNEMENT MARIN

&

DOCTEUR DE L'UNIVERSITÉ DU QUÉBEC À RIMOUSKI
CONJOINTEMENT AUX UNIVERSITÉS DE LAVAL ET DE MCGILL
SPÉCIALITÉ OCÉANOGRAPHIE

PROCESSUS MIS EN JEU DANS L'ÉVOLUTION
MORPHO-DYNAMIQUE
DE ROBERT BANK (DELTA DU FRASER) :

OBSERVATION ET MODÉLISATION
HYDRODYNAMIQUES ET SÉDIMENTAIRES

Le jury est composé de :

Professeur Ivan DEKEYSER
Docteur Xavier DURRIEU DE MADRON
Professeur Arnaud HEQUETTE (Rapporteur)
Professeur Phil HILL
Professeur Vladimir KOUTITONSKY
Docteur Christel PINAZO
Professeur Mireille PROVANSAL (Rapporteur)

UNIVERSITÉ DU QUÉBEC À RIMOUSKI
Service de la bibliothèque

Avertissement

Résumé

Roberts Bank couvre le delta intertidal entre le bras principal du fleuve Fraser et la pointe du Cap Roberts en Colombie Britannique, Canada. Sous la pression du développement urbain et la modification du régime sédimentaire, cette plage de sable fin est soumise à une érosion significative. L'identification des forces hydrodynamiques, leur importance et leur interaction permettent de déterminer les zones de transport, et donc la stabilité de Roberts Bank. Deux périodes de mesures associées à des phases de modélisation de la houle et des courants ont été effectuées lors de ce travail. La première période de mesure, entre le 29 juin et le 8 juillet 2001, a permis l'identification de processus hydrodynamiques et sédimentaires associés aux forts courants de marée présents le long de Roberts Bank. La seconde phase de mesure, entre le 1er mars et le 26 mars 2002, a permis d'étudier les processus de remise en suspension associés à la houle. Des phases de modélisation ont été menées à partir des connaissances acquises sur le terrain, afin d'affiner la compréhension des processus sédimentaires et notamment les interactions houle - courant - sédiment. Les mécanismes, mis en évidence dans cette étude, participent au façonnage de Roberts Bank, contribuent à son érosion et à la mise en place de nouvelles structures sédimentaires. Les courants de flot de marée vont initier la création de nuages de resuspension de sédiment depuis le fond. En eau peu profonde, la composante "*onshore*" du courant de marée induit un transport à la côte, tandis qu'en eau plus profonde une faible composante "*offshore*" du courant peut favoriser un transport au large le long de la pente. Les chenaux, les dunes subaquatiques et les surfaces d'érosion affleurantes fournissent une rugosité de fond suffisante à la génération de turbulence et donc de nuages de sédiment en suspension. Lors de la marée de jusant, les sédiments resuspendus en eau peu profonde, sont transportés vers le large à partir d'un panache de surface et par les chenaux deltaïques. Une forte turbulence favorisera un processus dit de "sédimentation convective induite par un mélange turbulent " ("*mixing-induced convective sedimentation*"). Le comportement des vagues de tempête qui se propagent sur la partie supérieure de la pente du Delta du Fraser dépend du marnage, de l'incidence de propagation et de la morphologie sous-marine. Ces facteurs contrôlent une divergence dans le transport sédimentaire au niveau de la rupture de pente deltaïque. A marée haute, le transport sédimentaire sera essentiellement "*onshore*".

REMERCIEMENTS

3

SOMMAIRE

159

1. INTRODUCTION

1.1. Contexte

Les deltas représentent des environnements sédimentaires complexes qui font la liaison entre la terre et la mer et qui induisent une grande gamme d'environnements de dépôts marins (Tetzlaff et Harbaugh 1989). C'est une zone dynamique affectée par la plupart des processus existants dans la zone de "surf" et ceux de la partie interne du plateau continental. De plus, il s'agit d'une zone où le régime sédimentaire peut être largement perturbé par de nombreuses pressions anthropiques. L'étude de la dynamique des sédiments, où de nombreux processus instationnaires sont mis en jeu et interagissent, est donc particulièrement complexe. S'il est difficile de les représenter avec exactitude, il est néanmoins possible de les mettre en évidence. La modélisation est un outil qui permet d'évaluer les paramètres moteurs de l'hydrodynamisme côtier. En ce sens, la compréhension du système en est facilitée. Dans le cas du delta du Fraser, la connaissance des processus sédimentaires est nécessaire pour assurer la faisabilité de projets d'ingénierie côtière et pour comprendre la sensibilité environnementale de cette zone. Economiquement la partie Sud du delta du Fraser, Roberts Bank, est d'importance majeure. Des câbles électriques hautes tensions, qui alimentent l'île de Vancouver depuis le continent, traversent le marais, le front et la pente deltaïque sur la portion Sud. Le plus grand port d'exportation de charbon du Canada et le terminal de ferry de Tsawwassen sont également présents dans cette zone. La connaissance d'un maximum de paramètres concernant la stabilité sédimentaire de la zone apparaît donc vitale.

Ce travail de thèse fait partie d'un vaste projet "The Georgia Basin Geohazards Initiative"[*], piloté par la Commission Géologique du Canada (Pacifique), qui a pour but de comprendre les processus géologiques et les conditions qui représentent un risque pour la population canadienne habitant autour du Bassin de Géorgie. Ce projet cherche à fournir une connaissance géoscientifique afin d'aider à prendre des décisions efficaces sur l'environnement et la gestion des ressources dans le Bassin de Géorgie.

1.2. Présentation du site d'étude

Le delta du Fraser est situé au Sud-Ouest de la Colombie Britannique, sur la côte Pacifique du Canada (Fig. I-1). C'est un delta de taille modérée (1000 km^2), en bordure du détroit de Géorgie (séparant le continent de l'île de Vancouver). Vancouver et sa périphérie urbaine (1.9 millions d'habitants en 1998) se sont développés en bordure de mer. Le Fraser est le système fluvial le plus important de la côte Pacifique du Canada. Son delta, datant de moins de 10 000 ans, s'est construit par la migration continue des chenaux de distribution pendant l'événement postglaciaire de l'Holocène (fin de la glaciation du Wisconsin). La région est soumise à des tensions de cisaillements résultant de la subduction de la plaque de Juan de Fuca sous la plaque nord-américaine. La vitesse de déplacement des deux plaques l'une par rapport à l'autre (le taux de convergence) est approximativement de 45 mm an^{-1} (Mosher *et al.* 2000). Ces caractères géophysiques font de la Colombie Britannique l'une des régions les plus sismiquement actives du Canada (Rogers 1994 ; Cassidy et Rogers 1999).

---

[*] http://www.pgc.nrcan.gc.ca/marine/gbgi/index_e.htm
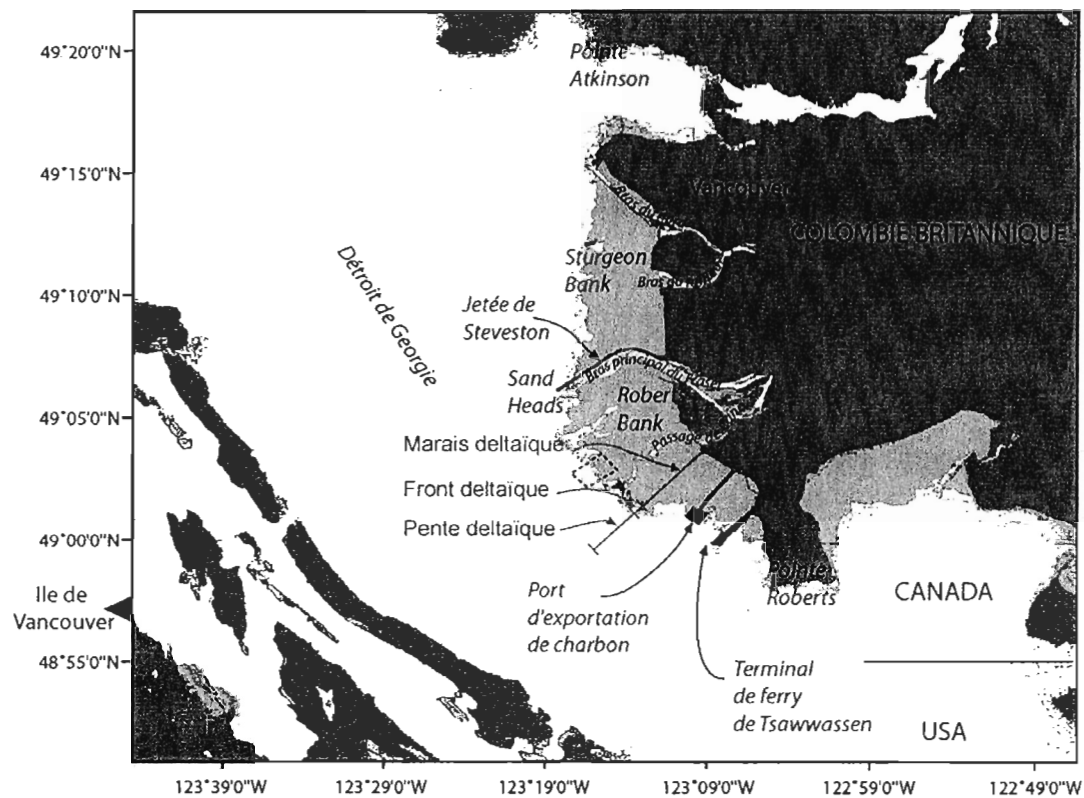
Figure I-1 : Localisation du site d'étude, et indication des différentes zones morphologiques. La zone pointillée représente la zone d'étude choisie pour l'article 2 (chapitre 3) et l'article 3 (chapitre 4).

1.2.1. Caractéristiques morphologiques

Le site étudié est Roberts Bank (Fig. I-1) qui couvre le delta intertidal entre le bras principal du Fraser et la pointe du cap Robert. Notre intérêt porte sur les zones morphologiques suivantes du delta sous-marin (Hart *et al.* 1995) :

- Le front deltaïque qui s'étend jusqu'à approximativement 10 m de profondeur, est à la limite du marais deltaïque.

- La pente deltaïque, typiquement de 2 à 3°, est une portion du delta sous le front deltaïque qui évolue au large jusque dans la zone du prodelta (typiquement <1°). Il est donc compris entre 10 m et 100 m de profondeur sur Roberts Bank.

Des chenaux sous-marins actifs et inactifs incisent le front deltaïque ainsi que la pente deltaïque entre 30 m et 90 m, augmentant localement la pente jusqu'à 23°. Ces chenaux sous-marins sont créés par l'apport de masse d'eau et de sédiments depuis les différents bras et chenaux de distribution (Hart *et al.* 1992). Roberts Bank est ainsi limité au Nord par le chenal sous-marin de Sand Heads (Fig. I-1 ; Hart et Barrie 1997) juste à l'embouchure du bras principal du Fraser. Plus au Sud, le chenal de Roberts Bank, actuellement en phase de remplissage, s'est formé à partir d'un chenal de distribution actuellement abandonné. Trois autres petits chenaux sous-marins sont situés au large du passage dit de Canoë. Les deux chenaux les plus au Nord sont inactifs tandis que celui au Sud reste actif. Différents auteurs (Mathews et Shepard 1962 ; Evoy *et al.* 1993 ; Kostaschuk *et al.* 1995) suggèrent que ces chenaux sous-marins servent de conduit pour le transport sédimentaire. Des courants turbides créés par des glissements à l'embouchure d'un passage ou d'un bras fluviatile vont former des levées et aider à la construction du prodelta.

En plus des complexes stratigraphiques liés à l'embouchure du fleuve (Hart 1993), une structure massive faillée résultant de processus d'instabilité de la pente se situe le long de la pente de Roberts Bank au niveau du port d'exportation de charbon (Hart *et al.* 1992 ; Hart *et al.* 1995 ; Currie et Mosher 1996 ; Christian *et al.* 1997 ; Hart *et al.* 1998). L'instabilité de la zone est augmentée par l'existence de forts gradients de pente et par la présence de gaz dans la colonne sédimentaire (Hart *et al.* 1992).

1.2.2. Caractéristiques hydrosédimentaires.

La morphologie du fond sous-marin et les corps sédimentaires reflètent l'interaction de différents processus de transport sédimentaire et de déformation. La charge annuelle du fleuve (environ $17.3.10^6$ tonnes) consiste en 65 % de silt et 35 % de sables, principalement transportés lors des crues printanières. A l'embouchure du bras principal et pour des conditions de basse mer en vives eaux, l'écoulement relativement fort provenant du fleuve génère des courants dirigés vers le large dont la vitesse est de 2.5 m s^{-1}. Pour de faibles marées, ces courants sont modérés et ont des vitesses de l'ordre de 1 à 1.5 m^{-1}. Lors du flot, le panache sédimentaire est dévié vers le Nord en direction de Sturgeon Bank sous l'effet de l'action de la force de Coriolis (Thomson 1981). Le sable fin est transporté en suspension avec la fraction argileuse. Même lors du jusant, les faibles courants sont contrebalancés par l'action de la force de Coriolis. Les sédiments fins sont alors transportés au large. Les sédiments les plus grossiers sont transportés par charriage et déposés près de l'embouchure.

Trois jetées ont été construites à travers la zone intertidale du delta (Fig. I-1) au cours des 40 dernières années. Ces constructions ont créé des barrières permanentes aux transports sédimentaires et aux courants de marée à travers et le long du front. Le plus gros port

d'exportation de charbon du Canada ainsi que le terminal de ferry de Tsawwassen ont été construits à la limite du marais deltaïque. La jetée de Steveston au Nord du chenal principal empêche la décharge sédimentaire de s'effectuer directement à l'embouchure. La partie Sud du bras principal n'est pas construite, et le transport de sédiment grossier par charriage peut s'effectuer à proximité dans la partie supérieure de la pente. Le transport en suspension est favorisé par la chenalisation du fleuve et le transport "*longshore*" (le long de la côte) est limité (Milliman 1980). Plusieurs auteurs (Hart et Barrie 1997 ; Barrie et Currie 2000) concluent que l'endiguage de l'embouchure a créé une zone d'instabilité et de glissements. Ils montrent également que la quantité de sédiments sableux actuellement entrant dans Roberts Bank est négligeable sauf à l'embouchure même.

La partie supérieure du front deltaïque de Roberts Bank est composée de sables fins à moyens. La granulométrie médiane est de 3 ϕ (unité phi) ou 0.125 mm (Barrie et Currie, 2000). Les sables fins sont progressivement remplacés par des silts vers l'estuaire. Sur la pente, les sédiments sont de plus en plus fins vers le large, à l'exception du Sud de Roberts Bank où le sable domine (Barrie, 2000). Mathews et Shepard (1962) ont observé, à l'embouchure du Fraser, à l'aide de prélèvements en bouteilles Niskin, la présence de larges pourcentages de fibres végétales et de mica, parfois associés en agrégats. Les taux de sédimentation et d'érosion basés sur les mesures de Cs^{137} par Hart *et al.* (1998) montrent que la pente et le prodelta de Roberts Bank sont des zones de non-déposition ou d'érosion. Enfin un large champ de dunes sous-marines recouvre le complexe faillé de Roberts Bank (Currie et Mosher 1996 ; Hart *et al.* 1998 ; Barrie 2000). Les dunes migrent vers le Nord-Ouest et Kostaschuk *et al.* (1995) suggèrent alors que la seule source de sédiment disponible provient de l'érosion du lit sédimentaire et du clapage local (notamment vers les terminaux au Sud).

Les mécanismes qui contrôlent le transport, l'érosion et le dépôt sédimentaire sont directement influencés par les paramètres hydrodynamiques eux-mêmes hautement variables. Puisque l'érosion est dominante au niveau du front et de la partie supérieure de la pente deltaïque, les processus majeurs sont les courants de marée, les courants de houle, ou ceux générés par les effets du vent.

Huit constituants tidaux sont important dans le détroit de Géorgie : M2, S2, N2 et K2 pour les harmoniques semidiurnes ; K1, O1, P1, et Q1 pour les harmoniques diurnes. A la pointe Atkinson au Nord, les 8 constituants comptent pour 86.1 % du marnage (Foreman *et al.* 1995). Le delta est donc une zone macrotidale avec une marée mixte semidiurne ($F = \dfrac{K_1 + O_1}{M_2 + S_2} = 1.4166$ à la pointe Sheringham au Sud du détroit de Géorgie). Le marnage moyen est de 2.9 m au niveau du front deltaïque (Thomson 1981) et le marnage de vives eaux est de 5 m et de 2 m pour les marées de mortes eaux. La marée entre par le détroit de Géorgie à travers le détroit de Juan de Fuca. Les courants sont fortement bidirectionnels et coulent le long du delta vers le Nord-Ouest pour les courants de flot et vers le Sud-Est pour le jusant. Les maxima des courants de flot se produisent 1h50 avant les marées hautes et ceux des courants de jusant 1h30 avant les marées basses (Thomson 1981). Les données de Kostaschuk *et al.* (1995), recueillies à 90 m de profondeur, indiquent des courants de flot avec une vitesse moyenne de 33 cm s^{-1}, plus amples et de plus longue durée que les courants de jusant, d'une vitesse moyenne de 29 cm s^{-1}. Les courants de flot sont parfois persistants particulièrement lors de faibles renverses. Les dunes sous-marines présentes semblent être générées par les courants de flot.

Bien que le Delta du Fraser ne soit pas exposé à de fortes houles de tempête, les courants oscillatoires peuvent être assez forts pour jouer un rôle important sur le littoral. Mathews et

Shepard (1962) ont observé que le *"shoaling"* (augmentation de la cambrure des vagues par effet de haut fond) était ainsi prononcé au niveau de Roberts Bank. Luternauer et Murray (1973) indiquent que la rupture de pente à 9 m, séparant le marais du front deltaïque, coïncide à la fois avec la profondeur maximale d'influence de la houle et avec le maximum d'intensité de turbulence générée par les courants. De la même manière, Hart et Barrie (1997) et Hart *et al.* (1995) ont observé que, dans ce secteur, la limite du front deltaïque (10 m de fond) est sous l'influence de la houle incidente. De plus, la partie extérieure du marais deltaïque présente un trait de côte rectiligne ce qui suggère un refaçonnage morphologique par la houle.

Dans un recueil de données de 1967 à 1990, Hill et Davidson (2002) indiquent qu'à Sand Heads les directions de vent les plus fréquentes sont de secteurs Est, Sud-Est et Nord-Ouest, représentant 65 % des observations totales. La fréquence des vents de Sud et d'Ouest représente chacune 10 % du temps, tandis que la fréquence des vents de Nord, Nord-Est et Sud-Ouest représente moins de 5 %. Sur une base annuelle les vents les plus intenses soufflent du Nord-Ouest et du Sud-Est, et les faibles vents proviennent des secteurs Nord et Nord-Est. Lors de forts coups de vents, l'intensité des courants induits est supérieure à celle des courants de marée. Le panache fluvial peut alors être dévié vers le Sud du détroit de Géorgie.

La proximité de l'île de Vancouver limite le fetch c'est à dire la distance sur laquelle des vagues peuvent être générées dans une zone de vent. En conséquence les fetchs les plus longs sont au Nord-Ouest (80 km). Le fetch du Sud-Est est de 45 km, celui d'Ouest de 20 km et celui du Sud de 16 km. En conséquence les champs de houle avec une hauteur significative (Hs) supérieure à 1 m sont générés principalement du Sud-Est ou Nord-Ouest, avec quelques contributions du S et de l'Ouest. La moyenne des hauteurs significatives pour ces houles est

de 1.3 m. Thomson (1981) a toutefois observé au large de Roberts Bank des hauteurs maximales de houle supérieures à 3 m et de période 5 s. Les vagues dont la période est supérieure à 6 s proviennent du Nord-Ouest. La hauteur significative moyenne pour ces houles est de 0.3 m tandis que le pic de période est de 6.8 s. Ces deux conditions de tempête (hauteurs importantes - courtes périodes et périodes importantes - faibles hauteurs) représentent 6% des conditions dans l'année.

1.3. Objectifs de l'étude

Plusieurs études antérieures (i.e. Kostaschuk *et al.* 1995 ; Hart et Barrie 1997 ; Hart *et al.* 1998 ; Barrie et Currie 2000) montrent que la plage de Roberts Bank, sans nouvel apport de sédiment est soumise à une érosion significative. Des constats semblables existent pour d'autres deltas, notamment pour le Nil (White et El Asmar 1999) et le Mississippi (Penland *et al.* 1988), confortant la notion qu'une réduction des apports sédimentaires et une subduction de la zone deltaïque entraînent une transgression marine et une rapide érosion du delta. En se basant sur une revue bibliographique, Hill (2001) développa, dans un modèle conceptuel, différentes hypothèses pour expliquer la dynamique sédimentaire au niveau du front deltaïque du delta du Fraser. Ces hypothèses, non exclusives ont permis de structurer la méthodologie de travail de cette thèse autour de phases d'échantillonnages et de modélisation.

L'objectif spécifique de cette thèse est l'étude des mécanismes de mise en suspension et de transport des sédiments fins de Roberts Bank. Cette étude a donc cherché à répondre à deux types de questions ; (1) identification fondamentale des forces hydrodynamiques, de leur importance et de leur interaction ; (2) détermination des zones de transport, d'accrétion et

d'érosion, et la détermination de la stabilité de Roberts Bank sous la pression du développement urbain et de la modification du régime sédimentaire.

Dans ce cadre, les mesures de terrain et les travaux de modélisation ont été menés parallèlement afin de bénéficier des informations complémentaires des deux approches tout au long de l'étude et ainsi établir un lien entre une approche à l'échelle des processus et une approche à moyenne échelle de la dynamique sédimentaire de la zone.

Les modèles mathématiques jouent un rôle de plus en plus prépondérant dans les géosciences et notamment dans la prise de décisions scientifiques et politiques. L'utilisation de techniques de modélisation est motivée par la volonté de déterminer plus précisemment les paramètres importants. Elles permettent également de compléter notre compréhension des processus de la dynamique sédimentaire. Les modèles hydrodynamiques (PARAB + COURAN) développés en convention avec l'entreprise PRINCIPIA (Marcer et Robin 1996, Meulé *et al.* 2001 - Annexe A2) ont été adaptés à l'environnement Linux (Mandrake 8.2) qui constitue le système d'exploitation le plus adapté en programmation pour des ordinateurs de type PC. Les calculs au niveau sédimentaire ont été effectués sous scripts Matlab regroupés dans un modèle appelé DYSCO[†] (*"DYnamique Sédimentaire CÔtière"*). Le déploiement en parallèle de plusieurs ordinateurs du Centre d'Océanologie de Marseille sous la forme d'un système centralisé dit Cluster a permis d'augmenter les capacités de calcul pour l'exécution des simulations.

Pour l'étude et la compréhension de certains processus liés à la propagation de la houle et afin de calibrer certains coefficients (par exemple, la calibration du coefficient de déferlement en

---

[†] Le modèle DYSCO sous Matlab 7 est également disponible à l'adresse internet suivante:
http://samuel.meule.free.fr/ dossier thèse/download/dysco
login: article ; password: transfer.1

fonction de la présence d'ondes infragravitaires), des données provenant du site de la plage de Sète dans le cadre du Programme National d'Environnement Côtier (PNEC – ART7) ont été analysées. Ce travail ne faisant pas partie du travail majeur de cette thèse, le lecteur est invité à se référer à l'article de l'annexe A3 et au résumé de l'annexe A4.

Cette thèse s'articule autour de 3 articles scientifiques (chapitres 2 à 4) avec des introductions, des méthodologies, des résultats et des discussions indépendantes. Les objectifs de chacun de ces articles sont définis dans la section qui suit. Le chapitre 5 synthétise les différents processus discutés dans chaque article.

1.3.1. Les processus de transport de sédiments en suspension sous influence de la marée au niveau du front du delta du Fraser.

L'influence de la marée sur la morphologie et les faciès deltaïques sont bien documentés (par exemple Kostaschuk *et al.* 1998 ; Rose et Thorne 2001) cependant la plupart des recherches ont porté sur la dynamique estuarienne des chenaux de distribution et leurs embouchures. Dans un contexte macrotidal, les forts courants de marée influencent typiquement l'ensemble d'un front deltaïque, créant des zones de dépôts actifs, de non déposition et/ou d'érosion. Les modifications de la pente deltaïque sont importantes pour la stabilité du système. L'objectif du premier article (chapitre 2) est donc de décrire les mécanismes de mise en suspension et de transport des sédiments en relation avec une forte circulation de marée dans la partie supérieure de la pente deltaïque du delta du Fraser, au niveau de Roberts Bank.

Ce travail a été mené en parallèle avec de récentes études d'imagerie par sonar multifaisceaux qui ont considérablement affiné l'identification et la compréhension de la morphologie de la

pente deltaïque et des structures sédimentaires présentes (Hart *et al.* 1992 ; Kostaschuk *et al.* 1992 ; Evoy *et al.* 1993 ; Hart 1993 ; Hart *et al.* 1995 ; Kostaschuk *et al.* 1995 ; Currie et Mosher 1996 ; Christian *et al.* 1997 ; Evoy *et al.* 1997 ; Hart et Barrie 1997 ; Hart *et al.* 1998 ; Luternauer *et al.* 1998 ; Barrie 2000). Carle et Hill (2004 submitted) présentent une analyse détaillée de ces structures. La présence de chenaux sous-marins, incisant le delta, conduit à un haut degré de variabilité longshore dans le régime du transport sédimentaire. La mise en évidence de l'importance des mouvements *"cross-shore"* (transversale à la côte) se fait donc par l'observation de l'hydrodynamisme aux niveaux des chenaux actifs et des chenaux abandonnés. Des structures morphologiques de plus petite dimension telles que des dunes sous-marines 2-D ou 3-D, des dunes isolées et des surfaces d'érosion affleurantes recouvrent la plupart de la pente deltaïque indiquant une forte dynamique sédimentaire.

L'étude présentée dans le premier article (chapitre 2) a été menée essentiellement en utilisant un courantomètre profileur acoustique (ADCP) de coque. L'ADCP mesure l'effet Doppler rétro-diffusé par les particules en suspension dans la colonne d'eau. Il permet ainsi une estimation des vitesses de courants à de multiples niveaux de la colonne d'eau et fournit une excellente résolution spatiale des circulations côtières comme cela a déjà été montré dans différentes études réalisées dans des embouchures d'estuaires (i.e. Valle-Levinson *et al.* 1998 ; Kincaid *et al.* 2003). Trois stratégies d'échantillonnage ont été appliquées sur l'ensemble du site de Roberts Bank :

- 2 avec le navire en déplacement, soit le long des isobathes de 10 m et 20 m, soit le long d'une des 5 "boîtes prédéfinies" découpant Roberts Bank entre 5 m et 60 m de profondeur (Fig. II-1).
- 1 en station fixe pendant 24h.

L'intensité du signal rétro-diffusé de l'ADCP a été utilisée comme indicateur des concentrations de particules. La perte du signal par atténuation dans l'eau a été prise en compte afin d'avoir une approche qualitative de la dynamique sédimentaire. Les principaux avantages des ADCP, pour les mesures hydrodynamiques et sédimentaires, sont qu'ils sont non intrusifs, et qu'ils permettent des mesures référencées par rapport au fond avec une haute résolution spatiale et temporelle.

1.3.2. Dynamique de la houle et des vagues de vent sur Roberts Bank : processus et modélisation.

Dans un contexte macrotidal, plusieurs observations montrent que Roberts Bank pourrait être également fortement remanié par la houle. L'érosion de Roberts Bank entraîne une divergence du transport sédimentaire dans la zone de déferlement entre la partie extérieure du marais deltaïque et la pente deltaïque. Les processus décrits dans les modèles conceptuels de Hill (2001) et de Swift et Thorne (1991) confirment cette observation. Les courants oscillatoires asymétriques présents pendant les périodes de beau temps tendent à accentuer le transport sédimentaire vers la côte. Le transport "*offshore*" (dirigé au large ou dans la direction de la pente) dans la zone de "*shoaling*" peut être dû à un "*set-up*" de tempête (surélévation du niveau marin d'ordre dynamique) combinés à des courants de "*downwelling*" (c'est à dire liés à une plongée d'eau). La houle peut donc avoir un rôle prépondérant dans la dynamique sédimentaire et une zone d'étude a été choisie là où un remaniement morphologique par la houle pourrait être vraisemblablement observé. Cette zone littorale est centrée sur Roberts Bank (figure I-1). Il s'agit d'une zone rectiligne, non incisée par des chenaux sous-marins, assez éloignée des terminaux portuaires et de l'embouchure.

Dans le deuxième article (chapitre 3) des données de terrain sont présentées en parrallèle à des résultats numériques obtenus à l'aide d'un modèle de propagation d'une houle monochromatique, ceci afin de comprendre l'impact des tempêtes sur le transport sédimentaire littoral. Une station de mesure (Birch *et al.* 2003) a été immergée sur Roberts Bank dans approximativement 12 m de profondeur entre le 1er et le 26 mars 2002. Vitesse orbitale et pression ont été enregistrées à partir d'un courantomètre-houlographe Marsh McBirney et d'un profileur acoustique Aquadopp Nortek équipé d'un capteur de pression. En faisant l'hypothèse que le système naturel de vagues est une superposition de plusieurs houles d'Airy (approximation linéaire du 1er ordre), une analyse spectrale a été menée sur les mesures de pressions converties en dénivellation de la surface libre (Horikawa 1988). Les caractéristiques des vagues sont ainsi extraites. Les directions de propagation sont calculées par une analyse spectrale croisée des données temporelles de pression et de vitesse orbitale.

Le modèle de houle (PARAB) développé en convention avec l'entreprise PRINCIPIA (Marcer et Robin 1996 ; Meulé *et al.* 2001) a été utilisé. Dans ce modèle, le comportement d'une houle monochromatique, unidirectionnelle à l'approche de la côte est traduite par l'équation différentielle partielle de Berkhoff (Berkhoff 1972) sous une forme parabolisée (Radder 1979). La bathymétrie de la portion subtidale, utilisée dans cette étude, a été extraite de la base de données des sonars multifaisceaux de la Commission Géologique du Canada. La grille a été tournée afin d'orienter le trait de côté en haut de la grille. La bathymétrie a été ensuite extrapolée sur la partie supérieure du marais deltaïque à partir d'une triangulation de Delaunay (Petrie et Kenny, 1990).

1.3.3. Processus sédimentaires sur le front du delta du Fraser : mesures de terrain et modélisation.

Une particule de sable déposée sur le fond ne peut être mise en mouvement que si les forces hydrodynamiques qui agissent sur elle sont supérieures aux forces stabilisatrices (pesanteur et cohésion des grains). Les différentes forces hydrodynamiques vont induire des contraintes de cisaillement sur les sédiments et permettre leur transport. L'étude de ces phénomènes est donc importante, notamment lors de la combinaison des houles et des courants, durant les conditions de tempête.

Le $3^{ème}$ article (chapitre 4) examine la relation entre le transport sédimentaire et les mouvements combinés des courants oscillatoires et des courants de marée. Cette étude fait suite aux mesures décrites précédemment ($2^{ème}$ article, chapitre 3). Les courants ont été mesurés en un point à 0.8 m du fond par le courantomètre Marsh McBirney et dans la colonne d'eau (18 cellules de 0.5 m) par un profileur acoustique Nortek Aquadopp. Les concentrations de sédiments en suspension ont été mesurées par des capteurs optiques (OBS) à 0.3 m et 1 m du fond. Le signal rétro-diffusé du profileur a également été calibré afin d'estimer les concentrations de sédiment en suspension dans la colonne d'eau.

Le modèle COURAN, développé en convention avec PRINCIPIA (Marcer et Robin 1996 ; Meulé *et al.* 2001), a été utilisé afin de simuler la courantologie pendant les situations de tempête. Ce modèle de type Saint-Venant résulte de l'intégration sur la verticale des équations de Navier-Stokes instationnaires. Les caractéristiques de vagues en sortie du modèle PARAB ($2^{ème}$ article - chapitre 3) ont permis l'implémentation du modèle hydrodynamique. Le

couplage de ces différents modèles a été facilité par la mise en place automatisée des conditions limites[‡].

A partir des mesures de terrain et des résultats issus de la modélisation de la houle et des courants, les vitesses de cisaillement induites par la houle ($u*_w$), par les courants ($u*_c$) ou par l'interaction non linéaire des deux mouvements ($u*_{cw}$) ont été calculées afin d'identifier plus spécifiquement l'importance de chacun des processus sur la remise en suspension. Les calculs ont été effectués sous script Matlab regroupé dans un modèle appelé DYSCO *("Dynamique Sédimentaire CÔtière")*

[‡] Le code en fortran 77 de détection automatique des conditions limites est disponible à l'adresse internet suivante:
http://samuel.meule.free.fr/   dossier thèse/download/condition limite
login: article ; password: transfer.1

2. SUSPENDED SEDIMENT TRANSPORT PROCESSES ON THE FRONT OF THE TIDE-INFLUENCED FRASER RIVER DELTA, BRITISH COLUMBIA, CANADA.

SAMUEL MEULÉ [A,B], PHILIP R. HILL [A], CHRISTEL PINAZO [B]

[A] NATURAL RESOURCES CANADA, GEOLOGICAL SURVEY OF CANADA - PACIFIC, 9860 WEST SAANICH ROAD, P.O. BOX 6000, SIDNEY, B.C., V8L 4B2, CANADA. EMAIL: sam.meule@nrcan.gc.ca

[B] LABORATOIRE D'OCÉANOGRAPHIE ET DE BIOGÉOCHIMIE, UMR 6535 CNRS/UNIVERSITÉ DE LA MÉDITERRANÉE, OSU/CENTRE D'OCÉANOLOGIE DE MARSEILLE, STATION MARINE D'ENDOUME, CHEMIN DE LA BATTERIE DES LIONS, 13007 MARSEILLE, FRANCE. EMAIL: samuel.meule@com.univ-mrs.fr

Abstract

In order to describe the mechanics of suspension and transport of sediments related to strong tidal circulation on the upper delta slope of the Fraser River delta, a downward-looking ADCP, mounted on a moving vessel, was used to determine current velocity. In addition, the backscatter intensity was used as an indication of particle concentration. Tidal currents were found to be strongly bi-directional, flowing along the isobaths. The maximum flood flow is stronger and of longer duration than the ebb flow. The slack water at both high and low tide exhibits remnant flow structures possible resulting from large-scale flow separation in the vicinity of the Fraser River mouth. Around maximum flood flow, channels, subaqueous dunes and outcropping beds provide significant bed roughness and turbulence to create clouds of resuspended sediment from the bottom. In shallow water, the induced net transport is onshore while in deeper water, a weak component of offshore flow favours down-slope transport. Offshore sediment transport occurs over the ebbing tide in a surface plume originating from shallow water resuspension and tidal creek outflow. Sedimentation by mixing-induced convective sedimentation is favoured by the strong turbulence.

Keywords: ADCP, Tidal current, Backscatter, Resuspension, off-shore sediment transport.

2.1. Introduction

Deltas represent a complex of sedimentary environments that link land and sea and involve deposition in a range of marine environments (Tetzlaff and Harbaugh 1989). The influence of tides on delta morphology and facies has been well documented (i.e. Kostaschuk *et al.* 1998; Rose and Thorne 2001) but most research has been directed at the estuarine dynamics of distributary channels and their mouths. In macrotidal settings, strong tidal currents typically influence the entire front of the delta, resulting in areas of active sediment deposition, non-deposition and/or erosion. Modifications to the delta slope are important to the stability of the system. In the case of the Fraser River delta, knowledge of the sedimentary processes active on the delta front is needed to address the suitability of specific areas for civil engineering projects, and to understand the ecological sensitivity of deltaic environments. The objective of this paper is to describe the mechanics of suspension and transport of sediments related to strong tidal circulation on the upper delta slope of the Fraser River delta.

A feature of this work is the use of acoustic current profiling instruments. Acoustic Doppler Current Profiler (ADCP) uses the Doppler frequency shift of particles in the water column to determine current velocity at multiple levels within the water column. In addition, the backscatter intensity can be used as an indication of particle concentration. Underway ADCP surveys, where a downward-looking ADCP is mounted on a moving vessel, can provide excellent spatial resolution of current circulation, as shown in several recent studies at the mouth of major estuaries (i.e. Valle-Levinson *et al.* 1998; Kincaid *et al.* 2003). The main advantages of ADCP's for both hydrodynamic and sediment measurements are that they are non-intrusive, bed referenced and have high spatial and temporal resolution.
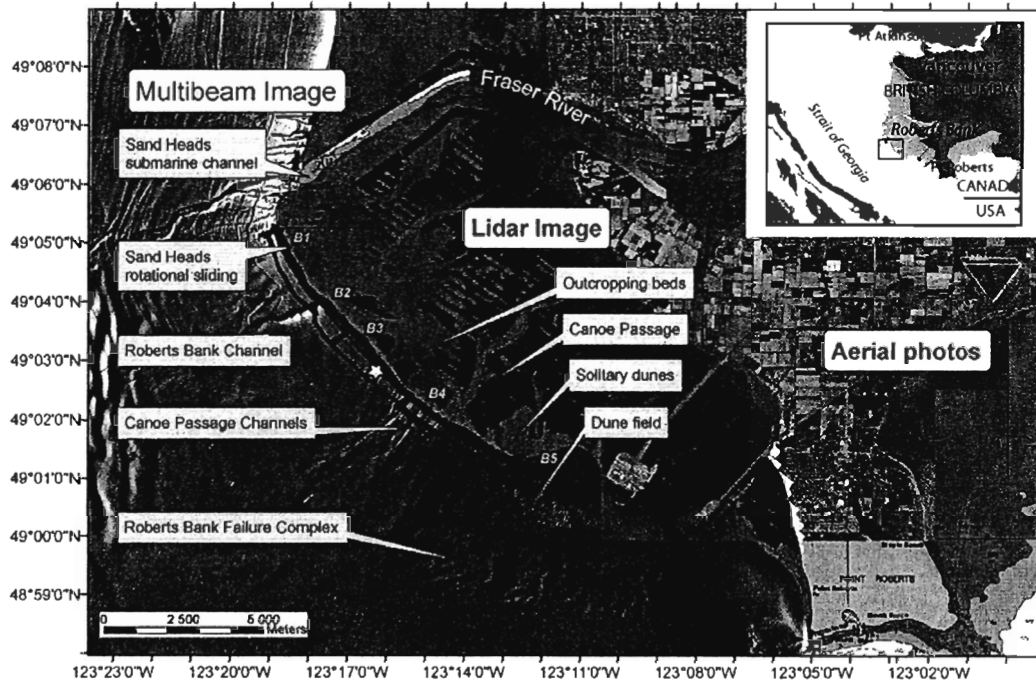
Figure II-1: Map showing the study area on Roberts Bank, Fraser Delta, British Columbia, Canada. The multibeam bathymetry and LIDAR are shown superimposed on a nautical chart. The survey area was divided into five sub- regions of different size between water depths of 5 and 60 m (black boxes B1 to B5). ADCP profiles were measured continuously around each box. In addition, a 24-hr station was occupied in 25 m depth on July 5 represented by a white star.

2.2. *Background*

The Fraser River delta (Fig. II-1), on the southwest coast of British Columbia, Canada, is a moderate-sized delta (1000 km^2). The post-glacial delta was built by progradation into the 300 m deep Strait of Georgia (separating the British Columbia mainland from Vancouver Island). The relative sea level rise in the area has been at a near eustatic rate of 0.36 to 2 mm y^{-1} since 1910 (Clague 1998). Vancouver and its urban areas (1998 population: 1.9 million) lie in close proximity. Roberts Bank is the area of intertidal delta between the Main Arm channel and Point Roberts headland. Following (Hart *et al.* 1995), the delta front is defined from the seaward limit of the tidal flat to approximately 10 m depth. The delta slope, typically 2-3 ° but locally over 23 °, is the portion of the delta between 10 m and 100 m water depth.

2.2.1. Patterns of sedimentation and erosion

Strong tidal currents flow along the delta front and slope, with the flood tide flowing generally south to north and the ebb tide flowing north to south. The sediment plume from the mouth of the main channel is frequently pushed north towards the Sturgeon Bank slope by the Coriolis effect acting on inertial river flow, combined with the dominant flood tide (Thomson 1981). Fine sand is transported in suspension with the mud fraction. During the weaker ebb tide, the fine sediment is transported offshore as the Coriolis force deflects the southeasterly ebb flow. The delta front and upper delta slope of the delta consist of fine to medium sands (Barrie and Currie 2000). The fine sand changes progressively to silt across the intertidal zone. On the delta slope, sediments fine progressively seaward on Sturgeon Bank and off the

29

main channel mouth, but coarsen well onto the delta slope on southern Roberts Bank, becoming finer-grained only at the base of slope (Barrie 2000).

Two causeways and a channel-training jetty have been built across the extensive intertidal estuary of the delta in the last 70 years. These features create permanent barriers to sediment transport and tidal flow across and along the delta front and upper delta slope. Several authors (Hart and Barrie 1997; Barrie and Currie 2000) have concluded that since the Main Arm is no longer free to migrate, the sea floor seaward of the river mouth can be expected to be a zone of ongoing slope instability and that sand supply is only significant at the mouth of Main Arm. Patterns of sedimentation and erosion based on ^{137}Cs measurements made by Hart *et al.* (1998) showed that the Roberts Bank delta slope and is either largely non-depositional.

2.2.2. Roberts Bank slope morphology

Recently obtained multibeam imagery (Fig. II-1) has added considerable insight to previous accounts of delta slope morphology and sediment transport features (Hart *et al.* 1992; Kostaschuk *et al.* 1992; Evoy *et al.* 1993; Hart 1993; Hart *et al.* 1995; Kostaschuk *et al.* 1995; Currie and Mosher 1996; Christian *et al.* 1997; Evoy *et al.* 1997; Hart and Barrie 1997; Hart *et al.* 1998; Luternauer *et al.* 1998; Barrie 2000). A brief review of the morphology is presented here. Further details on the sediment transport features can be found in Carle and Hill (2004 submitted).

The Roberts Bank delta slope is bounded to the north by the Sand Heads submarine channel, located off the mouth of the Main Arm distributary channel. South of this, several smaller channels cross the slope. The Roberts Bank Channel is thought to have formed seaward of a

30

now abandoned distributary channel. For most of its course, this channel is characterized by a rounded cross section, indicating infill, but in the head region it has virtually no remnant relief and the seafloor has a low-relief hummocky morphology that is interpreted to be erosional in nature. Three small submarine channels are located off Canoe Passage. The two northernmost submarine channels are inactive and partially degraded by active current erosion and infill. The southernmost channel appears more recently active but is partly infilled in his middle part by a slide block.

Smaller scale morphologic features such as 2-D and 3-D subaqueous dunes, solitary dunes and outcropping beds characterize much of the delta slope. Outcropping beds are interpreted to be the product of local erosion by tidal currents and shoaling waves. The development of a concave profile in this zone is thought to be an indicator of marine transgression (Carle and Hill 2004 submitted).

2.3. Methods

A side-mounted, downward-looking, 615kHz RD Instruments Workhorse Monitor ADCP was used to make detailed measurements of the nearshore flow from the CCGC Revisor. The four transducer beams were set with an off-axis beam angle of 20° which allows measurements to be made to 94% of the bottom depth. The instrument measures the velocity components in terrestrial coordinate u_j v_j w_j directly from the Doppler frequency shift relative to pitch and roll. A bottom-tracking feature allowed the measurements to be automatically bed referenced and positioned by DGPS.

Data were collected daily over a 10-day period between June 29 and July 8 2001. The survey design is shown in Figure II-1. Three configurations were employed, two with the boat in motion, and one anchored station:

1. The survey area was divided into five contiguous boxes (B1-B5) along the delta front between 5 m and 60 m depth. The boat was steered around the periphery of each box, running continuously at 5-6 knots (2.5-3 m s^{-1}) for a 10–h period. This allowed two alongshore and two cross-shore profiles to be run in less than one hour and for a time series of profiles to be constructed. The instrument was programmed with different configurations (ping rate, number and size of bins) depending on the depth and accuracy required. The raw data were averaged at each depth over 15 measurements, so that the typical data cell size lies between 80 and 110 m in the horizontal. At each cell, the average velocity was compared to the error and accepted when the error was less than 30 % of the absolute value. This filter typically eliminated approximately 3 % of the data. To determine the depth-averaged velocity, the mean profiles were numerically integrated over the water column and divided by the number of good bin cells. The coordinate system was corrected for magnetic north, and rotated to obtain a shore-normal x axis with u defined as positive shoreward and a shore-parallel y axis with v defined as positive south-eastward along the shore.

2. A one-day survey of the entire Roberts Bank delta slope along the 10 and 20 m isobaths was also carried out. One line was run in 5 m of water. The same boat speed of 5-6 knots (2.5-3 m s^{-1}) was used, allowing a single line to be run in one hour. No tidal correction was applied. These data were processed in a similar way.

3. A 24-h fixed station was established in the middle of box B3 on July 5-6. The strong currents in the area caused the boat to drift on its anchor between 20 and 35 m water depth (including tide). Data from 0 to 25 m depth were averaged in 1 m bins every 10

minutes. In addition, a CTD and Niskin bottle cast was completed every hour. Water samples from Niskin bottles were filtered and weighed to measure suspended sediment concentrations.

Hourly wind speed and direction at Sand Heads were obtained from the Canadian Atmospheric Environment Service and tide elevation at Point Atkinson (Fig. II-1) from the Canadian Hydrographic Service.

2.3.1. The acoustic backscatter signal

In recent years acoustic systems have gained increasing acceptance by coastal and estuarine sedimentation researchers for the measurement of suspended sediment concentration and particle size profiles. Profiles of the backscatter intensity measured by the ADCP were analyzed to obtain a qualitative view of the suspended sediment concentration in the profiles. Backscatter signal and velocity measurements are coincident in space and time. To obtain quantitative profiles of concentration from a single transducer operating at a fixed frequency, knowledge of the sediment concentration and grain size distribution is required, because the scattering and absorption properties of the sediment are dependent upon grain size. In the field, the size distribution varies spatially and temporally so the calculation of the suspended concentration from backscattered acoustic intensity may involve considerable uncertainty. Alvarez and Jones (2002) used simple linear regression of the raw acoustic backscatter signal strength, converted to decibel (dB), to estimate the suspended sediment concentration. This method requires a large number of water samples to obtain an accurate estimation, and does not take into account the loss by sediment attenuation. They assumed that uncertainties in the acoustically estimated concentration were less than 50 % in the lower parts of the

concentration profiles. However, other scatterers (i.e. fish, zooplancton, internal waves, and turbulence) can also be present and may induce bias in the sediment concentration estimate. In our study area, organic matter can be as much as 18 % of the river's suspended load (Milliman 1980). Near the river mouth, organic matter with wood and plant fibre may be important constituents (1-3 %) of the bottom sediment coarse fraction (Mathews and Shepard 1962).

Without calibrated backscatter amplitude to allow the determination of the system constant, and because insufficient grain-size data were available to properly calibrate the backscatter *in situ*, an "absolute backscatter" method including only the water attenuation coefficient was used in this study to estimate suspended sediment concentrations. To account for the range-dependent signal loss in the water TL, we used the equation given by RD Instruments[TM] and also used by Flagg and Smith (1989):

$$TL = 20\log(r) + 2\alpha_w r - 10\log(D \cdot 10^{-3})$$

(1)

where r is the range in meters, α_w is the attenuation coefficient due to water in neper per meter, and D is the bin size in meters. The first term accounts for the radial spreading of the transmitted signal, the second term for the absorption of acoustic energy as it propagates through the water and the third term for the effect of the total volume of water ensonified at any one instant. The amount of sound energy lost or attenuation due to absorption depends on the frequency of the instrument, the salinity and the temperature. For instrument frequencies higher than 1MHz, the effect of salinity vanishes and several authors (Hay and Sheng 1992; Lee and Hanes 1995; Thosteson and Hanes 1998) recommend using Fisher and Simmons (1977). In our case with a 600KHz ADCP, we used the following expression described by

DLR Software Ltd SEDIVIEW (1997) derived from an equation established by Liebermann (1951).

$$\alpha_w = f/91500 \times \left[\left(\frac{1.86S \times ft \times f}{ft^2 + f^2} \right) + 2.86 \times \frac{f}{ft} \right]$$

(2)

where f is the frequency in MHz and ft is the relaxation frequency:

$$ft = 21.9 \times 10^{\left(6 - \frac{1520}{273 + T} \right)}$$

(3)

and T is the temperature in degrees Celsius at the given range.

The sediment attenuation α_s due to absorption and scattering by particles is negligible and then ignored. When sediment concentrations are high, this assumption is no longer valid.
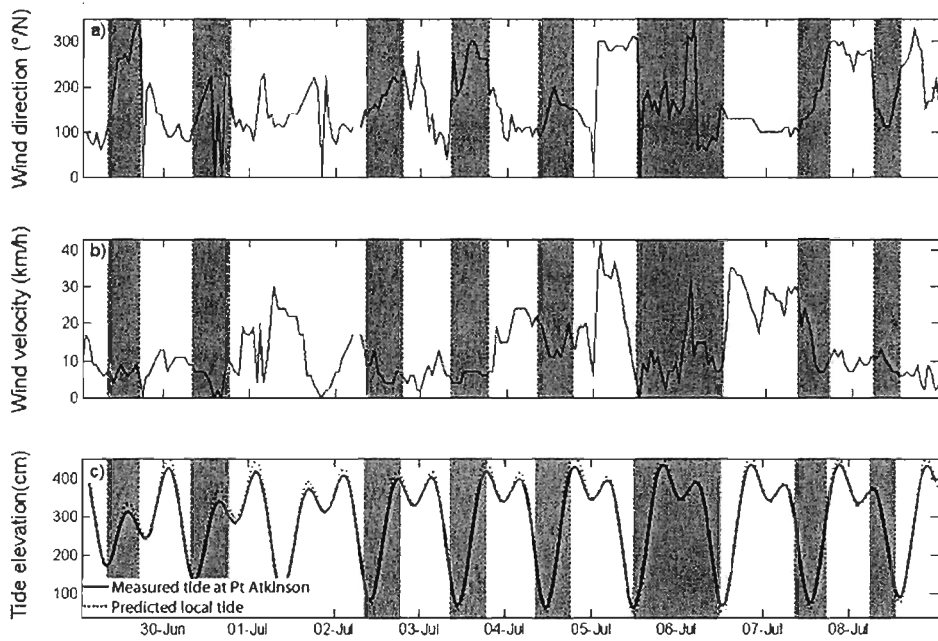
Figure II-2: (a) Time series of wind direction in degrees and (b) velocity in km h^{-1} during the field period. (c) Local predicted tide elevation in plain line and tide elevation measured at Point Atkinson measured in dotted line in cm.s^{-1}. The survey time is shaded in gray.

2.4. Current regime

Wind conditions over the measurement period were relatively light, rarely exceeding 40 km h^{-1} (Fig. II-2a-b), and we assumed wind driven currents to be negligible.

The Fraser Delta is a macrotidal environment. The waters enter by the south of the Strait of Georgia and are reflected at the end of the channel. This produces a standing wave in the Strait of Georgia which explains the northward monotonic increase in the tidal constituents (Thomson 1981). At Point Atkinson (26 km north of Roberts Bank) eight forcing constituents account for 86.1 % of the tidal height range in the diurnal (K1,O1,P1,Q1) and semidiurnal (M2,S2,N2,K2) frequency bands (Foreman *et al.* 1995). Semidiurnal fluctuations are slightly more important than diurnal fluctuation. As a result, the tide is a mixed semidiurnal tide. The local predicted tide and Atkinson tide gauge data during the field experiment are shown on Figure II-2c. The tidal phase generates a 9 min. lag between the site and Point Atkinson. The first 2 days of measurements were under a relatively small tide, whereas the others days were influenced by a significant spring tide, with maximum amplitude of 3.69 m on July 5 and 6.

The tidal currents are strongly bi-directional flowing along the isobaths, towards the West-North-West for the flood and the East-South-East to South-East for the ebb flow. A general observation is that the flood flow is stronger and of longer duration than the ebb flow (Fig. II-3) as observed in deeper water (Kostaschuk *et al.* 1995) and predicted by model simulations (Crean 1976, 1978; Foreman *et al.* 1995). Tidal currents are also stronger in shallow water during flood tide but stronger in deeper water during ebb tide. A plot of the standard deviation
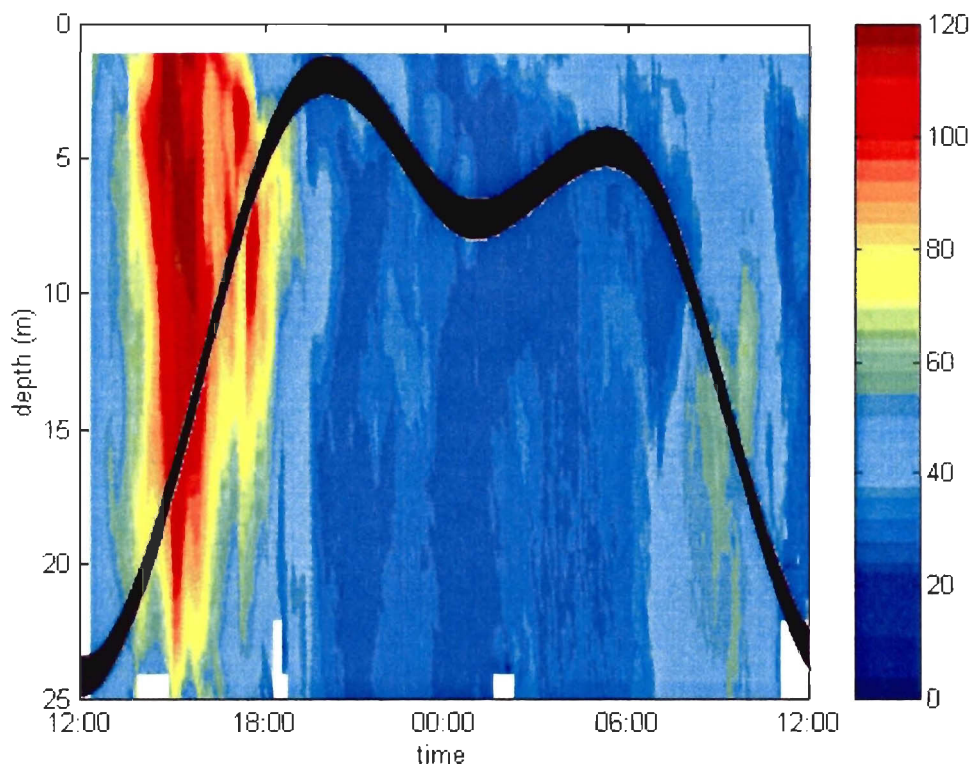
**Figure II-3**: Current magnitude in cm s^{-1} during the 24-hr station in 25 m depth. The dark thick line schematize the tidal elevation.
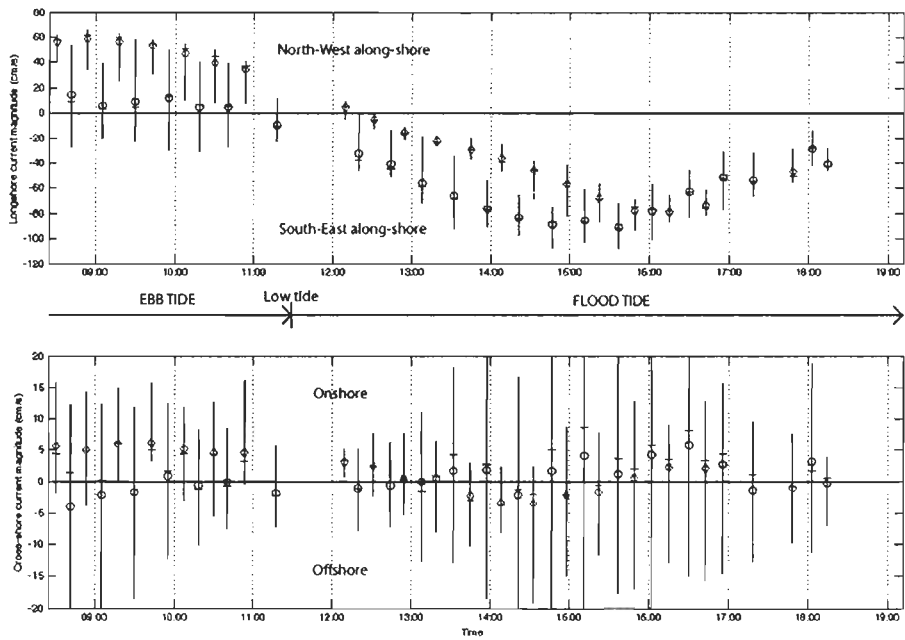
Figure II-4:   Time series of cross-shore and longshore components of the tidal current measured around the box B2 on July 4 in cm s^{-1}. Offshore mean velocities are presented in diamond. Coastal mean velocities are presented circle. The line mark represents the median.

of the depth integrated velocity components for July 4 shows that the longshore currents were more variable than the cross-shore currents (Fig. II-4). This variance is present mainly in the offshore (deeper water) transects. For the inshore transects, the cross-shore current variability was of the same order as the longshore current variability.

2.4.1. Flood tide

Flood tide was observed on seven different days and at 5 boxes, along the full transect and during the 24-h station. The depth-integrated velocity in deep water for the maximum flood current was typically greater than 1 m s^{-1} and a maximum of 1.30 m s^{-1} was observed on July 4. The tidal current speeds on the upper slope are therefore considerably higher than those described by Kostaschuk *et al.* (1995) in 90m depth of water. Instantaneous velocities[§] reached values greater than 3 m s^{-1}. These values include several components including mean tidal flow, wind-driven flow, orbital motions and turbulent eddies. The maximum flow was observed in the mid water column (June 29 and July 2, 3, 4 and 7) or in the near-surface (June 30 and July 5). On July 5 (Fig. II-3), the maximum (1.20 m s^{-1}) occurred in high mid-water (5-10 m in 25 m water depth), but the current was particularly strong over the entire column (>1 m s^{-1}).

As the flood phase progresses, the flood current is first observed close to the coast, then develops progressively offshore and from the south to north. The flood flow fills the coastal water column within one hour of low tide (Fig. II-5). For the example shown in Figure 5, the rate of tidal progression is estimated to be 0.60 m s^{-1}, which approximates the mean current.

[§] Instantaneous velocity is here considered as non depth-integrated. However a horizontal mean over 15 measurements was used.
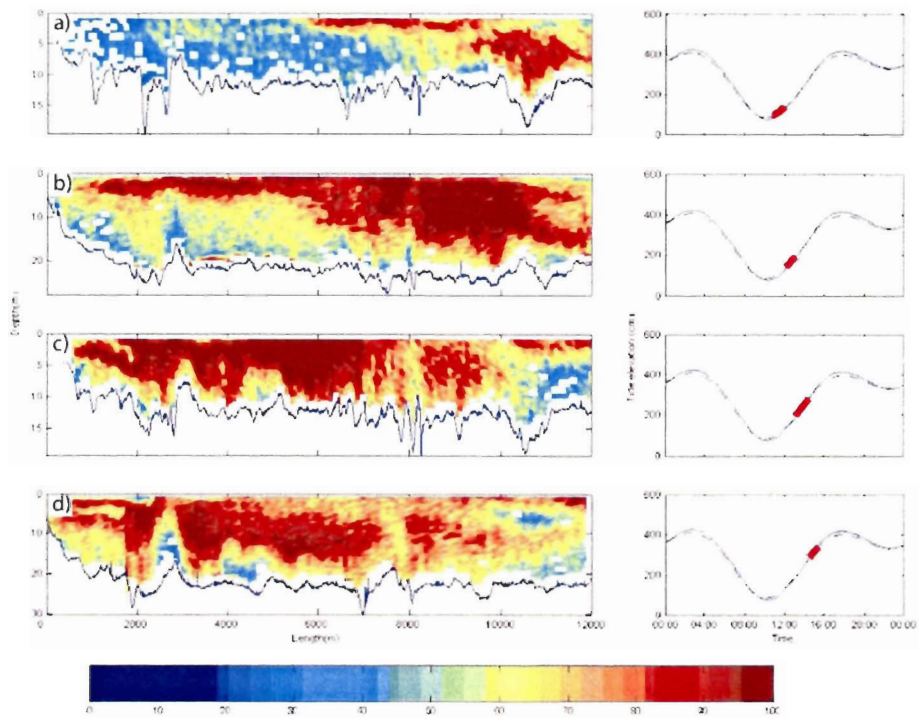
Figure II-5:   Selected transects along the coast depicting the current magnitude in cm s^{-1} during July 2. Northwest direction is on the left side of the graph. Tide elevation (in cm) is represented on the right side of the figure.

2.4.2. Ebb tide

Major ebb tide conditions were observed on only three days and at boxes B3 and B4 and during the 24-h station. The ebb tidal current is typically lower than the flood, with a depth averaged speed around 0.50 m s^{-1}, but it appears to have a more pronounced phase lag. For example, on July 8, the maximum velocity occurred 2 hrs 15 min before low tide and 4hrs 45 min after the high tide. Instantaneous current velocities reach 1 m s^{-1}. The maximum current speed was observed in deeper water, in mid-column between 25 m and 40 m. Despite a large variance in the cross-shore components due to a complex flow pattern induced by a rough bathymetry, an offshore current (0.2 m s^{-1}) is distinguished flowing in the surface layer. However this offshore flow does not expand far seaward.

2.4.3. Slack water

High tide conditions were observed on five different days (boxes B1, B2, B5, transect alongshore and 24-h station). Slack high water occurs almost simultaneously everywhere, with only minor phase lag with the high tide. Where measurements extended over the high tide, slack conditions occurred slightly later in deeper water than in the nearshore, although the lag was only in the order of 15 mins. Small remnant current velocities (0.15-0.30 m s^{-1}) were observed at high tide (see next section), but no direction was predominant.

Low tide conditions were observed on six days and at each box, during the full transect and the 24-h station. The slack low water field is also characterized by a remnant current and a difference in lag between the offshore and nearshore. On July 30, the current was minimal in

the nearshore at low tide, while in the offshore, the current reached a minimum about one hour later. On July 3, the currents were at a minimum before the low tide in the nearshore, while slack water in the offshore appeared one hour after low tide (except at the surface where the flood flow started to fill the area).

2.4.4. Remnant flow structures

Several ADCP profiles measured at low water slack tide showed complex structures in the water column as tidal currents reversed direction (Fig. II-6). On July 3 (box B3), three layers with opposite flow directions are visible, with the northwestward flood current appearing in the near surface and bottom layers while the intermediate layer is still flowing in the southeast, ebb-flow direction (Fig. II-6b). It should be expected that such remnant structures would rapidly dissipate within the flood flow. However on June 30 (box B1), a structure 1500 m wide in the alongslope direction and 20 m thick was observed 4 hours after slack tide (Fig. II-6a). The intermediate fluid shows a steep gradient in the flow direction, indicating strong shear between the remnant water mass and the surrounding strong flow. These structures may be related to inertial movements of a residual flow generated by flow separation over the complex topography of Sand Heads.
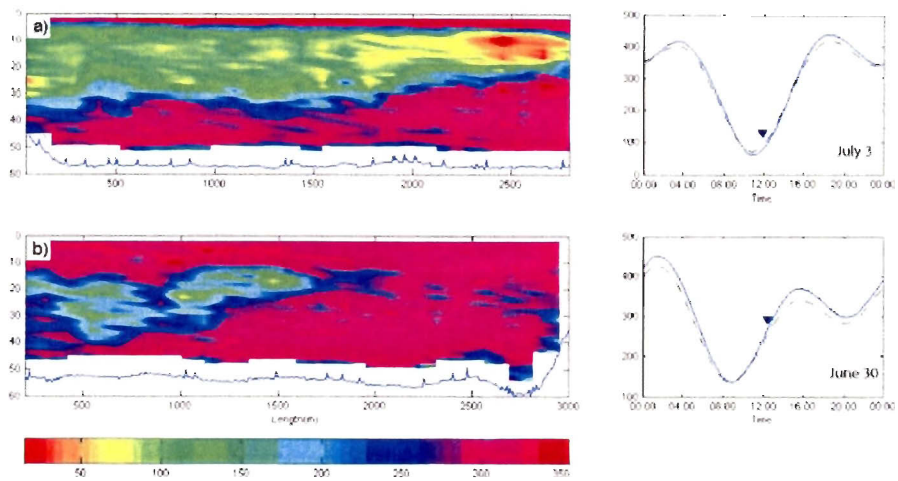
Figure II-6: Selected transects depicting the direction in degrees in earth coordinate system. (a) Current direction, box B1, June 30, measured 2 hrs after high tide (b) Current direction, box B3, July 3, measured 1hr after low tide.

2.5. Sediment transport processes, suspended sediment distribution

Water samples from Niskin bottles sampled on the 24-h station (5 July) showed an increase of SSC from near the surface (15 mg l^{-1}) to the bottom (35 mg l^{-1}). Microscopic analyses of the dried filters and Coulter Counter analysis showed that fine particles (mean 30 μm) dominated near the surface. Larger particles (>160 μm) were more abundant close to the bottom. The bed material on the upper delta slope is 125 μm (Barrie and Currie 2000).

2.5.1. Resuspension during flood tide

On every flood tide, an increase in backscatter intensity is observed in the lower water column near the peak of the flood current, indicating resuspension from the bottom (Fig. II-7). This is typically followed by a relatively rapid decrease, indicating rapid fall-out and sedimentation. Transect data show that backscatter is also highly variable along the delta front and generally higher in the nearshore than the offshore. Figure II-8 shows the lateral extent of near-bottom suspended sediment clouds for the full transect over the flood tide of July 2. In the early stage of the flood, two suspended sediment clouds and one particularly large one (extending through the entire water column) are visible in the nearshore transect. Each cloud is located in a specific area of irregular bottom morphology: A) large solitary dunes; B) a submarine channel off one branch of the Canoe Passage distributary channel; C) relict, erosional area to the northwest of a second branch of the Canoe Passage distributary channel; D) the head of the Roberts Bank Channel. As the flood progresses, each cloud expands and is advected
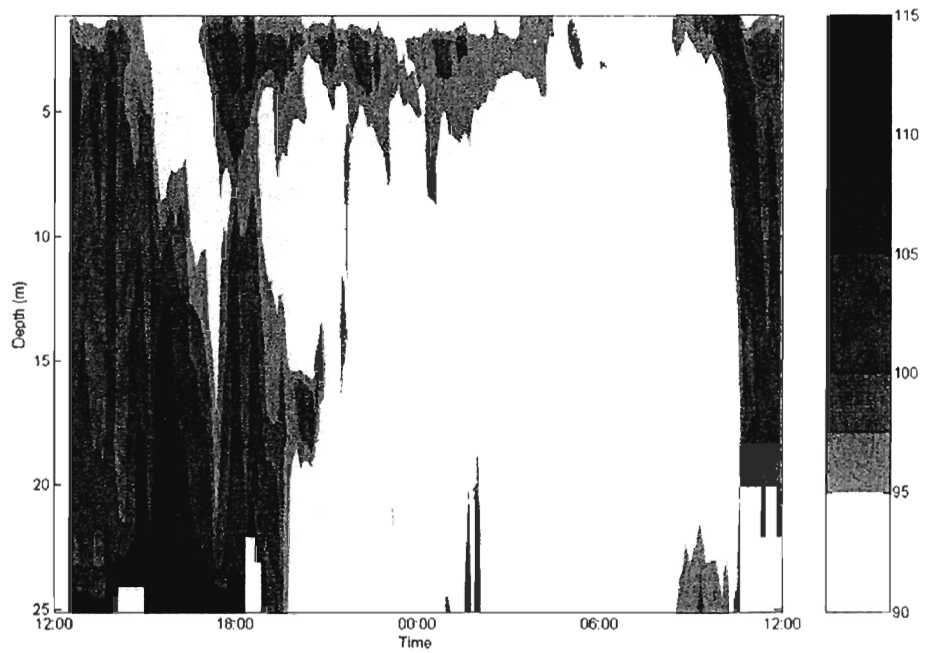
Figure II-7: Time series of backscatter intensity in dB during the 24h station, July 5. Resuspension from the bottom is observed during both flood and ebb tides.
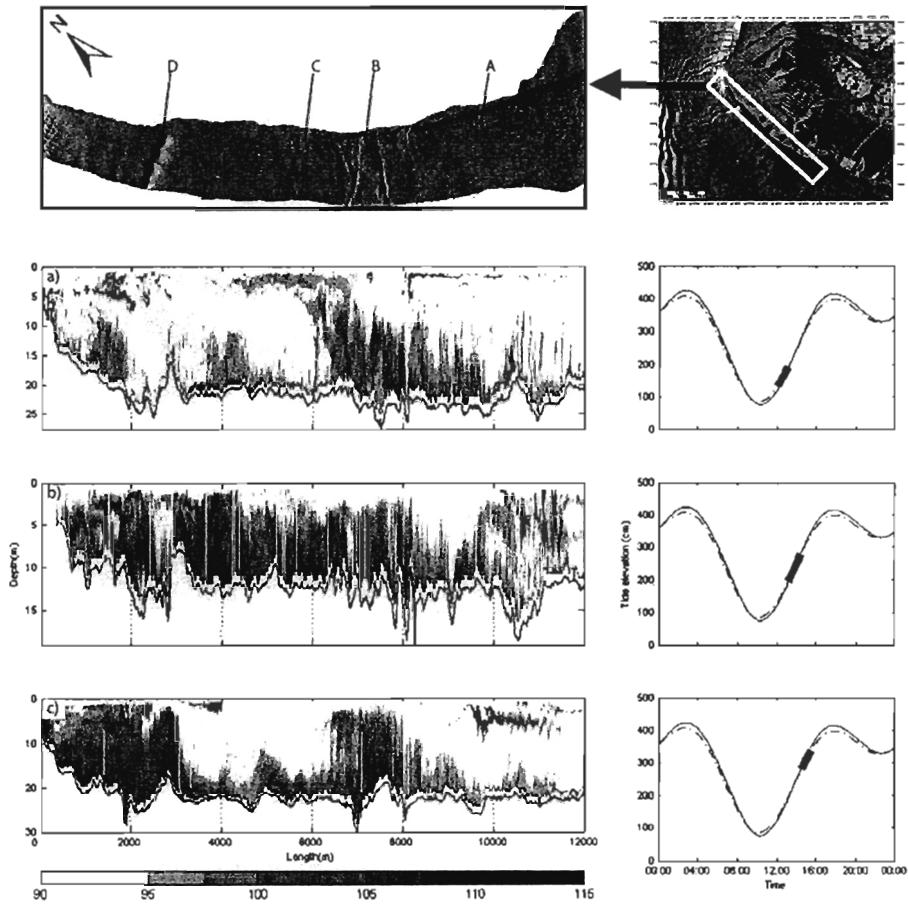
Figure II-8: Backscatter intensity in dB along the coast during July 2. The upper right graph shows transect position. The upper left graph depicts multibeam data associated with backscatter profiles a, b, c. Tide elevation (in cm) associated with each profiles is represented on the right side of the figure.

northwestward until the maximum flood current, when the suspended sediment cloud extends over almost all the nearshore and forms a broad cloud up to 3 km across (Fig. II-8b).

A more detailed example from box B2 (July 4) is shown in Figure II-9. Again, at the early stage of flood tide, two clouds originate from areas with rough seabed morphology. One cloud is located above an area hummocky morphology (A, Fig. II-9), while the other is located in an area of outcropping beds (B, Fig. II-9). Both morphologies are characterized by morphologies interpreted to be erosional in nature (Carle and Hill 2004 submitted). As the flood progresses, the clouds expand and are advected northwestward before starting to settle out at the waning stage of the flood tide.

2.5.2. Suspension during ebb tide

Bottom resuspension is less important during ebb tide conditions. On June 30, in box B1, just south of Sand Heads, a suspended sediment cloud was observed in deep water at low tide while the currents were almost negligible (Fig. II-10). Strong backscatter is observed in the entire water column and the cloud extends more than 500 m along the slope. Similar suspended sediment clouds were observed at slack ebb tide on July 3, 4 and 7. When the tide floods, these suspended sediment clouds tend to disappear rapidly and the phenomenon was not observed at high tide. The locations of these clouds seem to be closely correlated with distributary channels and the associated submarine channels. Figure II-11 shows the area of box B4 at late ebb tide on July 7, an area that includes three submarine channels off Canoe Passage. In the shallow water profile (Fig. II-11a), suspended sediment clouds are observed over the southern and northern channels. The offshore profile (Fig. II-11b) is characterized by
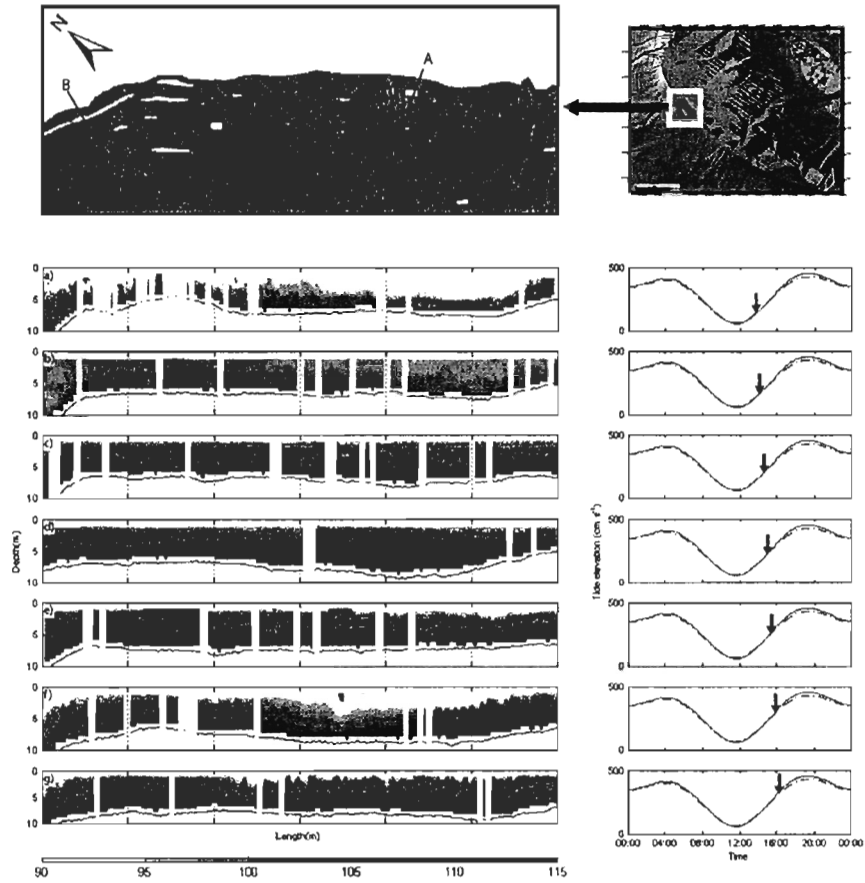
Figure II-9:   Backscatter intensity in dB in box B2 on July 4. The upper right graph shows transect position. The upper left graph depicts multibeam data associated with backscatter profiles a, b, c, d, e, f, g. Tide elevation (in cm) associated with each profiles is represented on the right side of the figure.
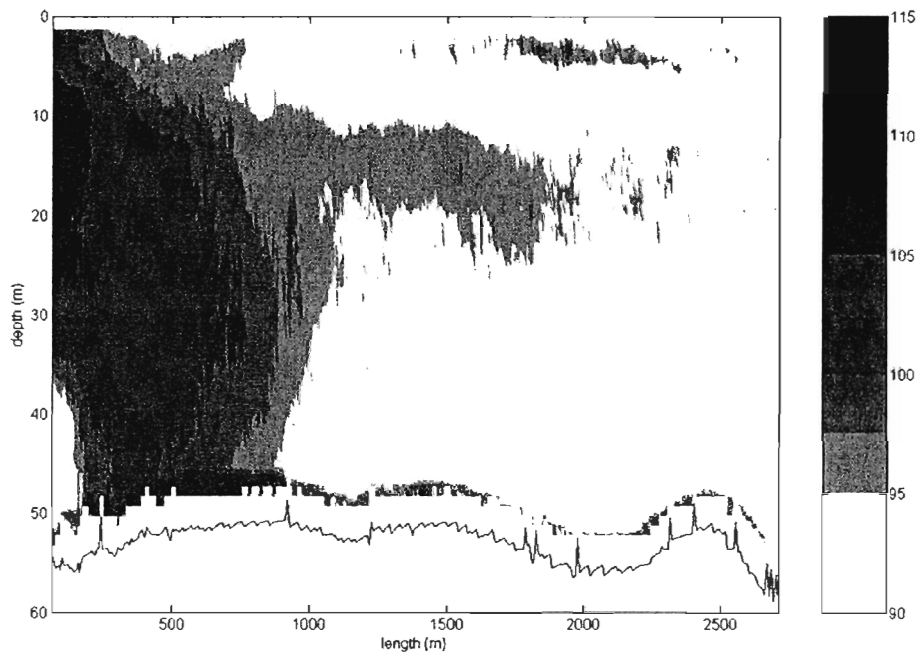
Figure II-10: Selected transect of backscatter intensity in dB. A maximum of sediment concentration is observed seaward of a major channel at ebb tide, box B1, June 30.

a cloud more than 1500 m wide that extends from the surface to the seabed indicating advection to the southeast in the direction of the ebb current and gradual settling to the seabed.

2.5.3. Cross-shore transport

Figure II-12 shows cross-shore transects of backscatter from box B2 on July 4 from late ebb tide stage (08.41 hrs) to high tide (16.30 hrs). This time series shows two apparent examples of cross-shore transport. During the late ebb tide stage (08.41 to 09.54 hrs), a near-surface suspended sediment plume extends offshore. This plume appears to be fed by ebbing flows from the tidal flats. One hour before low tide (10.18 hrs), the surface layer can be seen settling through the water column reaching the seabed in 40-50 m water depth within two hours. As the flood stage develops, bottom resuspension is clearly visible (14.46 to 15.37 hrs) and clouds of sediment appear to be advected into the mid-water column, suggesting offshore transport. At late flood tide stage, during the deceleration of the current (15.11 to 16.02 hrs), the bottom resuspension clouds seem to migrate seaward along the bottom and settle in deeper water.

2.5.4. Internal waves

Figure II-13 depicts a backscatter cross-shore transect on June 29, in box B5 at the early stage of flood tide. Strong backscatter intensity is visible in the upper 10 m of the water column. This surface plume is probably accompanied by a density difference between salt water and

fresh water discharged from the Fraser River or from tidal creeks. However, stratification tended to be weak throughout the field period because of vigorous tidal mixing.

The surface plume shows a distinctive internal wave structure with 2 m amplitude and 100 m wavelength (which shortens shoreward). Internal gravity waves in the Strait of Georgia have been observed in satellite images (Thomson 1975) and are thought to originate from strong ebb tidal current flow over shallow sills at the southern entrance to the Strait of Georgia. These flows generate internal hydraulic jumps and internal lee waves. On the ensuing flood, the internal waves are trapped at the upper layer interface and propagate in groups from south to north through the Strait of Georgia (Thomson 1975; Thomson personal communication). As they arrive at the delta front and the bottom shallows, the internal waves begin to steepen and shorten rapidly. Eventually, the waves become too steep and they break. This energy may add to turbulent mixing at the bottom on the upper delta slope.
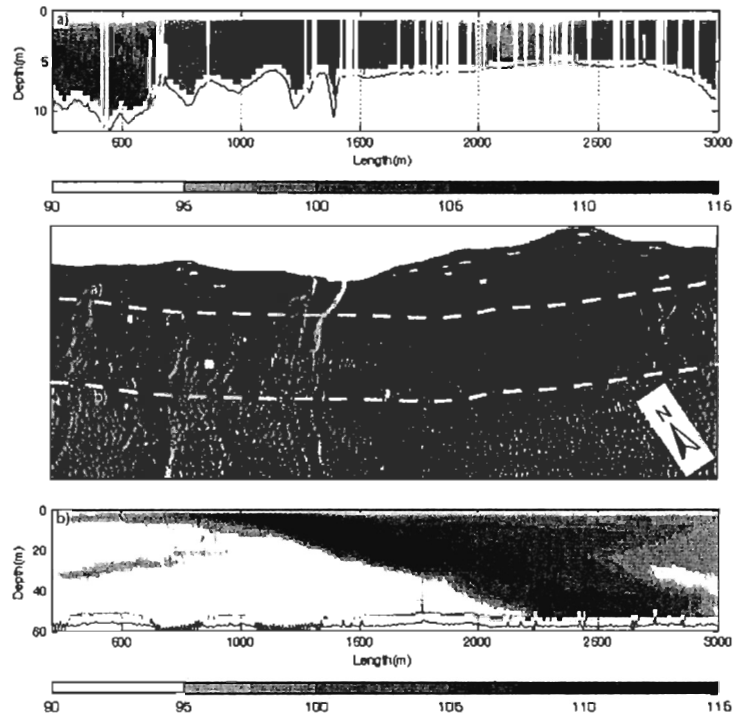
Figure II-11: Backscatter intensity in dB in box B4 on July 7. The mid graph depicts multibeam data associated with backscatter profiles a) and b). A maximum of sediment concentration is observed seaward of a major channel at ebb tide.
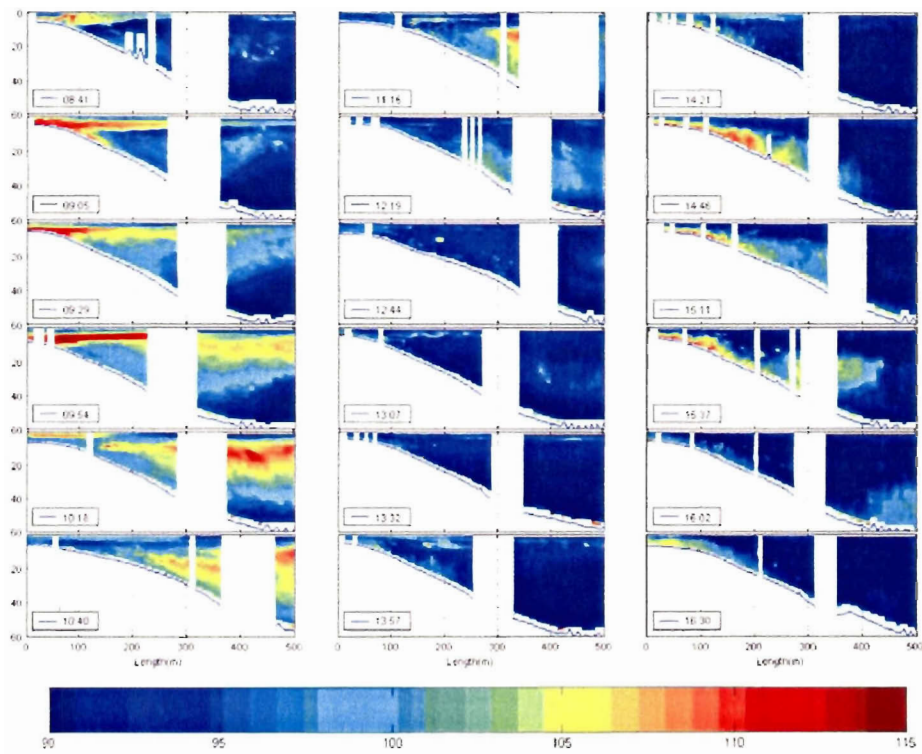
Figure II-12: Selected cross-shore profiles of backscatter intensity in dB in box B2, on July 4. Tide evolves from a late ebb tide stage (08:41) to a high tide stage (16:30). Offshore transport and resuspension events are observed in the Roberts channel.
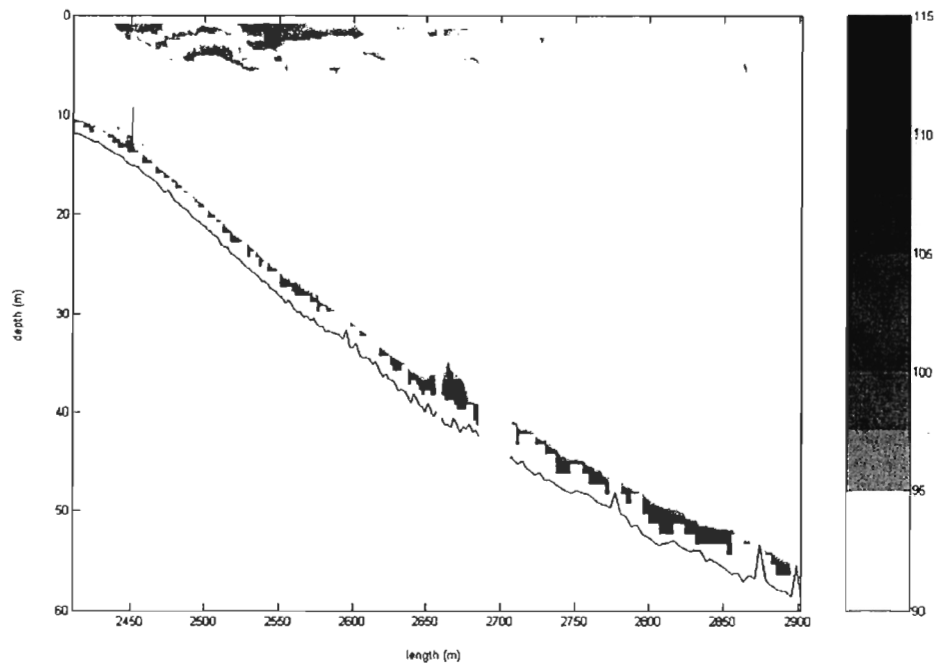
Figure II-13: Selected transect of backscatter intensity in dB in box B5, on June 29. The presence of internal waves can be observed.

a) Flood Tide

net offsho..
transport when
$(P_o + E) > C$

strong re-suspens...
off rough topography

b) Ebb Tide

surface plume
due to the river

surface plume from
tidal creeks and
distributary channels

weak bottom
resuspension

infilling former
distributary
channels

P_T = pressure force due to tide
P_o = pressure force due to setup
C = Coriolis force
E = excess weight force
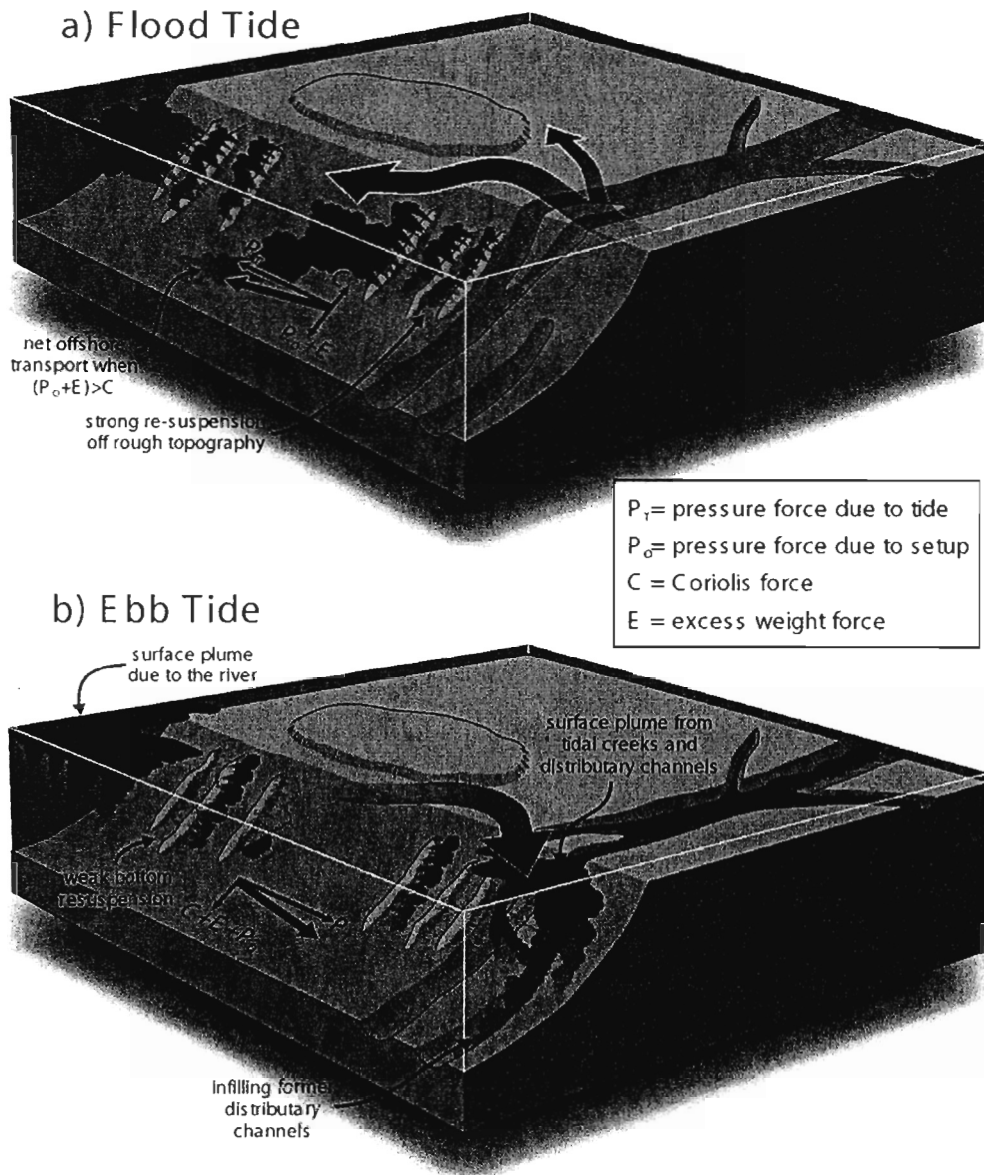
Figure II-14: schematic summary of the suspended sediment processes observed on the upper delta slope of the Fraser River during a) the flood tide and b) during the ebb tide.

2.6. Discussion

Figure II-14 provides a schematic summary of the suspended sediment processes observed on the upper delta slope of the Fraser River during the flood tide (Fig. 14a) and the ebb tide (Fig. 14b). The combination of different forces (tide, Coriolis, set-up and excess weight) may result into an alongshore transport of resuspended sediment and/or a cross-shore transport depending of the topography.

2.6.1. Flood resuspension

Numerous morphological indicators, including subaqueous dunes and outcropping beds attest to the regular and intense reworking of the slope by tidal currents and waves (Carle and Hill 2004 submitted). The data presented here demonstrate that the currents are sufficient to initiate sediment movement and resuspend sediment from the bottom (Fig. II-14a). The critical current speed for bed erosion of 0.125 mm sand, using the Yalin curve (Yalin 1972) modified by Li and Amos (1995), is 0.59 m s^{-1}. This is very close to the value at which the ADCP backscatter increases above background levels. This threshold is only reached near peak flood in water depths less than 25 m and sediments are fully entrained in suspension (Fig. II-7). In deeper water, direct resuspension by the tidal current was not observed. As the flood current wanes, sediment falls rapidly out of suspension. At slack tide, the water column becomes completely clear of suspended sediment. This is reasonable, given that the corrected Stokes settling velocity in still water (Baba and Komar 1981) for 0.125 mm sand is 1.75 cm s^{-1}, just over 1 m per minute.

The relatively large changes in the patterns of the suspended sediment clouds between consecutive profiles during flood conditions indicate that turbulent advection is important, especially in shallow water. The velocity profiles of Figure II-5 exhibit a large number of small-scale structures suggestive of turbulence. Suspended sediment profiles (e.g. Fig. II-8) show similar variability. The high level of turbulence may explain the poorer coherence of the ADCP data in the nearshore and the need to filter a large number of cells when processing the data.

The turbulence in the flood flow is generated by the rough seabed provided by the channels, subaqueous dunes and outcropping beds that characterize the seafloor of the upper delta slope. Similarly, sediment resuspension occurs over the same roughness elements (Fig. II-8). Studies of suspended sediment concentrations over subaqeous dunes have shown that suspended sediment clouds may be formed by turbulent ejection events originating on the stoss and crest of a dune (Sumer and Deigaard 1981; Kostaschuk and Church 1993; Garcia and Admiraal 1998; Lecouturier *et al.* 2000). Figures II-8b and II-8c show this well, with clouds of suspended sediment extending from the crests of dunes, particularly those associated with the heads of submarine channels off Canoe Passage. Carle and Hill (2004 submitted) noted that the head regions of these channels appeared to have been rapidly reworked, with the eroded material forming long wavelength "isolated" dunes. Our data show unequivocally that the reworking is very active, occurring during most flood tides.

The possible cross-shore transport identified on Figure II-12 should be considered with caution. While the time series is located over the Roberts Bank Channel and seems to indicate that a cloud of suspended sediment was generated by resuspension in shallow water and

moved down-slope, it should be noted that the predominant component of the current velocity at these times was the along-slope, not the cross-slope, component. This means that the cloud of sediment observed in the later sections was probably advected from several hundreds of metres along-slope. It is therefore unlikely that the cross-shore transport was effected by a turbidity current. Nevertheless, the presence of a suspended sediment cloud at depths greater than 50 m (well below the depth of resuspension) does indicate a significant cross-shore component of sediment transport. Despite the large variance in the current data, a weak offshore component of flow can be discerned for part of the flood tide (Fig. II-4). This could result from one or a combination of a downwelling component and a small gravitational component resulting from the concentration of sediment in suspension (Fig. II-14a; Myrow and Southard 1996). These would have to be strong enough to overcome the Coriolis force that would act in an up-slope direction on the flood current.

2.6.2. Ebb transport events

Net cross-shore sediment transport also occurs during the ebb tide (Fig. II-14b). The surface plume that develops on the ebb tide in Figure II-12 probably originates from both shallow water resuspension by the ebb tidal current and from ebb flow in the large tidal creek that crosses the tidal flats just to the north of box B2. The ebb tidal current appears to be just strong enough to resuspend finer sediment present in shallow water. Although averaging 0.5 m s^{-1}, instantaneous values considerably exceed this value. Anecdotal observations by the authors suggest that tidal flows in creeks draining the tidal flats carry fine sand and finer sediment in suspension to the delta front. The sharp gradient in backscatter in the top few metres of the water column (Fig. II-12, 09.05 hrs) suggests a degree of density stratification of the water column despite the moderate turbulence of the ebb tidal flow. However, the

sediment in suspension can be seen to settle rapidly at the end of the ebb tide and during slack tide (Fig. II-12, 09.54 – 12.19 hrs). Maxworthy (1999) and McCool and Parsons (2004) have suggested that the interaction between the sediment load and turbulent forcing can increase the effective settling speed of particles. Where the load consists of a significant concentration of fine sand, turbulent mixing between a buoyant gravity current and the ambient denser fluid produces gravitational instability and sediment is convected downward. The resulting convective plumes quickly remove sediment from the surface layer and deposit the sediment on the bottom in a process termed mixing-induced convective sedimentation. McCool and Parsons (2004) recently observed this process for suspended sediment concentration far lower than 1000 mg l^{-1}. The inferred concentrations of suspended sediment in the plume observed here are in the range of 15 to 60 mg l^{-1}.

Carle and Hill (2004 submitted) showed that although there is evidence for past gravity-flow activity in the Roberts Bank channel, it is no longer active and morphological and seismic evidence suggest that it is in the process of being infilled by relatively fine sediment. Our data shows that the process of infilling is likely to be this mixing-induced convective sedimentation.

2.7. Conclusion

1. Tidal currents on the upper slope of the Fraser River delta are strongly bi-directional, flowing along the isobaths. The maximum flood flow is stronger and of longer duration than the ebb flow. The slack water at both high and low tide exhibits remnant flow structures possible resulting from large-scale flow separation in the vicinity of the Fraser River mouth.

2. Around peak flood tide, the tidal current is strong enough to initiate sediment movement and create clouds of resuspended sediment from the bottom. In shallow water, the onshore component of the tidal current induces a net transport onshore while in deeper water, a weak component of offshore flow favours downs-slope transport. Channels, subaqueous dunes and outcropping beds provide significant bed roughness for the generation of turbulence and suspended sediment clouds.

3. Offshore sediment transport occurs over the ebbing tide in a surface plume originating from shallow water resuspension and tidal creek outflow. Sedimentation by mixing-induced convective sedimentation is favoured by the strong turbulence.

3. WAVE DYNAMICS OVER ROBERTS BANK: PROCESSES AND MODELLING

SAMUEL MEULÉ [A,B], PHILIP R. HILL [A], CHRISTEL PINAZO [B]

[A] NATURAL RESOURCES CANADA, GEOLOGICAL SURVEY OF CANADA - PACIFIC, 9860 WEST SAANICH ROAD, P.O. BOX 6000, SIDNEY, B.C., V8L 4B2, CANADA. EMAIL: sam.meule@nrcan.gc.ca

[B] LABORATOIRE D'OCEANOGRAPHIE ET DE BIOGEOCHIMIE, UMR 6535 CNRS/UNIVERSITE DE LA MEDITERRANEE, OSU/CENTRE D'OCEANOLOGIE DE MARSEILLE, STATION MARINE D'ENDOUME, CHEMIN DE LA BATTERIE DES LIONS 13007 MARSEILLE, FRANCE. EMAIL: samuel.meule@com.univ-mrs.fr

Abstract

Between 1 March and 26 March 2002, an instrumented wave and current measurement station was deployed on the upper delta slope of Roberts Bank in approximately 12 m of water. The measured wave characteristics for fair-weather, moderate and storm conditions were used as input parameters for a parabolic wave model. The model shows that storm waves act non-uniformly along the beach depending on the local morphology and tidal elevation. Waves propagating during high tide are characterized by smooth dissipation and progressive refraction while waves propagating during low tide show intense refraction and breaking in front or over a low tide bar. Sediment transport divergence in the nearshore will be strongly controlled by the temporal relationship between storm waves and tidal height.

Keywords: wave measurements, spectral analysis, parabolic wave model, sediment transport divergence
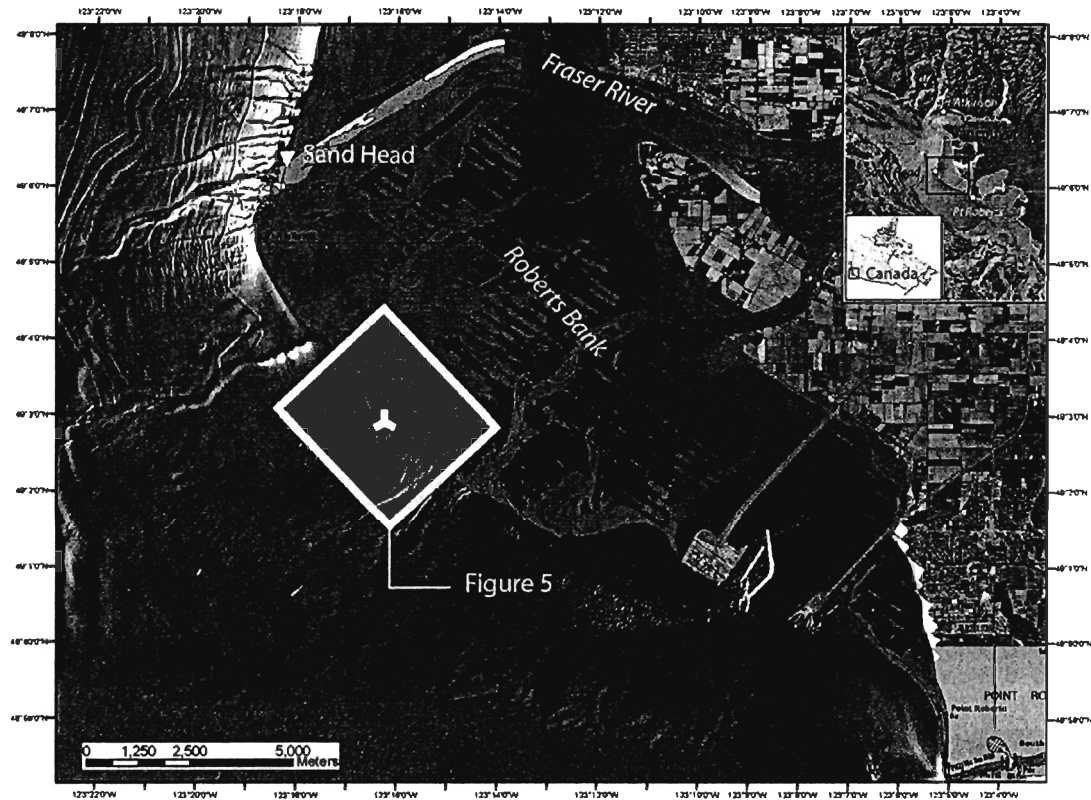
Figure III-1: Location map showing the study area with instrument deployment site and modelling grid, Roberts Bank, Fraser Delta, BC.

3.1. Introduction

The Fraser River delta is located on the southwest coast of British Columbia. Roberts Bank covers the intertidal delta between the Main Arm channel and Point Roberts headland (Fig. III-1). It is important, for planning civil engineering projects and evaluating the ecological sensitivity of deltaic environments, to be able to distinguish areas of active sediment deposition from those characterized by non-deposition and/or erosion. Based on a review of the literature, Hill (2001) developed a conceptual model for sediment transport on the delta front, suggesting that erosion in the nearshore of Roberts Bank is related to sediment transport divergence between the outer tidal flats and the delta slope during storms. An objective of the Geoscience for Ocean Management of the Georgia Basin project is to develop tools for evaluating sediment transport issues in the region. This paper reports on field measurements and initial parametric wave propagation model results aimed at understanding the impacts of storm events on nearshore sediment transport.

3.1.1. Physical Setting

There are two main morphologic zones of the subaqueous delta (Hart *et al.* 1995): (1) the delta front, at the seaward limit of the tidal flat that extends to approximately 10 m depth; (2) the delta slope, between 10 m and 100 m water depth with a typical slope of 2-3° but locally reaching 23°, the portion of the delta below the delta front that grades offshore into the prodelta zone (typically <1°). The detailed study area (Fig. III-1) was chosen for its linear low tide shoreline that was interpreted to be highly wave influenced. The local seabed in water depths less than 20 m is characterised by an area of outcropping beds and large solitary dunes

indicating erosional and/or sediment–starved conditions. A LIDAR image, collected on Roberts Bank in 2001, shows an archipelago of small low tide bars on the outer part of Roberts Bank.

In a review of 1967 to 1990 wind data, Hill and Davidson (2002) determined that the most frequent winds are from east, southeast and northwest, with the strongest winds blowing from northwest and southeast. The longest fetch is 80 km to the northwest, whereas the fetch from southeast is 45 km. Significant wave heights greater than 1 m are mainly generated by southeast and northwest winds with a small contribution from the south and west. Waves with period higher than 6.0 s come only from the northwest.

3.2. Methods

3.2.1. Field measurements and processes

A Norton instrumented tripod (Birch *et al.* 2003) was deployed at Roberts Bank in approximately 12m water depth from 1 to 26 March 2002. Velocity and pressure measurements were recorded with a Marsh McBirney current meter and a Nortek Aquadopp Profiler equipped with a pressure gauge. Spectral analysis was used to assess wave characteristics, assuming the sea state to be represented by a superimposition of Airy waves (linear approximation). Spectral analysis was conducted on the pressure data using an ensemble and band-averaging power auto spectrum With 512-s Hanning windows and 75 % overlap. Pressure measurements were converted to water elevations (Horikawa 1988) which leads to a necessary cut off imposed at 0.25Hz. A linear de-trending method increased the reliability of the results. Higher cut-off frequencies were also used to evaluate the importance

of frequency range. Wave directions were computed using cross spectral analysis between pressure and velocity time series

Waves in shallow water produce an oscillatory motion. The horizontal orbital velocity is given by the Stokes equation:

$$u = \zeta_0 \cdot \frac{2\pi}{T} \cdot \frac{ch[k(z+h)]}{sh[kh]} \cdot \cos(kx - \omega t) + 3 \frac{\pi^2}{\lambda.T} \zeta_0^{\,2} \frac{ch[2k(z+h)]}{sh^4[kh]} \cdot \cos 2(kx - \omega t) \qquad (1)$$

The second term of equation 1 is a non-linear term. It represents the wave deformation. When considered negligible (<50 % of the first term), the wave orbital motions ($\overline{u_w} = 0$) were obtained by filtering out the low-frequency velocity fluctuations assumed to be due to the tidal current $\overline{u_c}$. When this second term is not negligible, the nearshore wave deformation induces a current. Because this wave-induced current no longer corroborates the hypothesis $\overline{u_w} = 0$ the direction was not calculated. The frequency spread direction was also estimated.

For each burst, the mean water level obtained from the pressure gauge was compared with measurements from the Canadian Hydrographic Service tide gauge located at Point Atkinson, 26 km to the north. Hourly wind speed and direction were obtained from the Canadian Atmospheric Environment Service, from a station at Sand Heads (Fig. III-1).

3.2.2. Wave propagation model

The bathymetry of the subtidal portion of the study area was extracted from the GSC multibeam database and rotated to orient the coastline to the top of the grid. The tidal flat bathymetry was extrapolated using Delaunay linear triangulation.

The propagation of a monochromatic wave is commonly modelled using the Mild Slope Equation:

$$\nabla(CCg\nabla(\phi)) + k^2 CCg\phi = 0 \tag{2}$$

where C is the phase velocity ($=\omega/k$), ω is the wave angular frequency, k is the wave number, ϕ is the horizontal velocity potential and Cg is group velocity. The elliptic equation of Berkhoff (1972, 1976) was not used in its original form. For computational efficiency, the main direction of wave propagation was projected onto the X-axis and equation (2) was solved in a parabolic form (Radder 1979):

$$\frac{\partial\phi}{\partial x} = \left(ik - \frac{1}{2kCCg}\frac{\partial kCCg}{\partial x}\right)\phi + \frac{i}{2kCCg}\frac{\partial}{\partial y}\left(CCg\frac{\partial\phi}{\partial y}\right) \tag{3}$$

where i is the imaginary number, C is the phase velocity ($= \omega/k$), k is the wave number, ϕ is the horizontal velocity potential, Cg is the group velocity.

Wave information is prescribed only along the upwave boundary of the model. At the other boundaries it is assumed that no waves enter the model. This leads to unrepresentative results

69

near the lateral boundaries. These boundaries must therefore be chosen far enough from the area of interest.

The Radder parabolic equation remains valid for propagation angles within 30° of the initial direction of propagation. Kirby (1986) modified the parabolic equation form to extend the validity to within 50° while Mordane *et al.* (2004) extended it recently to 90°. From the Kirby (1986) and Mordane *et al.* (2004) criterion, equation 2 is valid within 50° for a 10 % error. However this directional restriction implies some limitations on the use of the model.

In the absence of infragravity energy, the breaking criterion used is based on Battjes (1974), which defines δ=0.8 for spilling and plunging waves.

When waves break, the surface elevation in the surf zone is recalculated from the equation of Stive (1984):

$$\frac{\partial \eta}{\partial x} + \frac{\eta}{4h}\frac{\partial h}{\partial x} = A_{\epsilon}\left(\frac{h}{gT^2}\right)^{\frac{1}{2}}\left(\frac{\eta}{h}\right)^2 \tag{4}$$

where η is the surface elevation, h is the depth, A_{ϵ} is a dimensionless dissipation factor, H is the wave height, g is the acceleration due to gravity, and T the wave period.

The wave propagation is calculated using an implicit Crank-Nicholson numerical scheme.

3.3. Results

3.3.1. Field measurements

The general oceanographic conditions over the study period are shown in Figure III-2. The month of measurements included five extended periods of fair-weather conditions and four periods of more energetic conditions including two major storms. The mean water depth shows the mixed semidiurnal tidal oscillation (Fig. III-2f). The mean water level was not raised significantly in response to winds and no coastal set up occurred. The spectral energy density plot (Fig. III-3) indicates generally low energy waves mostly confined to the high frequency range, with most of the recorded periods being under 8 s. Long period waves (>7 s) were associated with small significant wave height generally less than 0.3 m.

Fair-Weather Conditions (Days 1–5, 6–9, 12-15, 17-18, 19-27)

Five periods of fair-weather presented similar conditions. Light winds (<10 km h^{-1}) occurred for most of the time and they blew from northeast, southeast and south-southwest. Moderate winds (<20 km h^{-1}) blew randomly from the northeast, east-southeast, west-southwest and north-northwest. Wind direction tended to change abruptly and last only few hours at a time. These conditions generated waves with significant heights less than 0.25 m coming predominantly from the south, southwest and northwest. Under these conditions, wave periods were relatively variable, and long wave periods recorded e.g. 10 s peak period recorded on March 2 and March 20.

71
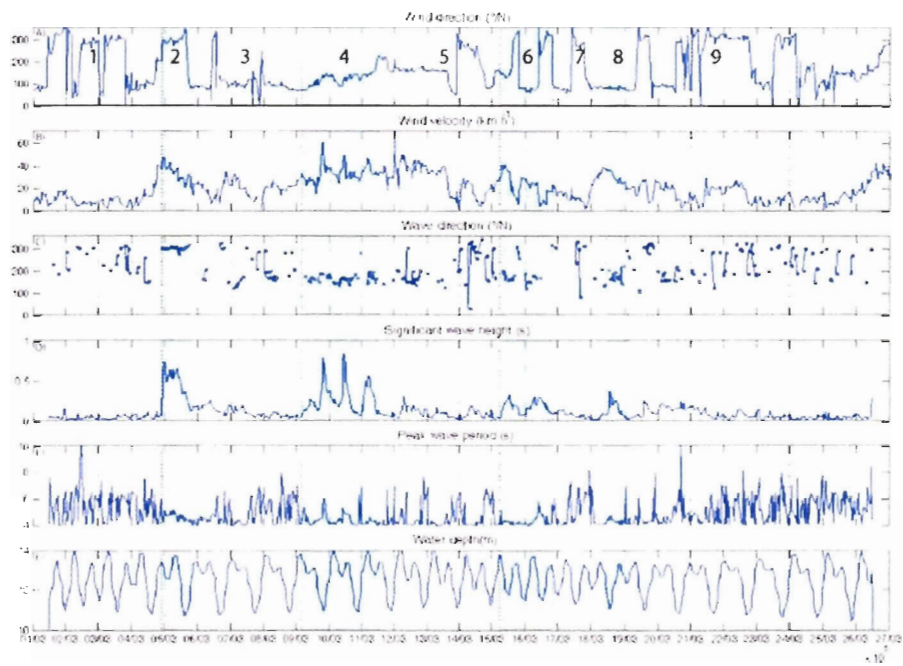
Figure III-2: Times series of: **A)** wind direction (°/N); **B)** wind speed (km h⁻¹); **C)** wave direction (°/N); **D)** significant wave height (m); **E)** peak wave period (s); and **F)** mean water depth (m). The measurements period is divided into different intervals representing fair-weather (1, 3, 5, 7, 9), moderate storm (6, 8), and major storm conditions (2, 4).
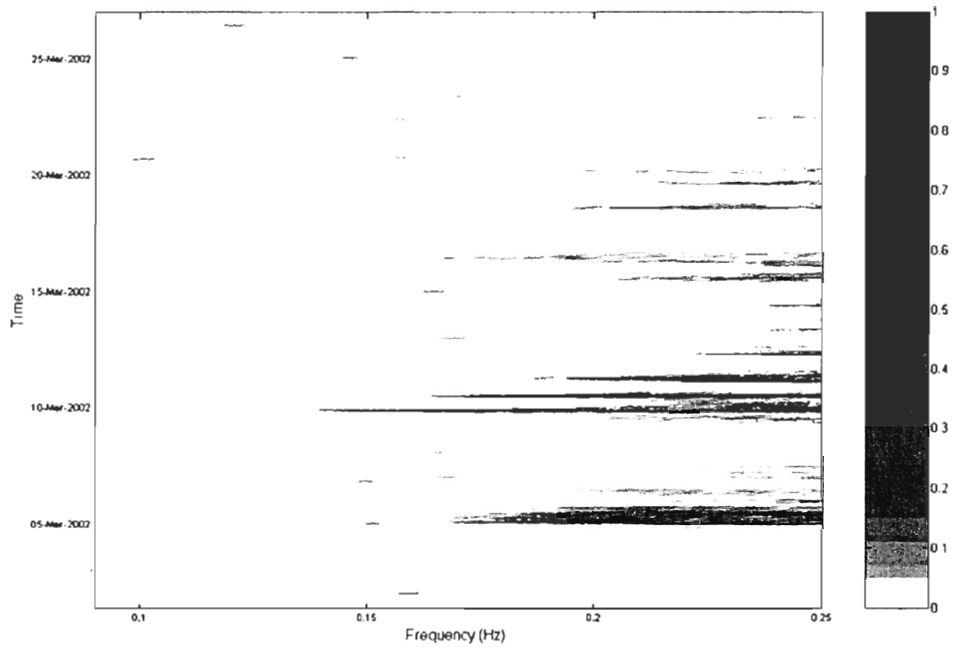
Figure III-3: Observed sea-surface spectral density in m² Hz⁻¹ for the overall period. Colorbar is in greyscale.
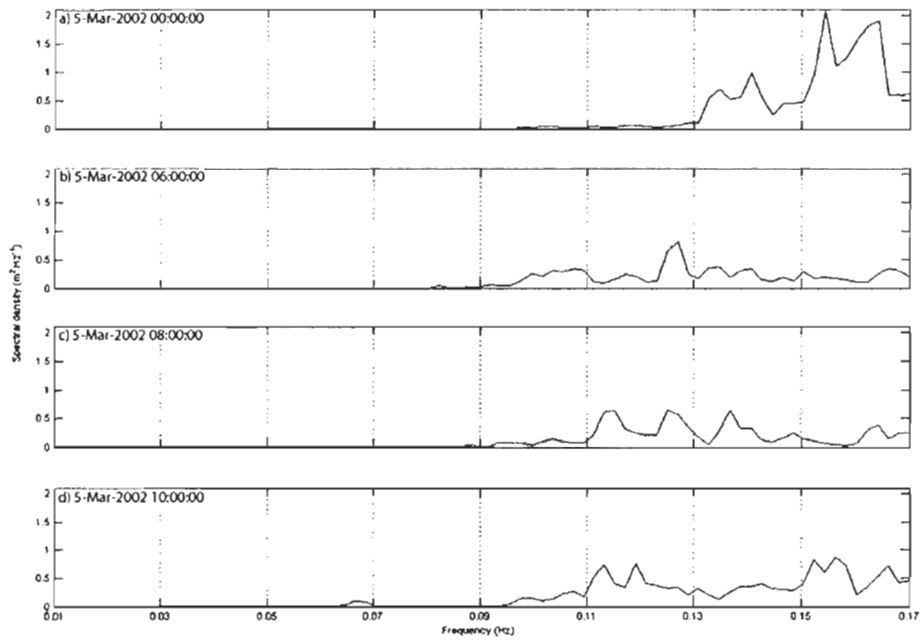
Figure III-4: Observed sea-surface spectral density in m² Hz⁻¹ for 4 selected burst during the major storm of 5 March 2002.

Moderate Storm Conditions (Days 15-17, 18–19)

Two moderate storm conditions were observed. Wind speeds built through the end of March 14 and the morning of March 15 and reached 40 km h^{-1}. Wind direction switched from the southeast at the peak of the storm to the northwest during the waning storm. Relative small waves with short periods were observed propagating from the south. The significant wave height increased to 0.4 m during a low tide condition. The energy was confined to the high frequency range and showed several narrow peaks (below 0.4 m^2 Hz^{-1}). Wave height decreased during the afternoon of March 15, propagating from the west. After an abrupt easterly rotation of moderate wind speed (30 km h^{-1}), the winds switched to the northwest. These conditions during the ebb tide generated moderate waves (Hs: 0.3 to 0.32 m) associated with both wind directions. They propagated from the south and the south-southeast and were relatively long-period waves (increasing from 4 s to 6 s and then decreasing). During the second moderate storm, between midday on March 18 to the early morning of March 19, winds blew from the east. Wind speed decreased from 40 km h^{-1} to 20 km h^{-1}, generating short period waves (between 4.1 s to 4.8 s) from the south, with a maximum significant height of 0.38 m at low tide. Towards the end of the waning phase, wave periods became very variable and very small waves with long periods were recorded. The spectral density distribution was similar to the first moderate storm.

Major Storm Conditions (Days 5 and 9-12)

Day 5 was characterized by a significant storm. As the winds rose through March 4, they turned from the east to the northwest in a clockwise rotation. Winds up to 48 km h^{-1} were recorded at the peak of the storm when the water elevation was at the secondary low tide.

Significant wave heights exceeded 0.5 m for 12 consecutive hours and reached 0.74 m, propagating from the northwest. Figure III-4 displays the spectral density for 4 bursts over the storm showing the evolution of energy distribution from high frequency range toward lower frequency. This progression was combined with a progressive loss of energy from 2.1 $m^2 Hz^{-1}$ when the storm increased suddenly to 0.9 $m^2 Hz^{-1}$ at the end of the 12th hour. The peak wave periods ranged between 5.5 and 4.5 s. As the storm waned, winds rotated back in a counterclockwise sense to the E. Wave height and period decreased rapidly.

A second intense storm lasted 3 days between March 9 in the morning and March 11, lasting over two full tidal cycles. Winds switched progressively from the southeast to the southwest over the period of the storm, increasing in speed between 20 and 60 km h^{-1}. Three major wind speed peaks over 50 km h^{-1} were observed and corresponded with 3 peaks of significant wave height (0.77, 0.83, and 0.55 m). The energy distribution was broad and harmonics were present in the relatively low frequency range. The first two peak events generated relatively long period waves (6 and 5.4 s) while the last peak event of this storm was associated with short period wave (4.6 s). Waves came predominantly from the south and south-southeast. Waves for the first peak propagated during low tide while the two later peaks were at high tide.

3.3.2. Model results

Figure III-5 presents the bathymetric grid used for wave simulation. The colorscale highlights the main features in shallow water. The upper shoreface slope breaks between 6 m and 7 m water depth. Above this depth, the morphology is characterized by the presence of a low tide bar and trough system almost parallel to the shoreline in about 2 m of water (A, Fig. III-5). At

Condition	Time	Figure	Wave height	Peak Wave period	Wave incidence	Tidal elevation
Fairweather	03 March 11:00	N	0.03	7.31	243	1.25
First moderate storm	15 March 13:00	III-6a	0.33	4.26	196.7	1.30
Second moderate storm	16 March 12:00	III-6b	0.30	5.12	260.8	1.18
Second major storm	10 March 12:00	III-7	0.835	5.06	181.29	2.4624
Second major storm	9 March 20:00	III-8	0.78	5.39	214.73	0.53
Second major storm	9 March 20:00	III-9	0.78	5.39	214.73	0.53

Table III-1: Wave parameters for simulation. Conditions were chosen to represent fair-weather and both moderate and major storm conditions.

the northern side of the domain, the height of the bar is about 1.3 m and the width is about 250 m. The low tide bar progressively disappears southward. A broad trough separates the low tide bar from the tidal flat. A second parallel bar, with a crest depth of 3 m, is located in the central part of the grid (B, Fig. III-5). The height of the bar is less than 1 m and the width is about 100 m. This low-amplitude ridge is almost 300 m long and is slightly oblique to the shoreline. Wave parameters from the field measurements were used as input parameters for 2D simulation. The wave conditions outlined in Table III-1 were chosen to represent fair-weather, moderate and storm conditions. The tide elevation measured from the Marsh McBirney pressure gauge was considered in each simulation.

Fair-weather conditions

Wave height were almost insignificant during fair-weather. Very small waves from all directions propagate across the upper shoreface without any modification. The effect of wave breaking is negligible but the low tide bar induced a few centimeters of shoaling in very shallow water. Waves converge over the front of the bar and diverge on the lee side.

Moderate Storm condition

Figure III-6 shows the pattern of the significant wave height as computed by PARAB for the first moderate storm condition. The second moderate storm showed similar characteristics but is not presented here. The two simulations show similar characteristics despite the two different wave incident angles (Table III-1). On the tidal flat, a noisy amplitude modulation spreads across the model grid suggesting that the Radder Parabolic approximation is no longer
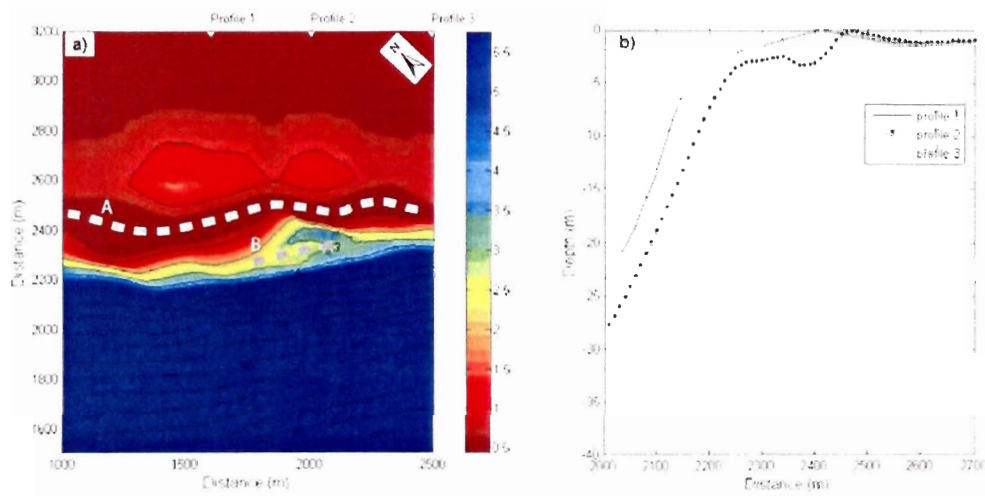
Figure III-5: a) bathymetric grid used for wave simulation. Dot Line represents bar crests. The 3 upside down triangles indicates the position of cross-shore profile. b) Cross-shore bathymetric profiles; Profile 1 shows only the low tide bar; Profile 2 shows the outer bar and low tide bar; Profile 3 shows no bars.

valid in these extremely shallow water depths. However these cases give useful information in deep water.

In the first simulation (Fig. III-6a), at low tide (1.30 m), waves propagate from the south with near normal incidence. Significant refraction begins in water depths between 1 and 2 m. Incident waves remain unmodified over the outer bar. Over the low tide bar, wave heights increase when refraction causes focusing of wave energy (convergence) and decrease when refraction causes spreading of energy (divergence). No wave breaking occurs.

In the second simulation (Fig. III-6b), also at low tide (1.18 m), the angle of incidence is greater and waves refract northward over the outer bar, creating a non-valid area in shallow water behind it due to angle limitation. A slight clockwise refraction in the north and a slight anticlockwise refraction in the south create a general convergence of waves over the inner bar. The gradual increase of wave height over the bar is due to shoaling processes. Waves do not break on the bar but may break on the tidal flat. However, the amplitude modulation generated by the simulation over the tidal flat prevents direct observation of this.

Major storm condition

The first storm was impossible to simulate because the wave direction was almost parallel to the shoreline. The simulations of major storm conditions were therefore based on conditions from the second storm on 9-10 March.
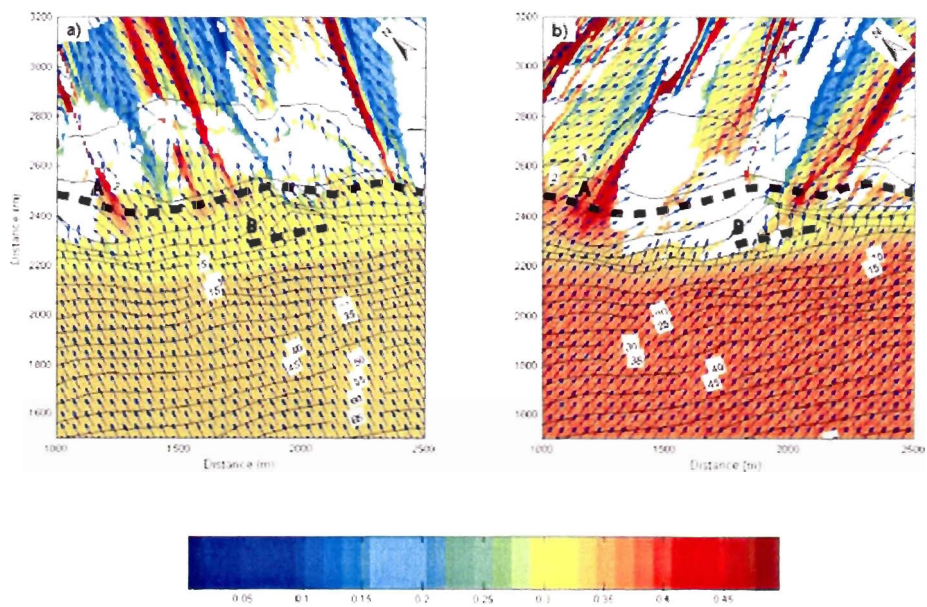
Figure III-6: Wave height simulation during a) the first moderate storm condition and b) during the second moderate storm condition (see table III-1 for parameters). Arrows indicate direction of propagation. Invalid data due to over refraction are indicated by blank area. Contour depth included tidal range are superimposed. Dot Line represents bar crests.

Figure III-7 shows a simulation for a 0.83 m incident wave height at a tide height of 2.46 m during the flood phase of a secondary high tide. Waves from the south start to refract significantly at a depth between 4 and 5 m. Over the outer bar where the incident wave direction is almost normal to the bathymetric contours, waves remain unrefracted and shoal over both bars, with wave height increasing by a few centimetres. In areas where the incident direction is more oblique to the bathymetric contours, refraction over the inner bar and the trough generates large patches of non-valid results due to the angle limitation. Some wave breaking occurs on the bar (indicated by areas of decreased wave height) where refraction caused significant shoaling but a large proportion of the wave energy propagates onto the tidal flats where they probably break again. However, once again, the amplitude modulation generated by the simulation over the tidal flat prevents direct observation of this.

Figure III-8 shows a simulation for a 0.78 m incident wave height propagating from the southwest during low tide (0.53 m). Over the outer bar, waves may refract significantly in a depth around 3 m and shoal. Waves also shoal over the offshore face of the inner bar. Waves break all along the coastline in a depth of 1 m on the inner bar resulting in a substantial decrease in wave height from about 0.9 m to about 0.4 m (Fig. III-9).
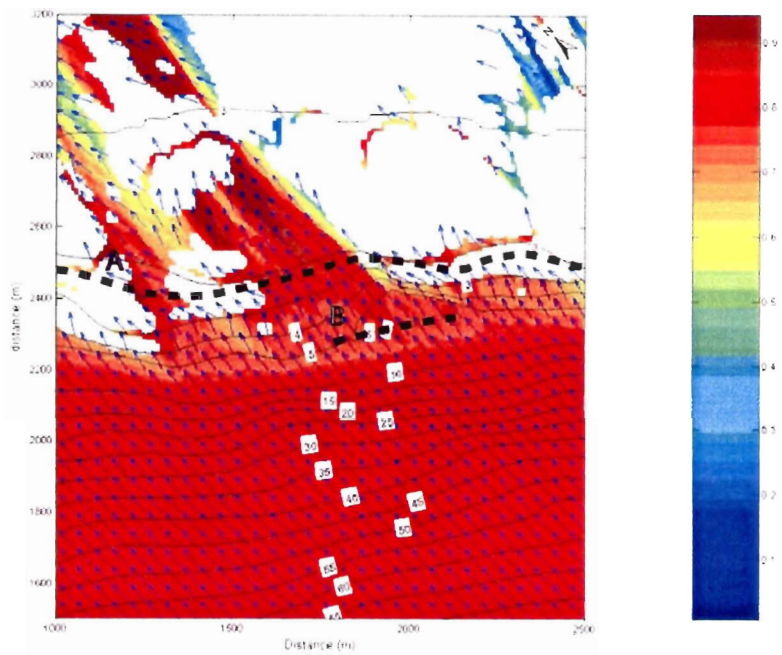
Figure III-7: Wave height simulation during the second major storm condition at high tide (see table III- 1 for parameters). Arrows indicate direction of propagation. Invalid data due to over refraction are indicated by blank area. Contour depth included tidal range are superimposed. Dot Line represents bar crests.
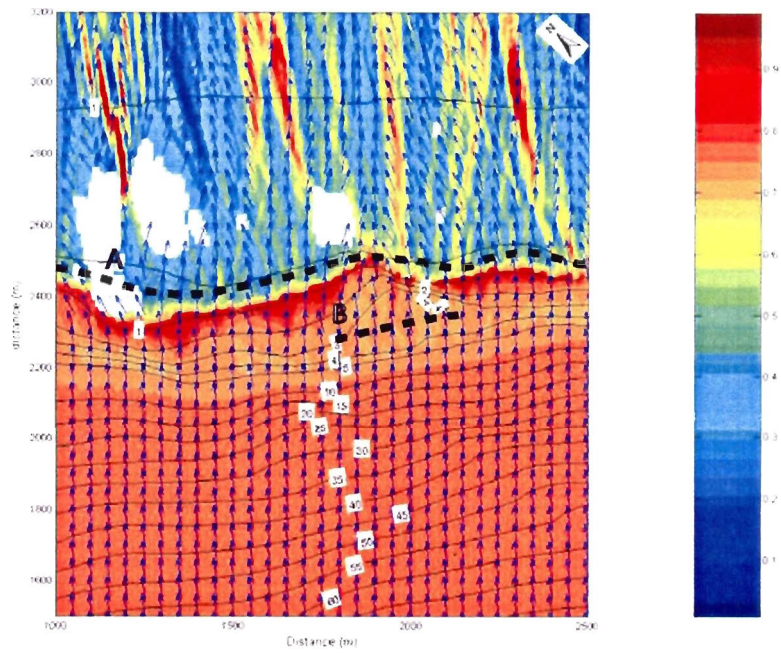
Figure III-8: Wave height simulation during the second major storm condition at low tide (see table III-1 for parameters). Arrows indicate direction of propagation. Invalid data due to over refraction are indicated by blank area. Contour depth included tidal range are superimposed. Dot Line represents bar crests.
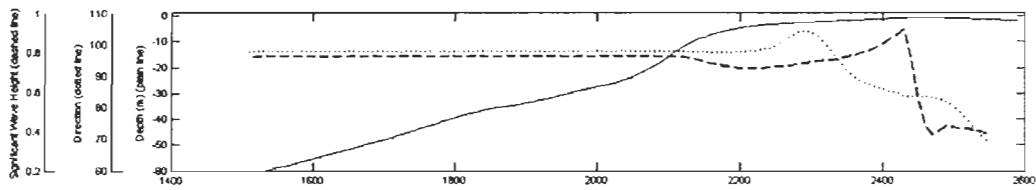
Figure III-9: cross-shore profile superimposing wave height simulation, wave direction simulation and bathymetry during the second major storm (see table III-1 for parameters)

3.4. Discussion

During the field measurements, the winds blew for the longest duration from the southeast where the fetch is limited. Waves were predominantly short period indicating that they were directly wind-induced and did not have swell or infragravity wave components. When winds rotated from south to west, the recorded waves were higher and of longer period. However, wave heights were remained below 1 m. Thomson (1981) and Luternauer *et al.* (1998) calculated that wave heights could exceed 1.2 m for 10 % of the year.

The main limitation of the PARAB model in this setting is the high angle of refractions due to the extreme shallow water of the tidal flat at low tide, making wave parameters fall outside of the valid model domain. Also wave/current interactions were not considered. Although tidal currents are particularly strong in this area, most of the storm peaks in the field measurements occurred coincidently at low tide when the tidal currents were minimal. Furthermore, wave directions were measured in 12 m depth and may already be refracted by tidal current. In this sense the simulations are valid for the observed conditions, but wave/current interactions would more typically be an important consideration. The model runs show an initial gradual decrease of wave height associated with slight refraction in the upper shoreface. Whereas the validity of equation 2 could also be called into question, given the higher slope gradient for the mid slop equation, wave heights decrease by only a few centimeters and are almost negligible.

The model shows that due to the nearshore slope and morphology, waves act non-uniformly along the shore. As waves propagate into shallow water, wave heights and wavelengths change in response to shoaling and refraction processes. Oscillatory wave motions become

significant under moderate storms at a depth between 4 and 6 m. Nielsen (1992) estimates a practical depth of closure as 3.5 times the annual maximum significant wave height beyond sand level changes is insignificant. Assuming values of Hs between 1.3 and a maximum of 3.1 m (Thomson 1981), the upper shoreface slope break coincide with this water depth (see Fig. III-5b).

The behaviour of waves after this point depends on the tide elevation, incident wave angle and the bottom topography. At high tide, small waves propagate into shallow water without any modification. Larger waves refract slowly over the relatively gentle slope and wave energy is progressively dissipated in the shallower water. At low tide, the upper beach is very steep and non-dissipative. When waves propagate into shallow water, oscillatory motions become important on the upper slope. Waves refract over a short distance without shoaling and abruptly break over the inner bar. Calculations suggest breaking would be in the form of a spilling wave. These large variations in significant wave height imply large variations in the spectral energy distribution.

Wave dissipation due to refraction and breaking increases the energy available for sediment transport. The focus of this energy depends on the temporal relationship between tide height, bathymetry and wave height. With the particular bathymetry of this deltaic environment, characterized by a steep slope followed by a shallow, low angle tidal flat the spatial distribution of wave energy due to refraction and breaking varies drastically with the tide height. At high tide, wave energy is more evenly distributed across the tidal flat and sediment transport will be dominated by onshore transport. In contrast, at low tide, the wave energy is highly concentrated at the top of the slope and offshore sediment transport is more likely to

occur. The relative importance of these temporally modulated conditions will determine the degree of net sediment transport divergence across the shoreface.

3.5. Conclusion

1.   During the field measurements on the upper slope of the Fraser River delta, waves were predominantly wind-induced and did not have swell or infragravity wave components. When winds rotated from south to west, the recorded waves were higher and of longer period. However, wave heights were remained below 1m.

2.   The behaviour of waves after the upper shoreface slope break depends on the tide elevation, incident wave angle and the bottom topography. At high tide, waves refract slowly over the relatively gentle slope. At low tide, the upper beach is very steep and waves refract over a short distance without shoaling and may abruptly break in front or over a low tide bar.

3.   Sediment transport divergence in the nearshore will be strongly controlled by the temporal relationship between storm waves and tidal height. At high tide, sediment transport will be dominated by onshore transport. In contrast, at low tide, offshore sediment transport is more likely to occur. The relative importance of these temporally modulated conditions will determine the degree of net sediment transport divergence across the shoreface.

4. SEDIMENT PROCESSES ON THE FRONT OF THE TIDE-DOMINATED FRASER RIVER DELTA, BRITISH COLUMBIA, CANADA: FIELD EXPERIMENTS AND MODELLING

SAMUEL MEULÉ [A,B,C], PHILIP R.HILL [A], CHRISTEL PINAZO [B], IVAN DEKEYSER[B], VLADIMIR[C] KOUTITONSKY.

[A] NATURAL RESOURCES CANADA, GEOLOGICAL SURVEY OF CANADA - PACIFIC, 9860 WEST SAANICH ROAD, P.O. BOX 6000, SIDNEY, B.C., V8L 4B2, CANADA. EMAIL: SAM.MEULE@NRCAN.GC.CA

[B] LABORATOIRE D'OCÉANOGRAPHIE ET DE BIOGÉOCHIMIE, UMR 6535 CNRS/UNIVERSITÉ DE LA MÉDITERRANÉE, OSU/CENTRE D'OCÉANOLOGIE DE MARSEILLE, STATION MARINE D'ENDOUME, CHEMIN DE LA BATTERIE DES LIONS 13007 MARSEILLE, FRANCE. EMAIL: SAMUEL.MEULE@COM.UNIV-MRS.FR

[C] INSTITUT DES SCIENCES DE LA MER DE RIMOUSKI, 310, ALLÉE DES URSULINES, C.P. 3300 RIMOUSKI (QUÉBEC) CANADA G5L 3A1 EMAIL: SAMUEL_MEULE@UQAR.QC.CA

Abstract

An instrumented station was deployed at Roberts Bank between 1 March and 26 March 2002, on the upper delta slope of Roberts Bank in approximately 12 m of water. Waves, currents, and near-bottom suspended sediment concentrations were measured. The calibrated backscatter signal for concentration values were filtered from the tidal harmonics. Two moderate storms and two major storms were identified. Current modelling and calculation of shear velocity induced by combined flows were conducted to understand sediment transport processes. Flood flow is the main forcing mechanism for resuspension. Oscillatory motions resuspend bottom sediment at low tide when tidal current of comparable magnitude may be too weak to initiate sediment motion. Rip-currents induced by wave pressure were identified in both late flood and late ebb tide simulation which generates strong resuspension over the low tide bar. Pressure force due to set-up associated with offshore components of the ebb flow and excess weight force should be strong enough to create large resuspension events and offshore sediment transport.

Keywords: Wave, currents, near-bottom suspended sediment concentrations, backscatter signal, current modelling, shear velocity, combined flow.

4.1. Introduction

Knowledge of the sedimentary processes active on the Fraser River Delta front is needed to address the suitability of specific areas for civil engineering projects, and to understand the ecological sensitivity of deltaic environments. The front of the Fraser River delta is strongly influenced by tidal currents. However, outcropping beds located on the upper slope of the delta are interpreted to be the product of local erosion by tidal currents and shoaling waves (Carle and Hill 2004 submitted). Tides, waves and gravity forces contribute to alongshore flow and intermittent cross-shore flow (Wright *et al.* 1991). The processes of sediment erosion, transport and deposition generated by these different forcing mechanisms occur essentially in the bottom boundary layer, which forms the interface between the seabed and the water column. Their effects on the sediment dynamics take place primarily through the bed shear stress exerted on the seabed. This study examines these relationships between physical processes and sediment transport mode in an environment of combined wave and current motions.

Wave motions, currents and near-bottom suspended sediment concentrations were measured during a winter month-long program on the upper delta slope of the Fraser River Delta, off Roberts Bank. In coastal environments, our understanding of shoreface sedimentary processes during high energy events is often limited by instrumental measurements. The use of an acoustic current profiler provided excellent spatial and temporal resolution of current circulation and gave an indication of particle concentration through the backscatter signal. Numerical modelling provides the opportunity to study the processes of shoreface sediment transport. From field measurements and current modelling, a sediment transport model was

implemented in order to study and identify areas of bedload, resuspension and sheet flow transport.

4.1.1. Study area

The Fraser River delta is located on the southwest coast of British Columbia (Fig. IV-1). Roberts Bank covers the intertidal delta between the Main Arm channel and Point Roberts headland. There are two main morphologic zones of the subaqueous delta (Hart *et al.* 1995): (1) the delta front, at the seaward limit of the tidal flat that extends to approximately 10 m depth. (2) The delta slope, between 10 m and 100 m water depth, with a typical slope 2-3° but reaching locally 23°, is the portion of the delta below the delta front that grades offshore into the prodelta zone (typically <1°). The detailed study area (Fig. IV-1) was chosen for its linear low tide shoreline that was interpreted to be highly wave influenced. The local seabed in water depths less than 20 m is characterised by an area of outcropping beds and large solitary dunes indicating erosional and sediment–starved conditions (Carle and Hill 2004 submitted).

4.1.2. Previous measurements

Meulé *et al.* (2004a submitted) reported on ADCP current and backscatter measurements that were analysed to identify major processes of resuspension and cross-shore transport. In a second paper, Meulé *et al.* (2004b submitted) modeled nearshore wave propagation for the conditions observed during the field program. The results are summarized in a following section.
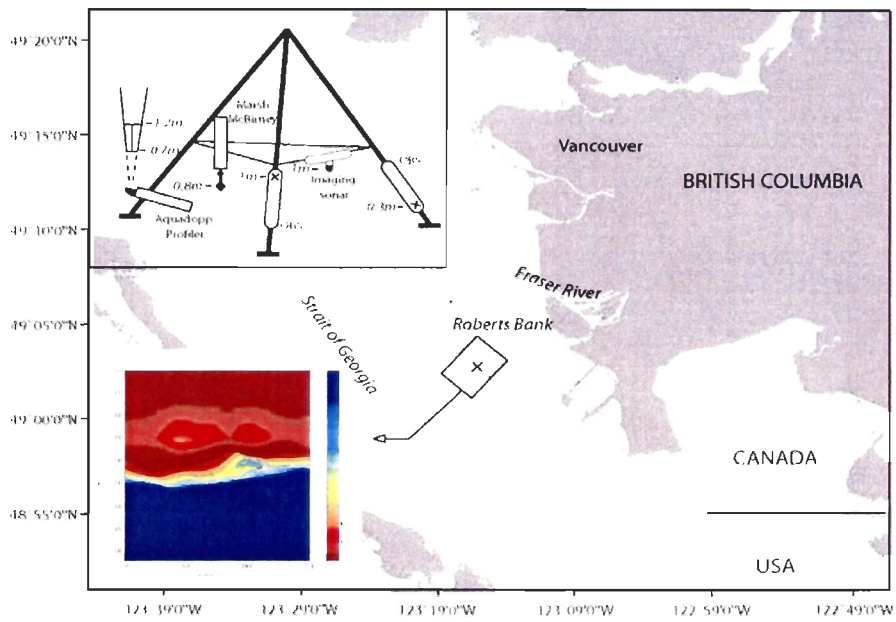
Figure IV-1: Map showing the study area on Roberts Bank, Fraser River Delta, British Columbia, Canada. The location of the mooring and a schematic diagram of the mooring are shown in the insets. The bathymetric grid used for modelling is shown in the lower left corner.

4.2. Methods

4.2.1. Field measurements

The Norton instrumented tripod (Birch *et al.* 2003), was deployed at Roberts Bank (Fig. IV-1) between 1 March and 26 March 2002. From multibeam imagery, the tripod was located in an area of oblique, low relief ridges, of 1 m height and 35 m wavelength in approximately 12 m water depth. A Nortek Aquadopp Profiler permitted directional currents measurements every 50 cm through the water column from 75 cm up to the surface. Velocity and pressure measurements were recorded with a Marsh McBirney current meter located 1m above the seabed. Two optical backscatter sensors (OBS), positioned at 30 cm and 100 cm above the seabed, were used to measure suspended-sediment concentration every minute. These data were calibrated for concentration values using a bottom sediment sample from the same water depth. Correlations between OBS voltage and mass content were high (r^2= 0.99, N= 5, R= [0:200] mg l^{-1}).

4.2.2. Current model

Meulé *et al.* (2004b submitted) used a monochromatic parabolic wave model to simulate different wave conditions over Roberts Bank. The output wave characteristics from this model were used as input to a numerical current simulation model, COURAN (Marcer and Robin 1996; Meulé *et al.* 2001). The current model solves the depth-averaged Navier and Stokes's equations for conservation of momentum and energy:

$$\frac{\partial \overline{\eta}}{\partial t} + \frac{\partial \overline{Q_x}}{\partial x} + \frac{\partial \overline{Q_y}}{\partial y} = 0 \tag{1}$$

$$\frac{\partial \overline{Q_x}}{\partial t} + \overline{U}\frac{\partial \overline{Q_x}}{\partial x} + \overline{V}\frac{\partial \overline{Q_x}}{\partial y} = -g(h+\overline{\eta})\frac{\partial \overline{\eta}}{\partial x} + \frac{1}{\rho}\left(\tau_{xx}+\tau_{xy}+\tau_{bx}+\tau_{wx}\right) + \frac{\partial}{\partial x}\left(\upsilon_{xx}\frac{\partial \overline{Q_x}}{\partial x}\right) + \frac{\partial}{\partial y}\left(\upsilon_{xy}\frac{\partial \overline{Q_x}}{\partial y}\right) + f\overline{Q_y}$$

$$\frac{\partial \overline{Q_y}}{\partial t} + \overline{U}\frac{\partial \overline{Q_y}}{\partial x} + \overline{V}\frac{\partial \overline{Q_y}}{\partial y} = -g(h+\overline{\eta})\frac{\partial \overline{\eta}}{\partial y} + \frac{1}{\rho}\left(\tau_{yy}+\tau_{yx}+\tau_{by}+\tau_{wy}\right) + \frac{\partial}{\partial x}\left(\upsilon_{yx}\frac{\partial \overline{Q_y}}{\partial x}\right) + \frac{\partial}{\partial y}\left(\upsilon_{yy}\frac{\partial \overline{Q_y}}{\partial y}\right) - f\overline{Q_x}$$

(2 and 3)

where $\overline{\eta}$ is the mean surface elevation, $\overline{U}$ and $\overline{V}$ are the mean horizontal currents, $\overline{Q_x}$ and $\overline{Q_y}$ are the mean horizontal fluxes, $\vec{\tau_b}$ is the bed shear stress, $\vec{\tau_w}$ is the wind shear stress (no wind stress was considered). Coriolis effects are negligible on the scale of our study. $\vec{\tau_b}$ the bed shear stress is calculated by the Chezy equation. υ_{ij} is the horizontal eddy viscosity and is calculated by the Fisher partial differential equation. Wave-induced currents are calculated from the Longuet-Higgins (1970) radiation stresses, $\tau_{xx};\tau_{xy};\tau_{yy};\tau_{yx}$. The excess of momentum flux S_{ij} (components of radiation stresses) is calculated from a formulation of Longuet-Higgins and Stewart (1962). The convection step is solved by a first order upwind scheme, the diffusive step is solved explicitly, and the propagative step is solved by an alternative direction scheme. The coast is imposed as an impermeable boundary and Sommerfeld radiation conditions are applied for the lateral open boundaries (Sommerfeld 1949; Miller and Thorpe 1981).

The bathymetric grid used for wave and current simulation is characterized by the presence of a low tide bar and trough system almost parallel to the shoreline in about 2 m of water (Fig. IV-1). A second parallel bar, with a crest depth of 3 m, is located in the central part of the grid and is slightly oblique to the shoreline

4.3. Sediment processes

4.3.1. Acoustic backscatter signal (ABS)

The ABS measured by the Aquadopp Profiler, was initially analyzed to obtain a qualitative view of the suspended sediment concentration (SSC; Meulé *et al.* 2004a submitted). For SSCs below 50 mg l^{-1} as in most of the present data, attenuation due to sediment can be considered to be negligible. Water attenuation was inferred from Aquadopp Profiler measurements of temperature and sound velocity.

In order to estimate the SSC, a regression between the ABS in dB at the first cell above the transducer, and the Optical Backscatter Signal (OBS) – derived sediment concentrations (SSC$_{OBS}$, Hoitink 2004) was carried out. The relation is found to be almost linear for small concentrations (Fig. IV-2). A third order function was then used to take all concentrations into account. A spectral analysis was then conducted on both SSC$_{OBS}$ and SSC$_{ABS}$. Diurnal and semidiurnal tide harmonics were then removed to observe residual suspended sediment due to other processes.

4.3.2. Estimation of bed shear velocity under combined-flow (DYSCO)

Several sediment transport models have been developed to account for a bottom boundary layer influenced by irregular topography (i.e. Grant and Madsen 1986; Van Rijn 1993; Soulsby 1997; Dibajnia and Watanabe 1998; Li and Amos 2001). In this study, calculations of
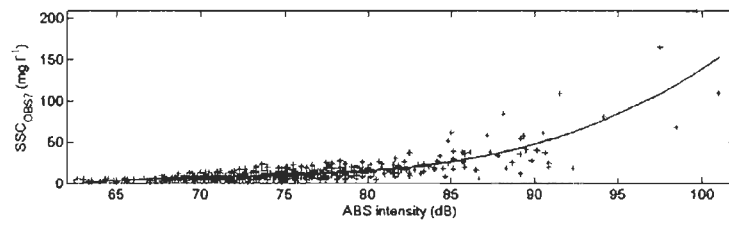
Figure IV-2: Relationship between SSC_{OBS} (mg l^{-1}) and ABS intensity (dB) measured by the Aquadopp profiler at 0.95 m above the seabed. The line represents the third order regression.

bed shear velocity are summarized in this section and were carried out in Matlab scripts grouped in a model called DYSCO ("*DYnamique Sédimentaire CÔtière*")[**].

Taking the Prandtl 1DV model, the integrated velocity profile for a steady current gives:

$$\overline{u} = \frac{u_*}{\kappa} Ln\left(\frac{h}{e^1 z_0}\right) \tag{4}$$

Where ū is the depth averaged velocity, u* is the shear velocity, h is the depth and z_0 is the roughness length.

The oscillatory boundary layer generates frictional effects near the bed. The amplitude of the oscillatory bed shear stress τ_w is calculated from the widely used formulae described by Jonsson (1966):

$$\tau_w = \frac{1}{2}\rho \cdot f_w U_{b\,max}^2 \tag{5}$$

, where ρ is the water density, U_{bmax} is the maximum wave orbital velocity and f_w is the wave friction factor which can be calculated from the following equation (Soulsby 1997) valid for smooth, transitional and turbulent flows:

$$f_w = 1.39\left(\frac{A_b}{z_0}\right)^{-0.52} \tag{6}$$

, where A_b is the orbital amplitude of wave motion near the bed.

The skin-friction shear velocity induced by wave $(u*_{ws})$ or current $(u*_{cs})$, which takes into account only grain roughness, z_0, were calculated for both the field data and the model runs. To compute total shear velocity, the methodology described by Li and Amos (1995; 1998;

[**] DYSCO Matlab[7] scripts are available on
http://samuel.meule.free.fr/   folder: these/download/dysco
login: article ; password: transfer.1

1999a; 1999b; 2001) was used. This method uses the combined wave and current boundary-layer theory of Grant and Madsen (1979; 1986) to determine the combined flow skin-friction shear velocity u_{*cws}. However, shear velocity is enhanced by the presence of ripples and bedforms. The model employs the governing equations of fluid motion in order to describe the velocity field and associated combined flow shear velocity u_{*cw}. The momentum equations are simplified and linearized, providing formulae for the velocities, shear stresses, friction factors and roughness factor. Other methods are described in Soulsby (1997). Soulsby parameterization of the Fredsoe (1984) models is also used in DYSCO to compare with Li and Amos method.

The critical shear stress is computed from the widely used Shield curve modified by Van Rijn (1984). The settling velocity used for critical shear stress for suspension is computed from the Migniot (1981) formulation for semi-turbulent flow. A sheet flow critical shear stress is also computed from Li and Amos (2001).

To compare shear stress to the different thresholds for bedload (u_{*cr}), saltation/suspension (u_{*crs}), and sheet flow/plane bed transport (u_{*up}), the following movement parameter is used:

$$M_* = 1 - \frac{u_{*cr}}{u_*} \text{ , with } M_* = 0 \text{, if } u_* < u_{*cr} \text{, (7)}$$

where u_* can be u_{*ws}, u_{*cs} or u_{*cw} and u_{*cr} replaced by u_{*crs} or u_{*up}.
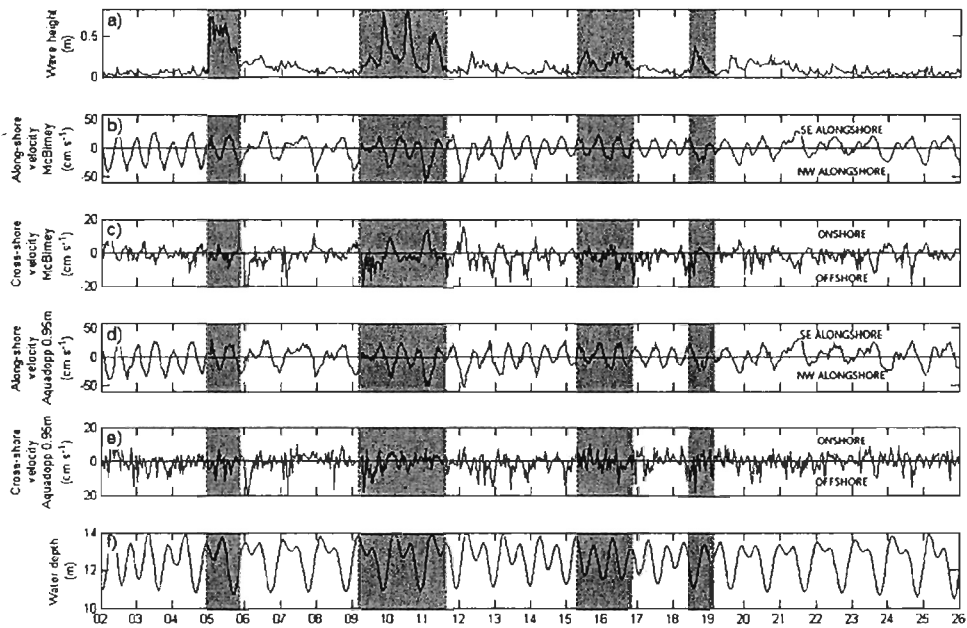
Figure IV-3: Time series of **a)** water depth; **b)** along-shore and **c)** cross-shore velocity measured by the Marsh McBirney; **d)** along-shore and **e)** cross-shore velocity measured by the Aquadopp Profiler at 0.95 m above the seabed; f) mean water depth. Storm periods are shaded in gray.

4.4. Field measurements results

The general oceanographic conditions over the study period are shown in Figure IV-3. Based on the analysis presented in Meulé *et al.* (2004b submitted), the period of measurements can be subdivided into five extended periods of fair-weather conditions and four periods of more energetic conditions including two major storms. The mean water depth shows the mixed semidiurnal tidal oscillation (Fig. IV-3f). At the tripod deployment location, the mean water level was not raised significantly in response to winds and no coastal set up was observed. A general observation confirms previous work (Crean 1976, 1978; Kostaschuk *et al.* 1995, Foreman *et al.* 1995; Meulé et al. 2004a submitted): the tidal currents are strongly bi-directional flowing along the isobaths and the maximum flood flow is stronger than the maximum ebb flow. The variability of the longshore currents (Fig. IV-3b and IV-3d) is strongly influenced by the tidal oscillation while the cross-shore currents (Fig. IV-3c and IV-3e) show a strong turbulent component. The cross-shore velocity measured by the Aquadopp profiler shows also more variability than the cross-shore velocity measured by the Marsh McBirney, due to a larger cell size of measurement.

4.4.1. Fair-Weather Conditions (Days 1–5, 6–9, 12-15, 17-18, 19-27)

Five periods of fair-weather presented similar conditions with significant wave heights less than 0.25 m predominantly coming from south, southwest and northwest (see Meulé et *al.* 2004b submitted).

The SSC_{OBS} and SSC_{ABS} were also observed to strongly respond to the tidal oscillation in a range of 0.1 to 0.3 g l^{-1} for the SSC_{OBS} and 0 to 0.15 g l^{-1} for the SSC_{ABS}. The spectral analysis conducted on the SSC time series over the month shows peaks at semidiurnal and diurnal tidal harmonics (Fig. IV-4) for both OBS and ABS data. The lower part of the water column shows a stronger diurnal signal, whereas the semidiurnal signal is stronger in the upper water column. When the data are filtered from the tidal harmonics, the SSCs show significant re-suspension only during periods of significant wave activity, with the single exception of a major event on March 12 (Fig. IV-5). This event occurred during an ebbing tide at maximum ebb current speed when wave heights were below 0.3 m (Fig. IV-3a). The offshore velocity measured by the Marsh McBirney (Fig. IV-3c) was of the same order (0.2 m s^{-1}) as the southeast alongshore velocity component (Fig. IV-3b). However, this condition was often repeated through the time series with no significant increase in SSC.

4.4.2. Moderate Storm Conditions (Days 15-17, 18–19)

Two moderate storm conditions were observed. These conditions generated short (4 s) to relatively long-period (6 s) waves with significant heights of 0.3 to 0.4 m (Fig. IV-3a), propagating from the south and south-southeast (Meulé et al. 2004b submitted). No significant near-bed suspension of bottom sediment occurred during these periods (Fig. IV-5). The SSC oscillated between 0.1 and 0.2 g l^{-1} during the first moderate storm and around 0.2 g l^{-1} during the second moderate storm but the filtered SSC_{OBS} and SSC_{ABS} show no contribution from wave re-suspension (Fig. IV-5).
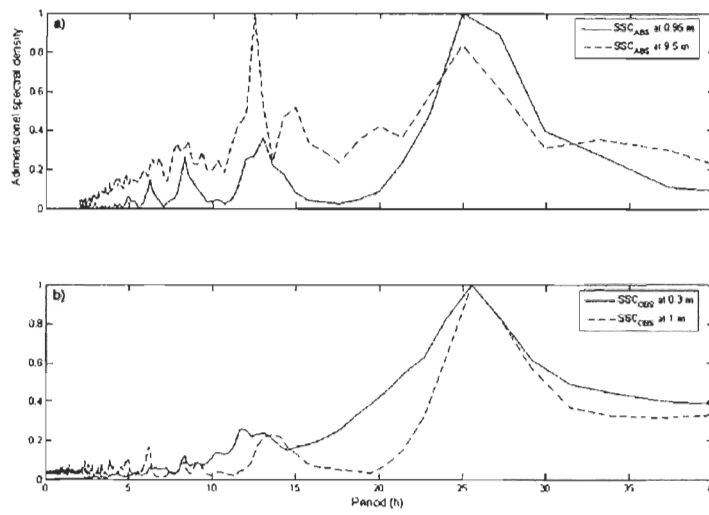
Figure IV-4: Adimensional spectral energy density for the suspended sediment concentration from **a)** the absolute backscatter signal at 0.95 m (plain line) and 9.5 m (dotted line) above the seabed; **b)** the optical backscatter signal at 0.3 m (plain line) and 1 m (dotted line).

4.4.3. Major Storm Conditions (Days 5 ; 9-12)

Day 5 was characterized by a significant storm. Significant wave heights exceeded 0.5 m for twelve consecutive hours and reached 0.74 m, propagating from the northwest. The peak wave periods ranged between 5.5 and 4.5 s (Meulé *et al.* 2004b submitted). The strong combined-flow conditions generated throughout the storm caused major re-suspension of sediment. The filtered-SSC_{OBS} and SSC_{ABS} at both elevations suggest an important contribution from wave action (Fig. IV-5).

A second intense storm lasted three days between March 9 in the morning and March 11. Three peaks of significant wave height (0.77, 0.83, and 0.55 m) were observed. The first two peak events generated relative long period waves (6 and 5.4 s) while the last peak event of this storm was associated with short period wave (4.6 s). Waves propagated predominantly from the south and south-southeast (Meulé *et al.* 2004b submitted). While two distinct peaks up to 0.2 g l^{-1} are visible in the filtered SSC_{OBS} and SSC_{ABS}, no direct correlation between wave height and the first SSC peak could be established. However both SSC events corresponded to the same tidal phase between slack high tide and early ebb tide. In contrast the second significant wave height peak (Fig. IV-3a) is perfectly correlated with the second major resuspension event. Both resuspension events were observed when the weak alongshore velocities were of the same order as cross-shore velocities (between 0.05 and 0.1 m s^{-1}). Figure IV-5a shows a high SSC event in the near-surface water column during the second major storm. It occurs during a high tide phase when waves of 0.3 m significant height were present.
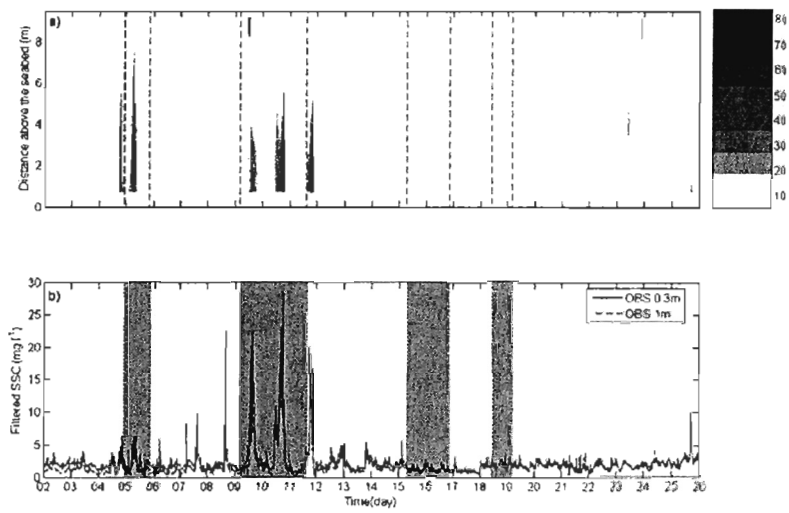
Figure IV-5: Time series of **a)** filtered SSC_{ABS} in the water column. Colorscale is in mg l^{-1}; **b)** filtered SSC_{OBS} at 0.3 m (solid line) and 1 m (dashed line) above seabed.
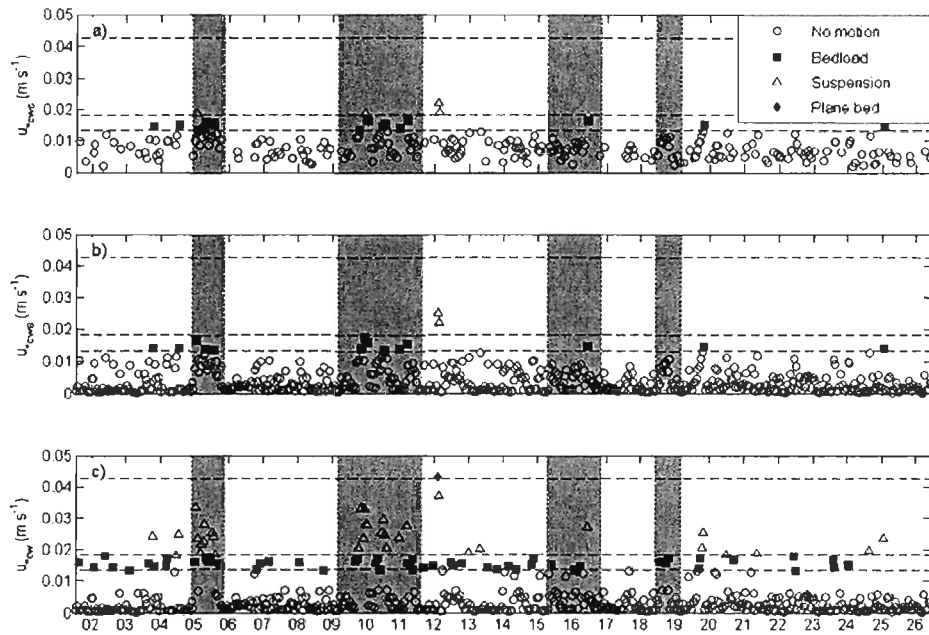
Figure IV-6:   **a)** Time series plot of the skin friction combined shear velocity calculated from field measurements with Soulsby parameterization of the Fredsoe model; **b)** Time series plot of the skin friction combined shear velocity calculated from field measurements using the Li and Amos method; **c)** Time series plot of the total friction combined shear velocity calculated from field measurements using the Li and Amos method. The horizontal lines represent the critical shear velocities for bedload (u_{*cr}), saltation/suspension (u_{*crs}) and sheet flow transport (u_{*up}).

4.5. Field measurements and combined-flow models

Figure IV-6 shows calculated values of the skin friction combined flow shear velocity u_{*cws} (Fig. IV-6a: Soulsby method; IV-6b: Li and Amos method) and combined flow shear velocity adjusted for the effects of ripples u_{*cw} (Fig. IV-6 c: Li and Amos method) for the measurement time series. When the effects of ripples are ignored, both calculations suggest that bedload sediment transport would have occurred essentially at storm condition and suspended sediment transport would have occurred only rarely. When the roughness due to the presence of ripples is taken into account, the model of Li and Amos (2001) suggests that bedload transport occurs during fair-weather conditions under both flood currents and the strongest ebb currents. Bedload transport is initiated prior to maximum flood flow, at the point of maximum acceleration of the tidal current. Under some of the stronger tidal flows, the suspension criterion is exceeded at maximum flood flow intensity. The suspension criterion is also exceeded under major storm conditions. This corresponds to the high SSC events in the measurement time series (Fig. IV-5), although resuspension under moderate storm condition or weak wave condition was minimal, suggesting a slight over-prediction by the Li and Amos method. The SSC event on March 12 (Fig. IV-5) is the only event observed outside of storm conditions that was computed to have developed sheet flow transport.

Current Simulation	Current Simulation	Current Simulation	Current Simulation	Shear velocity	Shear velocity	Shear velocity	Shear velocity
Figure 7a	Figure 7b	Figure 8a	Figure 8b	Figure 9	Figure 10	Figure 11a	Figure 11b
Late Flood phase	Late Ebb phase	Late Flood phase	Late Ebb phase	Late Flood phase	Late Ebb phase	Late Flood phase	Late Ebb phase
No Wave	No Wave	Wave-induced radiation stress Longuet Higgins	Wave-induced radiation stress Longuet Higgins	Current +Wave	Current + Wave	Current with Wave-induced radiation stress Longuet Higgins	Current with Wave-induced radiation stress Longuet Higgins
N $\bar{u}=0.3$ m s^{-1}	N $\bar{u}=0.1$ m s^{-1}	Hs: 0.83; T=5.07; $\Phi=194.69°$; $\bar{u}=0.3$ m s^{-1}	Hs: 0.78; T=5.39; $\Phi=214.73°$; $\bar{u}=0.1$ m s^{-1}	Hs: 0.83; T=5.07; $\Phi=194.69°$; $\bar{u}=0.3$ m s^{-1}	Hs: 0.78; T=5.39; $\Phi=214.73°$; $\bar{u}=0.1$ m s^{-1}	Hs: 0.83; T=5.07; $\Phi=194.69°$; $\bar{u}=0.3$ m s^{-1}	Hs: 0.78; T=5.39; $\Phi=214.73°$; $\bar{u}=0.1$ m s^{-1}

Table IV-1: Wave and current parameters for the simulations. Conditions were chosen to simulate late flood tide and late ebb tide during major storm conditions.
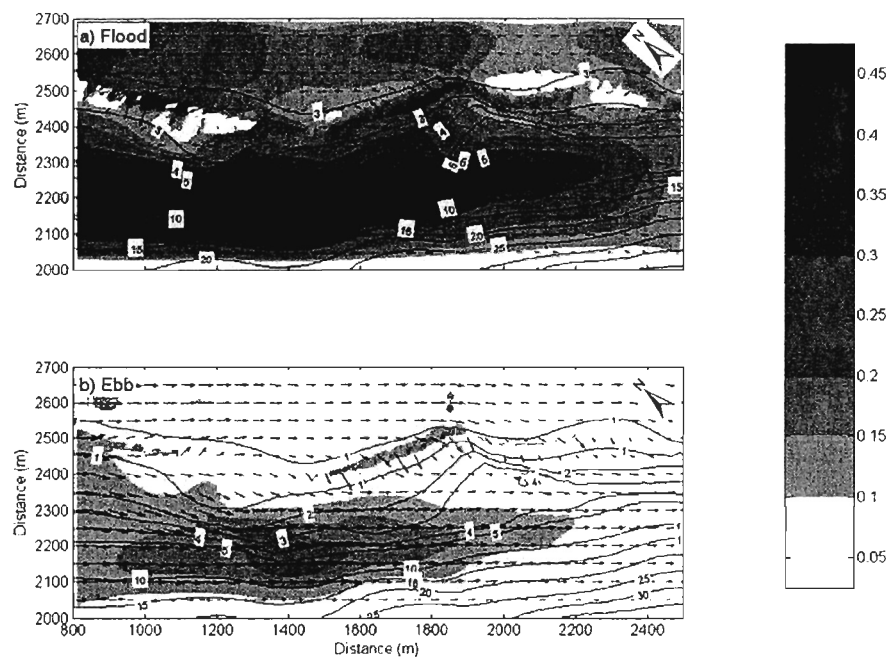
Figure IV-7: Flow pattern simulated for **a)** late flood tide and **b)** late ebb tide. The colorscale represent current magnitude in m s^{-1}. See table IV-1 for characteristics.

4.6. Current modelling and combined-flow models

Meulé *et al.* (2004b submitted) showed that the wave behaviour, above the upper shoreface slope break of the Fraser delta, depends on the tide elevation, the incident wave angle and the bottom topography. Based on this previous work, conditions from the second major storm were selected for detailed combined flow modelling. Table IV-I summarizes the parameters used in the numerical calculation. Current direction and intensity, and the different movement criteria M∗ for bedload, suspension and sheet flow on each point of the 2D grid are plotted as results.

4.6.1. Tidal flows

Figure IV-7 represents the current flow pattern simulated without any wave for both late flood tide ($\bar{u}$=0.3 m s^{-1}) and late ebb tide ($\bar{u}$=0.1 m s^{-1}). Behind the low tide bar for both situations, the smooth topography does not disturb the tidal flow which remains alongshore. In the shallowest water, strong dissipation diminishes the current intensity, which almost disappears. In the southeastern part, flood flows (Fig. IV-7a) are deviated shoreward by the presence of the outer bar between 4 and 5 m water depth. Flood flows are then accelerated above the low tide bar. In the northwestern part of the grid, these flows cross back over the low tide bar, converging with the main alongshore current. Both bars induce deviation of the flow creating an area of strong currents in deeper water in the northwestern part of the grid. The same area exists in the ebb simulation (Fig. IV-7b with boundary condition $\bar{u}$=0.1 m s^{-1}) but the ebb flow has a slight onshore component directed toward the low tide bar in the northwestern part of

the grid, while in the central and southern part the ebb current flows across the low tide bar with an offshore component.

4.6.2. Wave-modified tidal flows

Figure IV-8 shows the simulated flow pattern modified by wave propagation through radiation stress of Longuet-Higgins for both late flood tide ($\bar{u}=0.4$ m s^{-1}; Fig. IV-8a) and late ebb tide ($\bar{u}=0.1$ m s^{-1};Fig. IV-8b). In the deeper water, the main tidal flows are almost unmodified. During the flood high tide situation (Fig. IV-8a), a stronger current is simulated over the low tide bar and in the northwestern part of the grid, complex circulation cells appear. During the ebb low tide situation, the water level is 2 m lower than the flood situation and the energy dissipation is stronger for the shallower water. Shoreward of the low tide bar, a local setup due to the convergence of wave rays induces a strong offshore current. Large circulation cells exist and seaward-directed rip currents may cross the low tide bar.

4.6.3. Combined current-wave shear velocity

Under late ebb tide conditions (Fig. IV-7b) the skin friction shear velocity induced by the current alone is not sufficient to generate any sediment transport. However under late flood tide conditions, the flow generates a small zone of transport and, thus, potential erosion. The area of potential erosion is located in front of the low tide bar between 4 and 10 m water depth, where the current shows a strong acceleration (Fig. IV-7a).

111
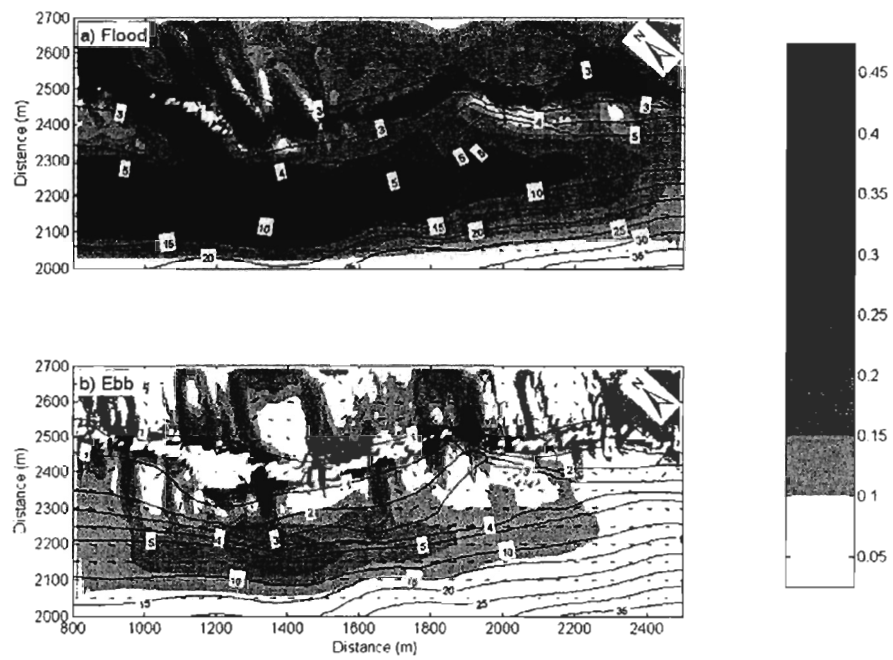
Figure IV-8: Flow pattern in presence of storm wave simulated for **a)** late flood tide and **b)** late ebb tide. The colorscale represent current magnitude in m s⁻¹. See table IV-1 for characteristics.

The shear velocity parameters M*, presented for the late flood tide situation in Figure IV-9 and for the late ebb tide situation in Figure IV-10, used wave and current parameters combined through the Li and Amos method. Due to a limitation of the maximum angle of refraction in the wave model (see Meulé *et al.* 2004b submitted), some invalid areas were eliminated and are shown in white. The combined wave and current shear velocity shows large region where the shear velocity is above the threshold for bedload movement (Fig. IV-9a- IV-10a), for suspension (Fig. IV-9b- IV-10b) and for sheet flow (Fig. IV-9c- IV-10c). In the late flood tide case, bedload is initiated in 15 m water depth and the strength of this mode of transport increases shoreward to a maximum over the bar. Suspension is initiated between 15 and 10 m water depth while sheet flow transport (plane bed) is initiated between 4 and 5 m water depth. Consequently, the low tide bar is under sheet flow transport, and the outer bar is under suspension transport.

During ebb conditions, waves influence drastically the shear velocity and the model predicts almost continuous upper-plane-bed traction transport (Fig. IV-10c) from around 10 m water depth toward a maximum in front of the low tide bar.
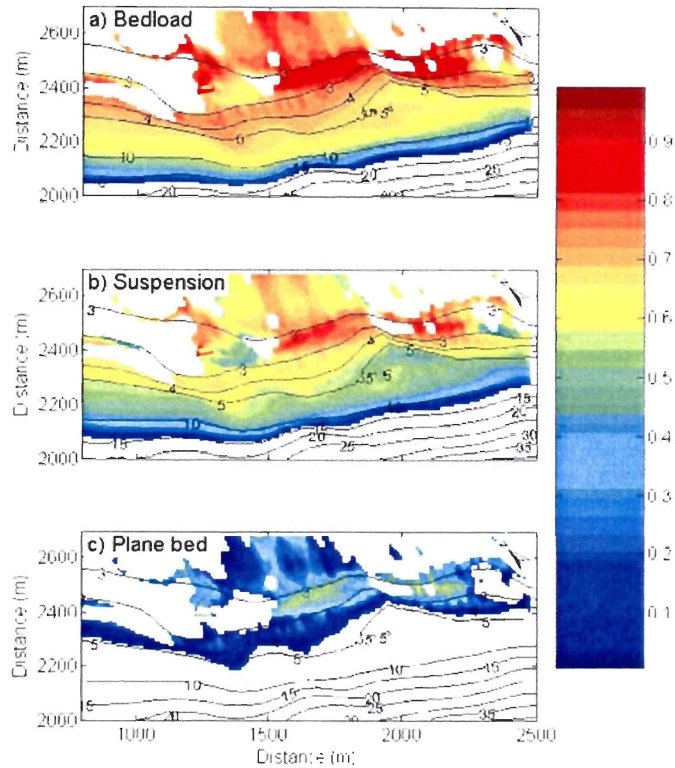
Figure IV-9: 2D representation of e M*, parameter for initiation of movement during the *late flood tide* from total friction combined shear velocity calculated from distinct wave and current simulation with Li and Amos method; **a)** Initiation of bedload transport; **b)** Initiation of saltation /suspension transport; **c)** Initiation of sheet flow/plane bed transport. See table IV-I for characteristics.
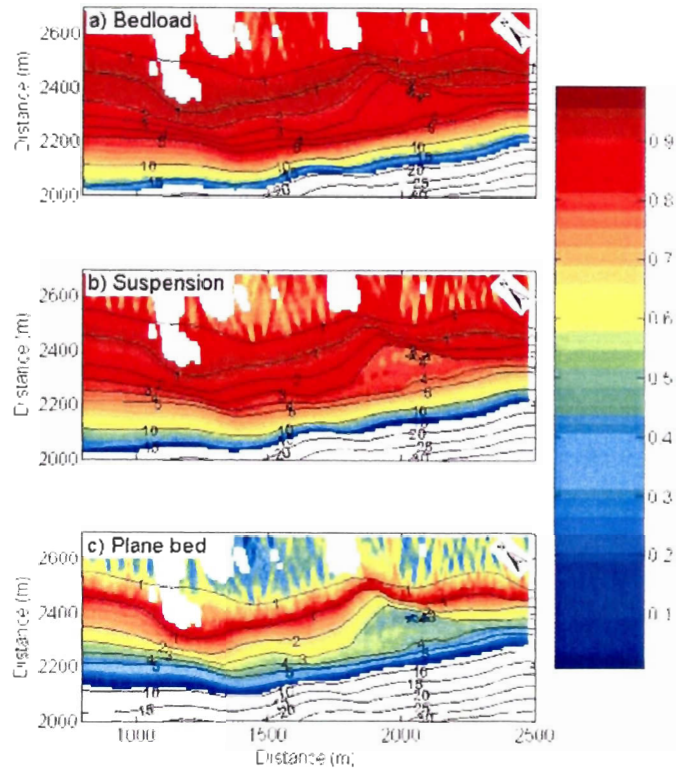
Figure IV-10: 2D representation of M∗ parameter for initiation of movement during the *late ebb tide* from total friction combined shear velocity calculated from distinct wave and current simulation with Li and Amos method; **a)** Initiation of bedload transport; **b)** Initiation of saltation / suspension transport; **c)** Initiation of sheet flow/plane bed transport. See table IV-1 for characteristics.

4.6.4. Shear velocity induced wave-modified tidal flows

Figure IV-11 represents the shear velocity parameter M* for bedload transport during both flood high tide (Fig. IV-11a) and ebb low tide situations (Fig. IV-11b) from simulations using a second method where the current is modified by wave propagation through the radiation stress of Longuet-Higgins (1970). The shear velocity is calculated using the Prandtl equation (eq. 4) as if induced by a steady current. In the flood high tide case, sediment transport is initiated between 10 and 15 m water depth (Fig. IV-11a). The shear velocity parameter has maximum values (transport by suspension reached) over the low tide bar, in small areas related to the circulation cells observed in the current model (Fig. IV-8a). In areas of strong dissipation, flows almost vanish and no transport is predicted. In the ebb low tide case, the transport pattern is more disparate (Fig. IV-11b). Transport is only predicted in the front and in the lee of the low tide bar along the rip-current patterns observed in Figure IV-8b. The suspension criterion is exceeded in front of and in the lee of the low tide bar, but no upper-plane-bed traction transport is simulated.
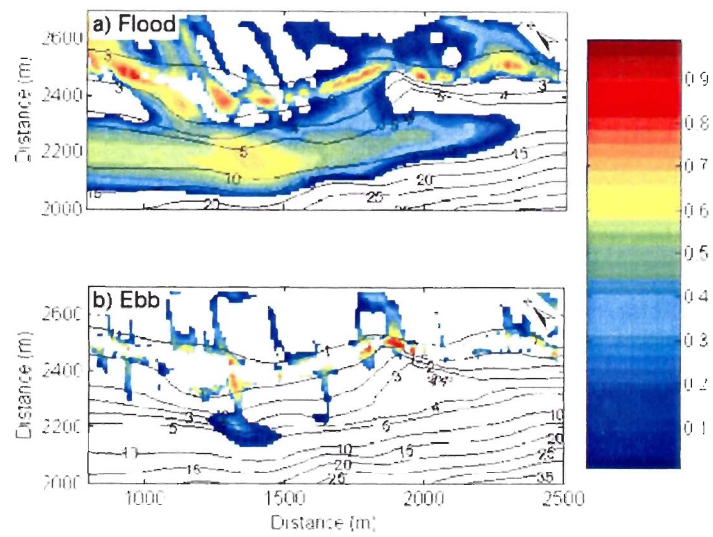
Figure IV-11: 2D representation of M. , parameter for initiation of bedload transport from total friction current shear velocity for **a)** late flood tide and **b)** late ebb tide. In this simulation, the current pattern is modified by the wave propagation through the radiation stress of Longuet-Higgins (1970). See table IV-I for characteristics.

4.7. Discussion

Modelling nearshore sediment transport is a challenge due to the need to combine the steady and the oscillatory components of the flow. In addition, several other effects such as the mean water level variation, breaking waves and topography must be considered. These parameters induce different types of transport with very different physical implications for the movement of sand. Camenen and Larroudé (2000; 2003) showed how major differences between models result from the inconsistent treatment of parameters such as grain diameter, wave orbital velocity, wave period, wave asymmetry or steady current. It appears also that significant errors in the sediment transport computation can be introduced through the calculation of total roughness. For these reasons, the estimation of sand transport from the various formulae can vary by over an order of magnitude. In the present study, the application of the 1D model DYSCO using output parameters from 2D wave and current models, while based on realistic initial inputs, include similar uncertainties. Consequently, the numerical simulations presented here should be considered as cautious attempts to help our understanding of sediment processes on Roberts Bank. If nothing else, they show how spatially variable sediment transport is, even with a relatively simple topography and simple input parameters.

Figure IV-12 provides a schematic summary of the processes suggested by the simulations on the upper delta slope of the study area during a storm at late flood tide (Fig. IV-12a) and late ebb tide (Fig. IV-12b). Topography is a major control on nearshore sediment transport, determining in large part whether the combination of different forces results in an alongshore transport of resuspended sediment and/or a cross-shore transport.

a) Late flood Tide

Rip current

Breaker zone

Wave propagation

b) Late ebb Tide

Pressure force
due to set-up

Breaker zone

Rip current

Wave propagation
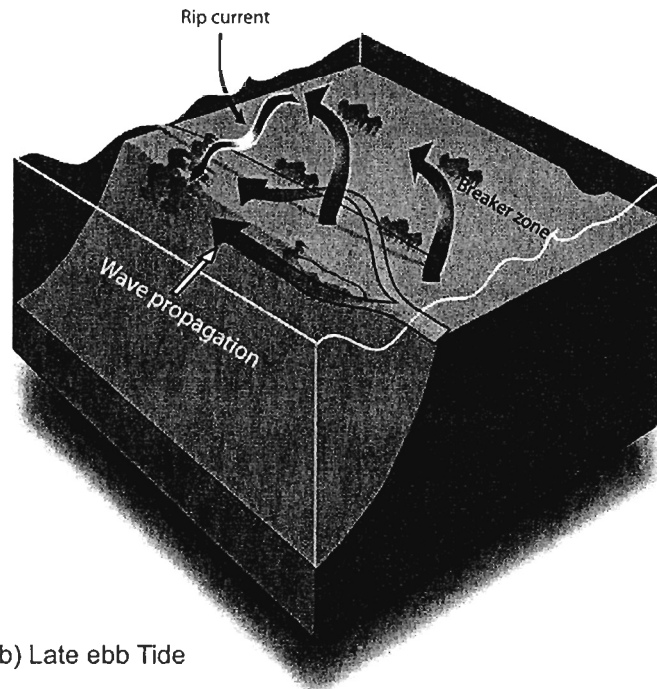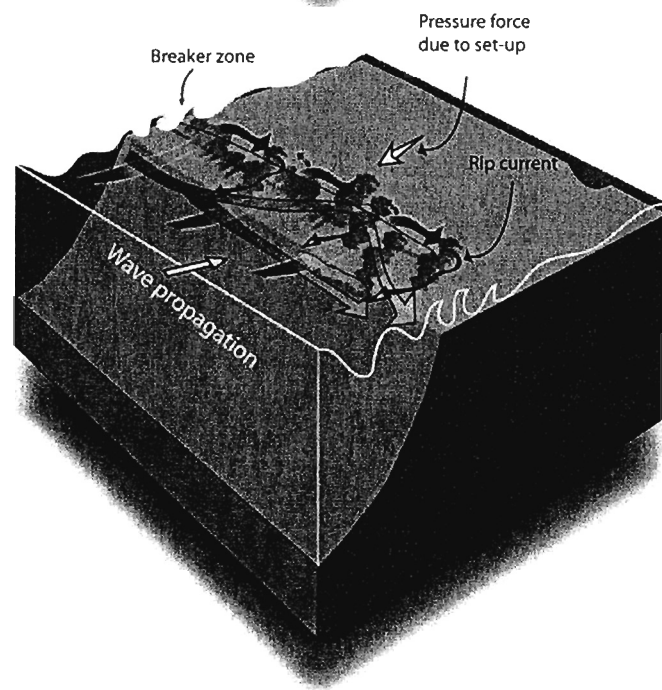
Figure IV-12: Schematic summary of the suspended sediment processes observed during a storm on the upper

delta slope of the Fraser River at a) late flood tide, and b) late ebb tide.

119

4.7.1. Tidal current only sediment transport

The field data presented here show that the tidal currents, in the absence of waves, are sufficient to initiate sediment movement and resuspend sediment from the bottom between 4 and 10 m water depth (Fig. IV-4). Multibeam imagery shows that the seabed in these water depths is characterized by erosional features (Carle and Hill 2004 submitted). Meulé *et al.* (2004a submitted) suggested that sediment resuspension in the flood flow may be enhanced by the rough seabed of the upper delta slope (channels, subaqueous dunes and outcropping beds). However, while resuspension due to the bed roughness may be important locally, the flood flow simulation (Fig. IV-7a) indicates that the main alongshore current interacts with the larger scale bottom topography causing acceleration of the flow in a range of 4-10 m water depth. The flow vectors also indicate a component of offshore transport.

The simulation of the late ebb tide current (Fig; IV-7b) shows a similar acceleration but the resultant skin friction shear velocity is insufficient to generate any sediment transport. However, the numerical results suggest that if we had simulated the ebb tidal current at maximum ebb tide acceleration some sediment transport would have occurred.

4.7.2. Wave and wave-current sediment transport

Wave dissipation due to refraction and breaking increases the energy available for sediment transport. Using the Li and Amos method for combined current-wave shear velocity (Fig. IV-7, IV-9 and IV-10), DYSCO shows that the added energy of waves is sufficient to cause resuspension during the late ebb tide. The boundary shear stress associated with the wave

motion, is an order of magnitude larger than the boundary shear stress associated with tidal currents of comparable magnitude (Grant and Madsen 1979; Glenn and Grant 1987) due to the formation of an oscillatory wave boundary layer within the steady current boundary layer. The result is that waves are capable of resuspending bottom sediment when a current of comparable magnitude may be too weak to initiate sediment motion (Fig. IV-12a). However, Camenen and Larroudé (2003) concluded in their numerical study that models based on the Grant and Madsen method tend to overestimate wave-current interaction (see also Hill *et al.* 2003 , in annexe A1).

The combined wave and current approach of the Li and Amos method, while valid for deep water, does not take into account very shallow water processes induced by radiation stresses (Longuet-Higgins 1970; Figs. IV-8 and IV-11). The wave induced pressure exerted as waves propagate towards shore creates longshore, rip and other nearshore currents and the flow pattern in the presence of waves is modified. Rip-currents were identified in both late flood and late ebb tide simulations but were more strongly defined at late ebb tide situation when the water level was lower and the low tide bar acts very much like a beach (Fig. IV-12b). Waves propagating shoreward induce a stronger pressure in the late flood tide than in the late ebb tide case, enhancing the sediment transport due to the current alone. However, in the late ebb tide case, the additional shear stress exerted by the waves is necessary to exceed the threshold of sediment motion.

4.8. Conclusion

(1) The shoreface at Roberts Bank is a tide dominated environment. Flood flow is the main forcing mechanism for resuspension. Bottom topography, specifically the low tide bar and the outer bar, induce convergence of the flow in the offshore forming an area of accelerated currents and erosion between 4 and 10m water depth.

(2) Storm waves enhance sediment transport processes, resuspending bottom sediment even at late ebb tide when the current alone is too weak to initiate sediment motion.

(3) Rip-currents were identified in both late flood and late ebb tide simulations. The wave-modified current at high tide generates strong resuspension over the low tide bar. At low tide, the induced sediment motions are weaker and the sediment transport is dominated by the rip-current pattern.

5. DISCUSSION

L'étude des mécanismes de mise en suspension et de transport des sédiments sur la plage de sable fin de Roberts Bank a été menée lors de deux périodes de mesure. Des phases de modélisation de la houle et des courants ont été conduites en parallèle. La première période de mesures effectuée entre le 29 juin et le 8 juillet 2001, a permis l'identification de processus hydrodynamiques et sédimentaires associés aux forts courants de marée présents le long de Roberts Bank. La seconde phase de mesures effectuée entre le 1er mars et le 26 mars 2002, a permis d'étudier les processus de remise en suspension associés à la houle. Les modèles ont été implémentés à partir des données acquises sur le terrain. Ils ont permis de compléter ainsi notre connaissance des variables et des processus de l'hydrodynamique sédimentaire notamment dans l'interaction houle - courant - sédiment.

Ce chapitre rassemble les différents processus identifiés dans chacun des articles afin d'établir le lien entre les différentes échelles : l'échelle conceptuelle du processus et celle de la dynamique sédimentaire de la zone.

5.1. Processus sédimentaires lors du flot de marée

De nombreux indicateurs morphologiques, telles que les dunes sous-marines et les surfaces d'érosion affleurantes, attestent d'un refaçonnage régulier et intense de la pente deltaïque par les courants de marée et les houles (Carle et Hill 2004 soumis). Les données présentées dans ce manuscrit montrent que l'intensité des courants de marée est suffisante pour initier un mouvement et une remise en suspension des sédiments (Fig. II-5 ; IV-4). Il apparaît

également que les courants de flot sont le moteur principal de cette remise en suspension (Fig. II.14).

A partir des données de la mission Fraser 2001, une valeur seuil de 0.6 m s^{-1} pour l'intensité du courant a été déterminée. Au dessus de cette limite, une remise en suspension a été observée sur les levées de signaux rétrodiffusés. Cette limite a été atteinte seulement lors des maxima d'intensité des courants de marée montante, à des profondeurs inférieures à 25 m. Les sédiments ont alors été remis en suspension, parfois sur toute la colonne d'eau. A plus de 25 m de profondeur, le mécanisme de remise en suspension des sédiments par les courants de marée n'a pas été observé. Pour des simulations de courant en fin de flot (condition limites de COURAN $\bar{u}$=0.4 m s^{-1}), les résultats de DYSCO indiquent que les zones de remise en suspension se situent au pied de la barre de marée basse ou subtidale (*"low tide bar"*), entre 4 et 10 m de profondeur, là où les courants présentent une forte accélération. Des simulations menées avec des valeurs proches ($\bar{u}$=1 m s^{-1}) de celles observées lors de la mission Fraser 2001, localisent la limite inférieure de remise en suspension à environ 20 m de profondeur.

A l'approche de la situation d'étale, les courants de flot diminuent d'intensité ($\bar{u}$ <0.3 m s^{-1}) et les particules vont sédimenter rapidement. Ainsi à l'étale de haute mer, les eaux ne sont plus chargées en particules en suspension. Cela paraît raisonnable étant donnée une vitesse de chute, calculée par la loi de Stokes et corrigée pour des sédiments naturels par Baba et Komar (1981), de 1.75 cm s^{-1}, soit de l'ordre d'un mètre par minute.

L'évolution du signal rétrodiffusé sur des profils consécutifs recueillis lors de la mission Fraser 2001 indique des changements relativement rapides dans la structure des nuages de sédiment en suspension. L'advection d'une énergie cinétique de la turbulence est donc

importante, spécialement dans les eaux peu profondes. De nombreuses structures de petite échelle sont observées sur le relevé de vitesse de la figure II-5 suggérant l'existence de phénomènes de turbulence. Les relevés de sédiments en suspension (Fig II-8) confirment également l'existence de ces mêmes structures de petite échelle. Cette circulation complexe est reproduite par le modèle de courantologie notamment au dessus de la barre subtidale (Fig IV-7). Le haut niveau d'intensité de turbulence explique également la faible cohérence, près de la côte, des données d'ADCP lors de la mission Fraser 2001. Cette faible cohérence justifie également l'utilisation d'un filtre sur un grand nombre de données lors du traitement.

La turbulence des courants de flot est générée par la rugosité de fond parfois à méso-échelle liée à la présence de chenaux, des dunes sous-marines et des surfaces d'érosion affleurantes qui caractérisent le fond sédimentaire sur la partie supérieure de la pente deltaïque. De manière similaire la remise en suspension des sédiments se fait au niveau de cette rugosité structurelle (Fig. II-8, II-14). Les études antérieures ont montré que la remise en suspension des particules se fait lors d'événements d'éjection turbulente sur le flanc aval et à la crête de la dune (Sumer et Deigaard 1981 ; Kostaschuk et Church 1993 ; Garcia et Admiraal 1998 ; Lecouturier *et al.* 2000). Les figures II-8b et II-8c montrent que les nuages de sédiment en suspension s'étendent depuis les crêtes des dunes notamment celles associées aux embouchures des chenaux sous marins du Passage de Canoë. Carle et Hill (2004 soumis) ont noté que les embouchures de ces chenaux ont été rapidement remaniées. Le matériel érodé participe alors à la formation de nouvelles dunes allongées isolées. Les données confirment sans équivoque que ce refaçonnage est très actif notamment pendant les phases de marée montante.

Lors de la mission Fraser 2001, un transport vers le large de particules en suspension a été observé (Fig. II-12, II-14). Ce phénomène doit toutefois être considéré avec précaution. Les mesures ont été faites au dessus du chenal de Roberts Bank et semblent indiquer qu'un nuage de sédiment en suspension a été généré par une remise en suspension de particules provenant des eaux peu profondes. La composante principale du courant est pourtant parallèle à la côte, et non transversale. Le nuage observé a donc très certainement été advecté de plusieurs centaines de mètres le long de la pente. Il est peu probable qu'un courant de turbidité ait facilité ce transport vers le large. Toutefois, la présence d'un nuage de particules en suspension à une profondeur supérieure à 50 m indique bien un transport significatif vers le large. Malgré la grande variabilité des données de courant, une légère composante vers le large peut être distinguée (Fig. II-4). De plus les simulations de courants de flot (Fig. IV - 7a, IV-12) indiquent que les courants principaux le long de la côte sont contraints par la morphologie sous-marine (dans le cas des simulations il s'agit de la barre subtidale et de la barre externe) et peuvent comporter une composante vers le large. Associé à des courants de downwelling et des mouvements gravitaires (Fig. II-14 ; Myrow et Southard 1996), l'intensité du courant peut alors être assez forte pour contrebalancer l'effet de la force de Coriolis, qui agit dans le sens du haut de la pente lors du courant de flot. Dans ce cas, il peut y avoir un transport sédimentaire vers le large.

5.2. Processus sédimentaires lors du jusant de marée

Les simulations de vitesse de frottement montrent que les courants de jusant en fin de marée descendante ($\bar{u}_{max}$=0.25 m s^{-1}) ne permettent pas le transport des sédiments. Toutefois, les données de la mission Fraser 2001 indiquent que les courants de jusant peuvent être juste

assez fort pour permettre une remise en suspension de sédiments plus fins présents dans les eaux peu profondes de la partie supérieure du front deltaïque.

Un transport sédimentaire vers le large se produit également lors des marées descendantes (Fig. II-14b). Le fort gradient, dans le signal rétrodiffusé dans les premiers mètres depuis la surface, que l'on observe sur la figure II-12 (09.05 hrs) suggère un certain degré de stratification malgré une intensité de turbulence modérée créée par les courants de jusant. Ce panache de surface, qui se développe pendant le jusant, a probablement son origine dans la remise en suspension de sédiment par les courants de jusant dans les eaux peu profondes et par les courants empruntant les larges chenaux de marée qui incisent le marais deltaïque juste au Nord de la boite B2 (localisation en Fig. II-1). Des observations de terrain suggèrent que les courants dans les chenaux drainent des sables fins et très fins en suspension jusqu'au front deltaïque.

En fin de marée descendante et lors de la période d'étale, il y a une rapide sédimentation (Fig. II-12, 09.54 – 12.19 hrs). Maxworthy (1999) et McCool et Parsons (2004) suggèrent que l'interaction de la charge en suspension avec le forçage turbulent peut augmenter la vitesse de chute des particules. Avec une concentration significative de sables fins en suspension, le mélange entre le courant gravitaire de densité et le fluide ambiant plus dense, produit des instabilités gravitationnelles ; les sédiments sont alors entraînés vers le bas. Le panache convectif résultant déplace rapidement les sédiments de la couche de surface vers le fond par un processus dit de "sédimentation convective induite par un mélange" ("*Mixing-induced convective sedimentation*"). McCool et Parsons (2004) ont récemment observé ce processus pour des concentrations bien en dessous de 1000 mg l^{-1}. Les concentrations observées dans le panache varient entre 15 et 60 mg l^{-1}.

Carle et Hill (2004 soumis) montrent qu'il y a eu dans le passé des courants gravitaires actifs dans le chenal de Roberts Bank. Toutefois ce chenal n'est plus actif actuellement et des observations de données morphologiques et sismiques suggèrent qu'il est en phase de remplissage par des sédiments relativement fins. Les données présentées dans ce manuscrit indiquent que ce remplissage pourrait être associé au phénomène de "sédimentation convective de mélange."

5.3. Processus sédimentaires associés à la recombinaison houle-courant

Dans un contexte macrotidal, les résultats présentés dans les $2^{ème}$ et $3^{ème}$ articles montrent que les courants oscillatoires et les courants induits par la houle à la côte peuvent jouer un rôle important sur la partie supérieure du front deltaïque de Roberts Bank.

Durant la période de mesure de la seconde mission Fraser 2002, les vents ont soufflé pendant une longue période du Sud-Est où le fetch est limité (Fig. III-2a). Les périodes des vagues ont été courtes indiquant des vagues de vent. Aucune composante de houle ou d'ondes infragravitaires n'a été observée. Lorsque les vents ont tourné du Sud à l'Ouest, les vagues enregistrées ont été de plus longues périodes et plus hautes, en restant toutefois en dessous du mètre. Thomson (1981) et Luternauer *et al.* (1998) ont toutefois calculé que les vagues pouvaient dépasser 1.2 m pendant 10 % de l'année.

Afin de comprendre l'impact de ces événements de tempête sur le transport sédimentaire littoral, le modèle de houle PARAB a été utilisé. Son utilisation a cependant été limitée en terme de capacité angulaire. En effet, les forts angles de réfraction dans les eaux très peu profondes du marais deltaïque sortent du domaine de validité du modèle. De plus la réfraction de la houle par les courants n'a pas été considérée. Toutefois, la plupart des pics de tempête coïncident avec des périodes de marée basse et de très faibles courants d'étale. Egalement la houle a été mesurée dans environ 12 m d'eau, et les directions calculées présentent très certainement un effet de la réfraction par les courants de marée. De ce point de vue, les simulations entreprises avec PARAB sont valides.

Le modèle de houle montre une diminution graduelle de la hauteur de houle associée avec une très faible réfraction sur la partie supérieure de la pente deltaïque. En ce point, la validité de l'équation 2 dite "mid slope" peut être remise en cause du fait du très fort gradient de pente. Toutefois, cette diminution de la hauteur n'est que de quelques centimètres et peut donc être négligée.

Le modèle montre que du fait de la pente et de la morphologie, les vagues agissent de manière non–uniforme le long de la côte. Rappelons que cet environnement deltaïque est caractérisé par une pente raide suivie par un marais deltaïque relativement plat et peu profond. Lorsque les vagues se propagent vers la côte, les hauteurs et les longueurs d'ondes se modifient en réponse aux processus de *"shoaling"* et de réfraction. Les mouvements oscillatoires deviennent significatifs lors de tempêtes modérées à une profondeur entre 4 et 6 m. Nielsen (1992) estime une profondeur de fermeture au delà de laquelle le niveau de changement sédimentaire est insignifiant. Celle-ci est estimé à 3.5 fois la hauteur significative maximale (Hs_{max}) annuelle. En considérant des valeurs de Hs_{max} entre 1.3 m et un maximum de 3.1 m

(Thomson 1981), la profondeur de fermeture estimée coïncide avec la rupture de la pente deltaïque (III-5b). Le comportement des vagues au delà de ce point dépend du marnage, de l'angle d'incidence et de la morphologie sous-marine. A marée haute les petites houles se propagent dans les eaux peu profondes sans modification. Les vagues les plus importantes se réfractent sur une pente faible et l'énergie est progressivement dissipée (Fig. IV-11a). A marée basse, le haut de plage est alors très raide et non dissipatif. Quand les vagues se propagent en eaux peu profondes, les mouvements oscillatoires deviennent importants, les vagues réfractent sur une courte distance sans gonfler et déferlent de manière abrupte sur la barre subtidale (Fig. IV-11b). Les résultats numériques suggèrent que le déferlement est de type déversant (*"spilling"*). Ces larges variations dans les hauteurs de vagues entraînent la modification de la distribution des spectres d'énergie par transfert d'énérgie et interaction non-linéaire.

La dissipation de la houle due à la réfraction et au déferlement augmente l'énergie disponible pour le transport sédimentaire. La distribution de cette énergie dépendra de l'importance relative du marnage, de la hauteur des vagues et de la morphologie sous-marine. A marée haute l'énergie est donc distribuée plus largement à travers le marais et le transport sédimentaire sera dirigé essentiellement vers la côte (Fig. IV-12a). Au contraire, à marée basse l'énergie de la houle est hautement concentrée en haut de pente et le transport sédimentaire se fera plus vers le large (Fig. IV-12b). Une divergence dans le transport s'établit donc en fonction de ces conditions.

En utilisant la méthode de Li et Amos pour le calcul de la vitesse de cisaillement liée à la combinaison houle-courant, DYSCO montre que la houle est plus efficace pour remettre en suspension les sédiments à marée basse même si le transport à marée haute reste relativement important. Grant et Madsen (1979) et Glenn et Grant (1987) statuèrent que la couche limite de

cisaillement associée aux mouvements orbitaux est d'un ordre de grandeur supérieur à la couche limite de cisaillement associée à des courants uniformes d'une intensité comparable. Ce phénomène est dû à la formation d'une couche limite de fond oscillante, ce qui facilite la remise en suspension. Toutefois, Camenen et Larroudé (2003) concluent dans leur étude numérique que les modèles basés sur les méthodes de Grant et Madsen surestiment la vitesse de frottement dans une interaction houle-courant (voir également Hill *et al.* 2003 dans l'annexe A1).

La propagation des vagues à l'approche de la côte a été décrite par Longuet-Higgins et Stewart (1962). Celles-ci induisent de fortes forces de pression et d'inertie à la côte. Par conservation de la quantité de mouvement, il y a création des courants littoraux (*"longshore"*), des courants d'arrachements (*"Rip-current"*) et d'autres types de courants côtiers. La modélisation permet de dissocier l'impact de ces différents courants de l'impact des mouvements orbitaux de la houle. Par conséquent, les mécanismes forçants, considérés dans ce cas, sont différents de ceux considérés dans la méthode de Li et Amos pour la recombinaison des courants et des houles. Le schéma de circulation en présence de vagues est modifié à travers les tensions de radiation de Longuet-Higgins. Ainsi, lors des simulations de courants de marée en fin de flot (Fig. IV-8a) et en fin de jusant (Fig. IV-8b), des courants d'arrachements ont été identifiés. Ceux-ci sont clairement générés en fin de marée basse. Le frottement induit par les courants de flot uniquement a une très faible capacité à mettre en mouvement les sédiments du fond. Au contraire les courants modifiés par les tensions de radiations des vagues sont plus efficaces. Les vagues qui se propagent génèrent une plus forte force de pression à la côte en fin de marée haute qu'en fin de marée basse. Toutefois en fin de marée basse, il apparaît que les vagues de tempête restent la seule source d'énergie pour la

remise en suspension. Une fois en suspension, les sédiments seront transportés préférentiellement dans les zones de courants d'arrachements et donc vers le large.

Tous ces processus sont relativement identifiables. Toutefois lors de la mission Fraser 2002, certaines fortes variations observées sur les SSC_{OBS} et SSC_{ABS} filtrés (Fig. III-5) n'ont pas pu directement être reliées aux pics de tempête et aux mécanismes décrits précédemment. C'est notamment le cas pour l'événement de remise en suspension du 12 mars 2002. Différentes hypothèses peuvent expliquer cet événement. Une forte advection de sédiment allochtone depuis une zone plus turbulente peut entraîner l'apparition sur les données enregistrées de fortes concentrations de sédiments en suspension. De plus le tripode Norton se situe dans un champ de dunes qui complexifie très certainement le schéma de circulation (Kostachuk et Church 1993). Les vitesses de cisaillement combinées, calculées par le modèle DYSCO à partir des données de terrain, présentent un comportement similaire à l'évolution des SSC mesurés. Cela signifie que les mécanismes forçants générant la remise en suspension ont été mesurés. La propagation de vagues à la côte lors du flot peut générer assez de forces de pression pour créer une surcote. Lors de la marée descendante les forces de pressions liées à cette surcote peuvent générér des courants de "*downwelling*" (c'est à dire liés à une plongée d'eau). Ces courants de "*downwelling*" associés avec les composantes "*offshore*" des courants de jusant et les forces gravitationnelles peuvent être suffisantes pour permettre une forte remise en suspension. Les cellules d'arrachement identifiées lors des simulations participent très certainement à ce processus.

6. CONCLUSION ET PERSPECTIVES

Le fond sédimentaire de Roberts Bank à moins de 20 m de profondeur est caractérisé par des surfaces d'érosion affleurantes et de larges dunes isolées indiquant des conditions d'érosion et un déficit en sédiments (Carle et Hill soumis). Ce travail de thèse a mis en évidence les processus qui participent au façonnage de Roberts Bank, qui contribuent à son érosion, et à la mise en place de nouvelles structures sédimentaires.

1. Pendant la marée montante, le courant peut être suffisamment fort pour initier le mouvement des sédiments et créer des nuages de remise en suspension depuis le fond, parfois dans toute la colonne d'eau. En eau peu profonde, la composante "*onshore*" du courant de marée induit un transport à la côte, tandis qu'en eau plus profonde une faible composante "*offshore*" du courant peut favoriser un transport vers le large le long de la pente. Les chenaux, les dunes subaquatiques et les surfaces d'érosion affleurantes fournissent une rugosité de fond suffisante à la génération de turbulence et donc de nuages de sédiments en suspension.

2. Lors de la marée de jusant, un transport sédimentaire "*offshore*" a lieu à partir d'un panache de surface, généré par les sédiments remis en suspension en eau peu profonde puis transportés vers le large par les chenaux deltaïques. Le processus de "sédimentation convective induite par un mélange" ("*mixing-induced convective sedimentation*") est favorisé par une forte intensité de turbulence.

3. Les vagues qui se propagent sur la partie supérieure de la pente du Delta du Fraser sont essentiellement induites par le vent et ne présentent pas de composante de houle ou d'onde infragravitaire. Lorsque les vents s'orientent plein Ouest, les vagues formées présentent des périodes plus longues. Toutefois, les hauteurs significatives mesurées, présentées dans l'article 2 (chapitre 3), restent inférieures à 1 m.

4. Le comportement des vagues dans la région située après la rupture de pente deltaïque dépend du marnage, de l'incidence de la propagation et de la morphologie sous-marine. A marée haute, les vagues vont progressivement se réfracter au dessus d'un fond en légère pente. Par contre, à marée basse, la partie supérieure de la plage est alors abrupte et les vagues se réfractent sur une très courte distance. Aucun processus de "*shoaling*" n'est alors initié et le déferlement se produit sur la partie frontale ou au-dessus de la barre subtidale.

5. La divergence du transport sédimentaire au niveau de la rupture de pente deltaïque est contrôlée par la relation entre les vagues de tempête et le marnage. A marée haute, le transport sédimentaire est dominé par une composante "*onshore*". Au contraire, à marée basse le transport sédimentaire "*offshore*" est favorisé. Le transport sédimentaire net à travers la zone côtière est donc déterminé par l'importance relative de ces conditions.

6. Le transport sédimentaire, gouverné par cette relation entre les vagues de tempête et l'oscillation de marée, est toutefois complexifié par la présence d'une surélévation du niveau marin d'ordre dynamique, dit "*set-up*" de tempête. L'advection par la marée montante contribue également à ce "*set-up*". Lors de la marée descendante, les courants de "*downwelling*" engendrés par ce "*set-up*" ajoutées aux forces de frottement dues au courant de jusant induisent une remise en suspension des sédiments, et un transport "*offshore*". Ce

phénomène est également associé aux rip currents générés par la propagation de la houle à la côte.

Le travail présenté dans ce manuscrit a permis de mettre en évidence la variabilité du transport sédimentaire sur le front et la pente deltaïque de Roberts Bank. L'identification des mécanismes à l'échelle des processus et la compréhension de la dynamique sédimentaire à l'échelle de la zone confirment donc de manière globale que Roberts Bank est soumis à une érosion significative. Les processus sédimentaires tels que le remplissage d'anciens chenaux, ou encore la migration des dunes sédimentaires se font par le transport des sédiments mis à disposition par la remise en suspension sur le site. Cette approche qualitative doit cependant être étayée afin de quantifier ces processus.

En perspective de ce travail, le projet VENUS (Victoria Experimental Network Under the Sea) a pour objectif la mesure en temps réel de multiples paramètres océanographiques. En effet, l'utilisation de stations instrumentées est importante pour les suivis long terme, et la compréhension des phénomènes dont la fréquence d'apparition reste incertaine. Différents instruments, des éclairages, et des engins télé-opérés à câble (remotely operated vehicles) seront mis en place dans un réseau permanent de câbles sous-marins en fibres optiques. Une des lignes majeures de ce projet traversera le détroit de Géorgie près du terminal de Ferry de Tsawwassen. Les données seront recueillies en continu, et pourront être analysées en temps réel.

L'instrumentation embarquée, tel que pour les mesures de courants par profileurs de coque, permet de s'extraire des contraintes spatiales encore existantes dans le projet VENUS. Il serait donc important de continuer les mesures par profileurs acoustiques embarqués notamment au

niveau des chenaux de distribution et des chenaux sous-marins. Le traitement du signal rétrodiffusé a montré un fort potentiel dans l'estimation des concentrations de sédiments en suspension. L'utilisation d'appareillage acoustique multifréquence permettrait de s'affranchir des restrictions existantes dans l'utilisation de l'effet doppler d'une seule fréquence.

La modélisation est importante dans la compréhension des systèmes sédimentaires puisqu'elle permet une approche à la fois spatiale et temporelle. La calibration des modèles à partir des données expérimentables permettrait la quantification du transport sédimentaire et des flux d'érosion dans la zone de Roberts Bank.

Enfin ce travail s'est entièrement focalisé sur la zone entre le marais deltaïque et le prodelta où a été démontrée l'existence d'une divergence dans le transport sédimentaire. Il y a donc un mouvement des sédiments vers la plaine deltaïque. Pour comprendre le système sédimentaire dans son ensemble, il serait important de connaître l'origine et le devenir des sédiments en direction "*onshore*". Ce travail devra donc être couplé aux recherches déjà en cours sur le marais deltaïque.

BIBLIOGRAPHIE

Alvarez, L.G. and Jones, S.E. (2002). Factors influencing suspended sediment flux in the upper Gulf of California. Estuarine, Coastal and Shelf Science, v. 54, p. 754-759.

Arnott, R. W. C. and Southard, J. B. (1990). Exploratory flow-duct experiments on combined-flow bed configurations, and some implications for interpreting storm-event stratification. Journal of Sedimentary Petrology, v. 60(2), p.211-219.

Baba, J. and Komar, P. D. (1981). Measurements and analysis of settling velocities of natural quartz sand grains. Journal of Sedimentary Petrology, v. 51(2), p. 631-640.

Barrie, J.V. (2000). Recent geological evolution and human impact: Fraser Delta, Canada. In Coastal and Estuarine Environments: sedimentology, geomorphology and geoarcheology. Pye, K. and Allen, J.R.L. London, The Geological Society of London, v. 175, p. 281-292.

Barrie, J.V. and Currie, R.G. (2000). Human impact on the sedimentary regime of the Fraser River Delta, Canada. Journal of Coastal Research, v. 16, p. 747-755.

Battjes, J. A. (1974). Surf similarity. Proc 14th International Coastal Engineering Conference, p. 466-480.

Berkhoff, J. C. W. (1972). Computation of combined refraction-diffraction. Proc.13th Int. Conf. On Coastal Engineering, Vancouver, p. 471-490.

Berkhoff, J. C. W. (1976). Mathematical models for simple harmonic linear water waves; wave diffraction and refraction, Delft Hydraulics Laboratory. Publ. N°163, p. 1-103.

Birch, R., Hill, P. R., Clarke, M., Lemon, D. and Fissel, D. (2003). A configurable multi-sensor tripod for the study of near-bottom ocean processes. Oceans 2003, San Diego, p. 1234-1240.

Camenen, B. and Larroudé, P. (2000). Numerical comparaison of sediment transport formulae. Marine sandwave dynamics, Proceedings of an International Workshop, March 23-24 2000, University of Lille, France, p. 37-42.

Camenen, B. and Larroudé, P. (2003). Comparison of sediment transport formulae for the coastal environment. Coastal Engineering, v. 48, p. 111-132.

Carle, L. and Hill, P. R. (2004 submitted). Morphology of the Roberts Bank upper foreslope, Fraser River Delta, Britsih Columbia, Canada. Journal of Sedimentary Research.

Cassidy, J. F. and Rogers, G. C. (1999). Seismic site response in the greater Vancouver, British Columbia, area: spectral ratios frol moderate earthquakes. Canadian Geotechnical Journal, v. 36, p.195-209.

Christian, H.A., Mosher, D.C., Mulder, T., Barrie, J.V. and Courtney, R.C. (1997). Geomorphology and potential slope instability on the Fraser River delta foreslope, Vancouver, Britsih Columbia. Canadian Geotechnical Journal, v. 34, p. 432-446.

Clague, J. J. (1998). Geological setting of the Fraser River Delta. Geology and Natural Hazards of the Fraser River Delta, British Columbia. Clague, J. J., Luternauer, J. L. and Mosher, D. C., Geological Survey of Canada. Bulletin 525, p. 7-16.

Crean, P.B. (1976). Numerical model studies of the tides between Vancouver Island and the mainland. J. Fish Res. Bd. Canada, v. 33, p. 2340-2344.

Crean, P.B. (1978). A numerical model of barotropic mixed tides between Vancouver Island and the mainland and its relation to studies of the estuary's circulation. In Hydrodynamics of Estuaries and Fjords. Nihoul, C.J. New York, Elsevier, p. 283-314.

Currie, R.G. and Mosher, D.C. (1996). Swath bathymetric surveys in the strait of Georgia, British Columbia. In Current Research 1996, Geological Survey of Canada. E, p. 33-40.

Dibajnia, M. and Watanabe, A. (1998). Transport rate under irregular sheet flow conditions. Coastal Engineering, v. 35(3), p. 167-183.

DLR Software Ltd (1997). Sediview Procedure Manual. Issue 1 (SV v1.1), p. 1.1-7.16.

Evoy, R.W., Moslow, T.F. and Luternauer, J.L. (1997). Grain size distribution patterns supporting sediment bypassing on the Fraser River delta foreslope, British Columbia, Canada. Journal of Coastal Research, v. 13, p. 842-853.

Evoy, R.W., Moslow, T.F., Patterson, R.T. and Luternauer, J.L. (1993). Patterns and variability in sediment accumulation rates, Fraser River delta foreslopes, British Columbia, Canada. Geo-Marine Letters, v. 13, p. 212-218.

Fisher, F.H. and Simmons, V.P. (1977). Sound absorption in sea water. Journal of Acoustical Society of America, v. 62, p. 558-564.

Flagg, C.N. and Smith, S.L. (1989). On the use of the acoustic Doppler current profiler to measure zooplankton abundance. Deep-Sea Research, v. 36(3), p. 455-474.

Foreman, M.G.G., Walters, R.A., Henry, R.F., Keller, C.P. and Dolling, A.G. (1995). A tidal model for eastern Juan de Fuca Strait and the southern Strait of Georgia. Journal of Geophysical Research, v. 100(n°C1), p. 721-740.

Fredsøe, J. (1984). Turbulent boundary layers in wave-current motions. Journal of Hydraulic Engineering, v. 110, p. 1103-1120.

Garcia, M.H. and Admiraal, D.M. (1998). Laboratory measurements of suspended sediment concentration in unsteady flows with an acoustic backscatter profiler. Federal interagency workshop, sediment technology for the 21'st century, St. Petersburg, p. 1-2.

Glenn, S. M. and Grant, W. D. (1987). A suspended sediment stratification correction for combined wave and current flows. Journal of Geophysical Research, v. 92, p. 8244-8264.

Grant, W. D. and Madsen, O. S. (1979). Combined wave and current interaction with a rough bottom. Journal of geophysical research, v. 84, p. 1797-1808.

Grant, W. D. and Madsen, O. S. (1986). The continental-shelf bottom boundary layer. Annual Reviews of Fluid Mechanics, v. 18, p. 265-305.

Hart, B. S. and Barrie, J. V. (1997). Environmental Geology of the Fraser delta, Vancouver. Environmental Geology of Urban Area. Eyles, N., Geological Association of Canada, p. 285-296.

Hart, B.S. (1993). Large-scale in situ rotational failure on a low-angle delta slope: the foreslope hills, Fraser Delta, British Columbia, Canada. Geo-Marine Letters, v. 13, p. 219-226.

Hart, B.S., Hamilton, T.S. and Barrie, J.V. (1998). Sedimentation rates and patterns on a deep water delta (Fraser Delta, Canada): Integration of high-resolution seismic stratigraphy, core lithofacies, and 137Cs fallout stratigraphy. Journal of Sedimentary Research, v. 68(4), p. 556-568.

Hart, B.S., Hamilton, T.S., Prior, D.B. and Barrie, J.V. (1995). Seismostratigraphy and sedimentary framework of a deep water Holocene delta: Fraser River, British Columbia. In Geology of deltas. Oti, M.N. and Postma, G. Rotterdam, Balkema, A.A., p. 167-178.

Hart, B.S., Prior, D.B., Barrie, J.V., Currie, R.G. and Luternauer, J.L. (1992). A river mouth submarine channel and failure complex, Fraser Delta, Canada. Sedimentary Geology, v. 81, p. 73-87.

Hay, A.E. and Sheng, J. (1992). Vertical profiles of suspended sand concentration and size from multifrequency acoustic backscatter. Journal of Geophysical Research, v. 97 (C10), p. 15,661-15,677.

Hill, P. R. (2001). Conceptual model for sediment transport pathways on the Fraser delta foreslope. Geological Survey of Canada, Vancouver, p. 1-19.

Hill, P. R. and Davidson, S. (2002). Preliminary modeling of sediment transport on the upper foreslope of the Fraser River delta. Geological Survey of Canada, Current Research, v. 2002-E2, p. 1-9.

Hill, P. R., Meulé, S. and Longuépée, H. (2003). Combined flow processes and sedimentary structures on the shoreface of the wave dominated Grande Rivière de la Baleine Delta. Journal of Sedimentary Research, v. 73(2), p. 217-226.

Hoitink, A. J. F. (2004). Tidally-induced clouds of suspended sediment connected to shallow-water coral reefs. Marine Geology, v. 208(1), p. 13-31.

Horikawa, K. (1988). Nearshore dynamics and coastal processes: theory, measurement and pedictive models. Tokyo. University of Tokyo Press, p. 1-522.

Jonsson, I. G. (1966). Wave boundary layers and friction factors. Proceedings 10th Conference of Coastal Engineering, Tokyo, p. 127-148.

Kincaid, C., Pockalny, A. and Huzzey, L.M. (2003). Spatial and temporal variability in flow at the mouth of Narragansett Bay. Journal of Geophysical Research, v. 108(C7): 3218, doi:10.1029/2002JC001395.

Kirby, J. T. (1986). Higher approximations in the parabolic equation method for water waves. Journal of Geophysical Research, v. 91, p. 933-952.

Kostaschuk, R. A. and M. A. Church. 1993. Macroturbulence generated by dunes: Fraser River, Canada. Sedimentary Geology, v. 85, p. 25-37.

Kostaschuk, R., Luternauer, J. L. and Church, M. A. (1998). Sedimentary processes in the estuary. Geology, Geohazards of the Fraser River Delta, British Columbia. Clague, J. J., Luternauer, J. L. and Mosher, D. C., Geological Survey of Canada Bulletin, v. 525, p. 41-56.

Kostaschuk, R.A., Luternauer, J.L., Barrie, J.V., Werth Von Deichmann, L. and Leblond, P.H. (1995). Sediment transport by tidal currents and implications for slope stability: Fraser river delta, British Columbia. Canadian Journal of Earth Sciences, v. 32, p. 852-859.

Kostaschuk, R.A., Luternauer, J.L., McKenna, G.T. and Moslow, T.F. (1992). Sediment transport in a submarine channel system: Fraser River Delta, Canada. Journal of Sedimentary Petrology, v. 62, p. 273-282.

Lecouturier, M., Grochowski, N.T., Heathershaw, A., Oikonomou, E. and Collins, M.B. (2000). Turbulent and macro-turbulent structures developed in the benthic boundary layer, downstream of topographic features. Estuarine, Coastal and Shelf Science, v. 50(6), p. 817-833.

Lee, T.H. and Hanes, D.M. (1995). Direct inversion method to measure the concentration profile of suspended particles using backscattered sound. Journal of Geophysical Research, v. 100(C2), p. 2649-2658.

Li, M.Z. and Amos, C.L. (1995). SEDTRANS92: A sediment transport model for continental shelves. Computers and Geosciences, v. 21(4), p. 533-554.

Li, M. Z. and Amos, C. L. (1998). Predicting ripple geometry and bed roughness under combined waves and currents in a continental shelf environment. Continental Shelf Research, v. 18(9), p. 941-970.

Li, M. Z. and Amos, C. L. (1999a). Field observations of bedforms and sediment transport thresholds of fine sand under combined waves and currents. Marine Geology, v. 158(1-4), p. 147-160.

Li, M. Z. and Amos, C. L. (1999b). Sheet flow and large wave ripples under combined waves and currents: Field observations, model predictions and effects on boundary layer dynamics. Continental Shelf Research, v. 19(5), p. 637-663.

Li, M. Z. and Amos, C. L. (2001). SEDTRANS96: The upgraded and better calibrated sediment-transport model for continental-shelves. Computers and Geosciences, v. 27(6), p. 619-645.

Liebermann, L. (1951). The effect of temperature inhomogeneities in the ocean on the propagation of sound. Journal of Acoustical Society of America, v. 23, p. 563-570.

Longuet-Higgins, M. S. and Stewart, R. W. (1962). Radiation stress and mass transport in gravity waves, with application to 'surf beats'. Journal of Fluid Mechanics, v. 13, p. 481-504.

Longuet-Higgins, M. S. (1970). Longshore currents generated by obliquely incident sea waves. Journal of Geophysical Research, v. 75, p. 6778-6801.

Luternauer, J. L., Mosher, D. C., Clague, J. J. and Atkins, R. J. (1998). Sedimentary environments of the Fraser delta. Geology and Natural Hazards of the Fraser River Delta, British Columbia. Clague, J. J., Luternauer, J. L. and Mosher, D. C., Geological Survey of Canada Bulletin 525, p. 27-39.

Luternauer, J.L., Mosher, D.C., Clague, J.J. and Atkins, R.J. (1998). Sedimentary environments of the Fraser delta. In Geology and Natural Hazards of the Fraser River Delta, British Columbia. Clague, J.J., Luternauer, J.L. andMosher, D.C., Geological Survey of Canada Bulletin, v. 525, p. 27-39.

Luternauer, J. L. and Murray, J. W. (1973). Sedimentation on the western delta-front of the Fraser River, British Columbia. Canadian Journal of Earth Sciences, v. 10, p. 1642-1663.

Marcer, R. and Robin, N. (1996). Modélisation des courants de houle et du transport sédimentaire pour l'étude de stabilité de plage. $IV^{\text{ème}}$ journées nationales de Génie civil-Génie côtier, Ed. Parallia, p. 61-68.

Mathews, W.H. and Shepard, F.P. (1962). Sedimentation of Fraser river delta, British Columbia. Bulletin of the American Association of Petroleum Geologists, v. 46(8), p. 1416-1443.

Maxworthy, T. (1999). The dynamics of sedimenting surface gravity currents. Journal of Fluid Mechanics, v. 392, p. 27–44.

McCool, W. W. and Parsons, J. D. (2004). Sedimentation from buoyant fine-grained suspensions. Continental Shelf Research, v. 24, p. 1129-1142.

Meulé, S., Hill, P. S. and Pinazo, C. (2004a, submitted). Suspended sediment transport processes on the front of the tide-influenced Fraser River Delta, British Columbia, Canada. Journal of Sedimentary Research.

Meulé, S., Hill, P. S. and Pinazo, C. (2004b, submitted). Wave dynamics over Roberts Bank: Processes and Modeling. Current Research. Geological Survey of Canada Paper.

Meulé, S., Pinazo, C., Degiovanni, C., Barusseau, J. P. and Libes, M. (2001). Numerical study of sedimentary impact of a storm on a sand beach simulated by hydrodynamic and sedimentary models. Oceanologica Acta, v. 24(5), p. 1-8.

Migniot, C. (1981). Erosion and sedimentation in sea and river. Le moniteur, p. 1-103.

Miller, M. J. and Thorpe, A. J. (1981). Radiation conditions for the lateral boundaries of limited-area numerical models. Quarterly Journal of the Royal Meteorological Society, v. 107, p. 615-628.

Milliman, J.D. (1980). Sedimentation in the Fraser River and its estuary, southwestern British Columbia (Canada). Estuarine and Coastal Marine Science, v. 10, p. 609-633.

Mordane, S., Mangoub, G., Maroihi, K. L. and Chagdali, M. (2004). A parabolic equation based on a rational quadratic approximation for surface gravity wave propagation. Coastal Engineering, v. 50(3), p. 85-95.

Mosher, D. C., Cassidy, J. F., Lowe, C., Mi, Y., Hyndman, R. D., Rogers, G. C. and Fisher, M. (2000). Neotectonics in the Strait of Georgia: first tentative correlation of seismicity in southwestern British Columbia. Geological Survey of Canada, Current Research 2000-A22, p. 1-9.

Myrow, P. M. and Southard, J. B. (1996). Tempestite deposition. Journal of Sedimentary Research, v. 66(5), p. 875-887.

Nielsen, P. (1992). Coastal bottom boundary layers and sediment transport. Singapore, Advanced series on ocean engineering, 4. World Scientific Publishing Co.Pte.Ltd., p. 1-324.

Penland, S., Boyd, R. and Suter, J. R. (1988). Transgressive depositional systems of the Mississipi delta plain: a model for barrier shoreline and shelf sand development. Journal of Sedimentary Petrology, v. 58(6), p. 932-949.

Petrie G., T. J. M. K. (1990). Terrain modelling in surveying and civil engineering. Whittles Publishing, p. 1-351.

Radder, A. C. (1979). On the parabolic equation method for water wave propagating method. Journal of Fluid Mechanics, v. 95, p. 159-176.

Rogers, G. C., Ed. (1994). Earthquakes in the Vancouver Area. Geology and Geological Hazards of the Vancouver Region, Southwestern British Columbia, Geological Survey of Canada, Bulletin 481, p. 221-229.

Rose, P.C. and Thorne, P.D. (2001). Measurements of suspended sediment transport parameters in a tidal estuary. Continental Sheld Research, v. 21, p. 1551-1575.

Sommerfeld, A. (1949). Partial differential equations, Lectures in Theoretical Physics, Academic Press, v. 6, p. 1-355.

Soulsby, R. L. (1997). Dynamics of marine sands. Thomas Telford Publications, p. 1-249.

Stive, M. J. F. (1984). Energy dissipation in waves breaking on gentle slopes. Coastal Engineering, v. 8, p. 99-127.

Sumer, B.M. and Deigaard, R. (1981). Particle motions near the bottom in turbulent flows in an open channel, Part 2. Journal of Fluid Mechanics, v. 109, p. 311–337.

Swift, D. J. P. and Thorne, J. A. (1991). Sedimentation on continental margins, I: a general model for shelf sedimentation. Shelf Sand and Sandstone Bodies, Geometry, Facies and Sequence Stratigraphy., Special Publication of International Association of Sedimentologists, v. 14, p. 3-31.

Tetzlaff, D.M. and Harbaugh, J.W. (1989). Simulating clastic sedimentation. New York, Van Nostrand Reinhold, p. 1-202.

Thomson (1981). The Oceanography of the British Columbia coast. Canadian Special Publication of Fisheries and Aquatic Sciences. Department of Fisheries. Ottawa. Bulletin 56, p. 1-291.

Thomson, R.E. (1975). Longshore current generation by internal waves in the Strait of Georgia. Canadian Journal of Earth Sciences, v. 12, p. 472-488.

Thosteson, E.D. and Hanes, D.M. (1998). A simplified method for determining sediment size and concentration from multiple frequency acoustic backscatter measurements. Journal of Acoustical Society of America, v. 104(2), p. 820-830.

Valle-Levinson, A., Li, C., Royer, T. and Atkinson, L.P. (1998). Flow patterns at the Chesapeake entrance. Continental Shelf Research, v. 18, p. 1157-1177.

Van Rijn, L. C. (1984). Sediment transport, Part I: bed-load transport. Journal of Hydraulic Engineering, v. 110(10), p. 1431-1456.

Van Rijn, L. C. (1993). Principles of Sediment Transport in Rivers, Estuaries and Coastal Seas. Aqua Publications, p. 1-715.

White, K. and El Asmar, H. M. (1999). Monitoring changing position of coastlines using Thematic Mapper imagery, an example from the Nile Delta. Geomorphology, v. 29(1-2), p. 93-105.

Wright, L. D., Boon, J. D., Kim, S. C. and List, J. H. (1991). Modes of cross-shore sediment transport on the shoreface of the Middle Atlantic Bight. Marine Geology, v. 96, p. 19-51.

Yalin, M.S. (1972). Mechanics of Sediment Transport. Oxford, Pergamon, p. 1-290.

LISTE DES FIGURES

152

153

154

ANNEXE

A1. HILL P., **MEULÉ S.,** LONGUÉPÉE H. (2003). Combined flow processes and sedimentary structures on the shoreface of the wave dominated Grande Rivière de la Baleine Delta. Journal of Sedimentary Research, v. 73(2), p. 217-226.

A2. MEULÉ S., PINAZO C., DEGIOVANNI C., BARUSSEAU J.P., LIBES M. (2001). Numerical study of sedimentary impact of a storm on a sand beach simulated by hydrodynamic and sedimentary models, Oceanologica Acta, v. 24(5), p.417-424.

A3. CERTAIN R., **MEULÉ S.,** REY V., PINAZO C. (submitted to Journal of Marine Systems). Wave deformation over sand barred beach: Sète.

A4. MEULÉ S., CERTAIN R., PINAZO C., REY, V., (2003). Morphodynamique de la plage de Sète sous l'incidence de houle de tempête : expérimentation et modélisation. Communication au $9^{ème}$ congrès de l'Association des Sédimentologistes Français, Bordeaux, le 14-15-16 octobre 2003.

Le manuscrit présenté ici et des données complémentaires ont été mises à disposition sur le site internet suivant: http://samuel.meule.free.fr/. Les articles précedents sont présents en version pdf. Des animations de profils de signaux rétrodifusés sont téléchargeables et permettent une meilleure visualisation des phénomènes décrits dans le 1er article (chapitre 2). Les codes pour le modèle DYSCO et les calculs des conditions limites pour le modèle de COURAN sont également téléchargeables.

ANNEXE A1

COMBINED-FLOW PROCESSES AND SEDIMENTARY STRUCTURES ON THE SHOREFACE OF THE WAVE-DOMINATED GRANDE-RIVIÈRE-DE-LA-BALEINE DELTA

PHILIP R. HILL,* SAMUEL MEULÉ, AND HUGUES LONGUÉPÉE**

Institut des Sciences de la Mer, Université du Quebec à Rimouski, 310 allée des Ursulines, Rimouski, QC, G5L 3A1, Canada

e-mail: phill@nrcan.gc.ca

ABSTRACT: Shoreface sediments exposed in raised deltaic deposits along the Hudson Bay coast are characterized by a thick succession of predominantly parallel-laminated and small-scale cross-laminated fine sand. Ripple forms, where preserved, include both combined-flow and wave-ripple geometries. Hummocky cross stratification is present in lower parts of the section. Similar facies have been found in cores from the present-day shoreface. Measurements of waves, currents, and suspended sediment concentrations in 10 m water depth, conducted over a 15-day period in the fall of 1999, captured four different meteorological periods. These included an intense four-day storm which sustained significant wave heights over 3 m for 15 hours and a storm surge of over 1 m height. Fair-weather conditions produce weak alongshore tidal flows, but oscillatory motions generated by small local waves predominate. During storms, orbital motions dominate the flow but a strong inertial flow generated by wind forcing is also present. Comparison with a published combined-flow bedform-stability diagram suggests that the predominant bedforms at 10 m depth would be small 2-D wave-dominated ripples and small, weakly asymmetrical 3-D ripples under fair-weather conditions and large 3-D ripples and upper plane bed under storm wave conditions. The predominantly interbedded parallel-laminated and small-scale cross-laminated facies is therefore interpreted to be characteristic of the upper shoreface, where the seabed experiences intense oscillatory motions under all storms and even some fair-weather conditions. Combined-flow ripples would form during storm events because of the stronger wind-driven mean residual current. Hummocky cross-stratification forms in deeper water during storms where the ratio of maximum orbital velocity to mean residual current velocity remains for longer periods in the large 3-D ripple field during the waning phase of storms. A numerical bed predictor model, using the 15-day data set as input, also suggests bimodal conditions fluctuating between wave ripples and upper plane bed at 10 m water depth. This model further indicates that combined-flow ripples would form rarely, but tends to underestimate the threshold of sediment suspension.

INTRODUCTION

The shoreface is variously defined in the geological literature, but most commonly as the zone between mean low water level and fair-weather wave base (Reading and Collinson 1996). In practice, fair-weather wave base is interpreted in ancient successions by the transition from interbedded sandstones and mudstones to relatively clean sandstones (Walker and Plint 1992). The concept of fair-weather wave base is problematic on modern coasts, especially in restricted seaways where swell waves are insignificant and fair-weather conditions can include the near absence of waves. For the purposes of this paper, the shoreface is defined as the transition zone between the surf zone and the inner continental shelf in which shoaling but nonbreaking waves frequently cause sediment resuspension (Wright et al.

1991). This definition therefore includes the offshore transition zone between fair-weather and storm wave base (Reading and Collinson 1996).

The shoreface is the site of complex interaction between fluid processes and substrate response. Combined flows, consisting of oscillatory and steady flow components, are typical of the shoreface environment and are thought to produce diagnostic facies for their identification in ancient rocks (Walker and Plint 1992). These physical characteristics are also typical of wave-dominated deltas, where the delta-front succession resembles that of a wave-dominated shoreface (Bhattacharya and Walker 1992). In this paper, which describes a wave-dominated delta, the term shoreface is used to describe the portion of the delta front and prodelta on which shoaling but nonbreaking waves act.

The incident wave spectrum on a shoreface is highly variable and depends both on temporal changes in the wave conditions at a given site (storm versus fair-weather conditions) and on the geographic variability of the shoreface setting (e.g., open ocean dominated by long-period swell waves versus restricted basin dominated by short-period local waves). In addition, wind, tide and gravity forces influence the steady component of flow and contribute to both consistently strong alongshore flows and more intermittent cross-shore flows (Arnott and Southard 1990; Niedoroda and Swift 1981; Wright et al. 1991). This range of combined flows occurring in the shoreface environment leads to a complex range of possible preserved facies (Myrow and Southard 1991).

Substantial progress on the bedforms and sedimentary structures produced by combined flows has been made from laboratory studies (Harms 1969; Southard et al. 1990; Arnott and Southard 1990; Yokokawa 1995) and field measurements (Li et al. 1996; Li and Amos 1998, 1999). There is still, however, a need for more data to extend the range of observations available for interpreting combined-flow structures and shoreface facies. Isostatically uplifting shorelines such as that of Hudson Bay, northern Canada (Fig. 1), provide a particular opportunity to study the processes of shoreface sediment transport and facies evolution because process studies can be combined with examination of cores from the modern shoreface and sections through very recently raised shoreface deposits. The latter provide greater confidence that the facies interpreted to be due to particular physical conditions or processes are geologically preserved and significant.

Such conditions exist in the modern and raised delta of the Grande-rivière-de-la-Baleine delta (Hudson Bay, northern Quebec, Canada). Studies of sediment cores from offshore and sections of 3000-yr-old raised delta deposits exposed along the incised river valley have shown that the shoreface deposits of this wave-dominated delta consist of a predominant parallel-laminated and small-scale cross-laminated fine sand facies and that hummocky cross-stratification (HCS) has only limited occurrence. Standard facies models of wave- and storm-dominated shorefaces emphasize the presence of HCS and swaly cross-stratification. The objectives of this study were to examine the sediment transport conditions on the shoreface under fair-weather and storm conditions and to estimate the conditions under which these facies occur.

BACKGROUND

The Grande-rivière-de-la-Baleine (or Great Whale River) delta is located along the east coast of Hudson Bay (Fig. 1). The wave-dominated delta is one of a series of downstepping deltas formed along the incised valley of the Grande-rivière-de-la-Baleine as a result of isostatic rebound and falling relative sea level, following retreat of the Laurentide Ice sheet (Hill et al.
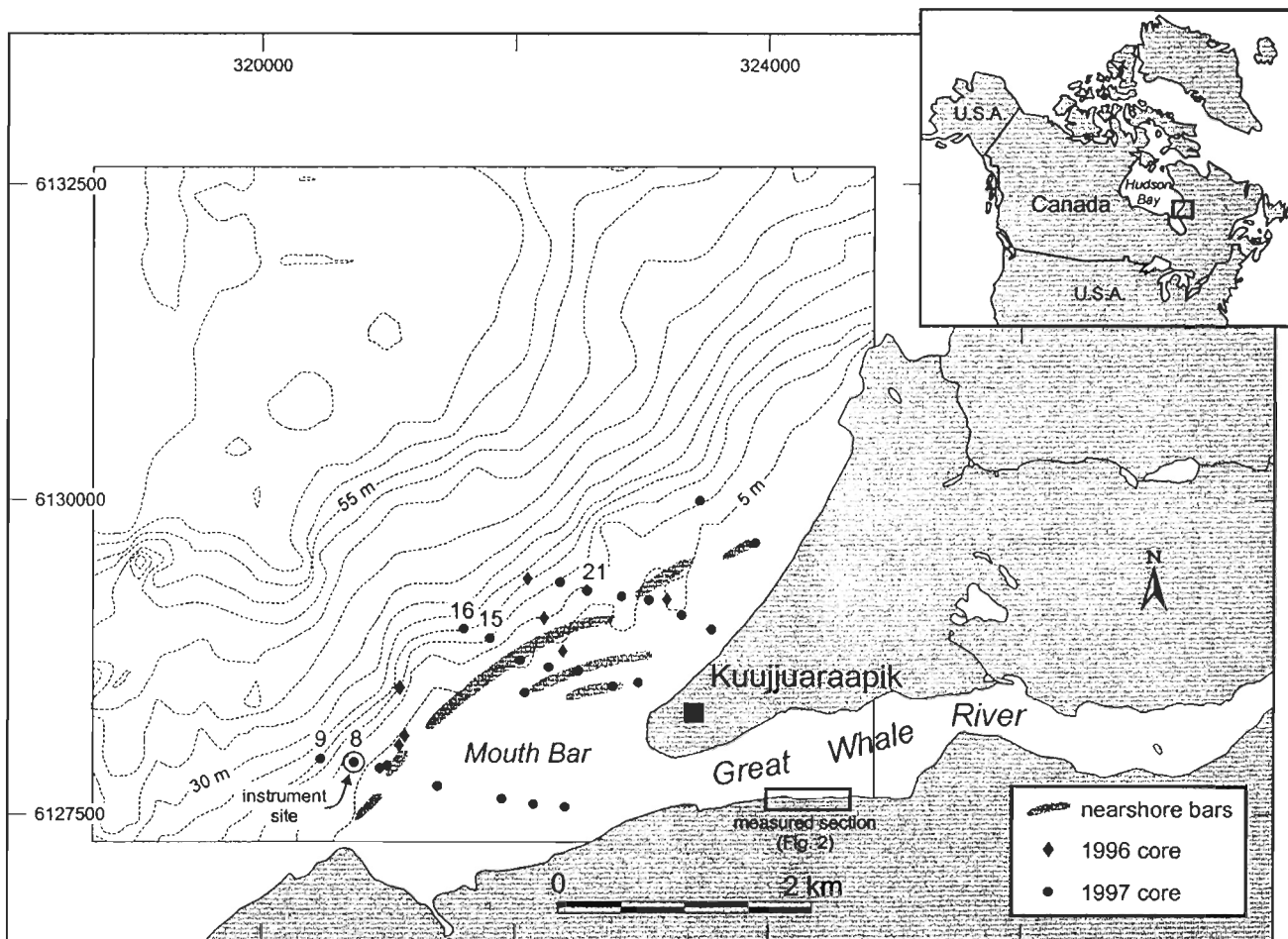
FIG. 1.—Location map showing the study area, raised section, core sites and instrument deployment site, Grande-rivière-de-la-Baleine, Hudson Bay. The numbered cores are shown in Figure 6.

1998; Gonthier et al. 1993). The present rate of isostatic uplift is 11 mm a⁻¹ (Hillaire-Marcel 1976; Allard and Tremblay 1983) and results in rapid incision of the river valley through the deltaic deposits, leaving exposures of the latter in the valley walls (Fig. 1).

The modern subaerial delta plain is characterized by a seaward-dipping surface, sloping at 1° from 25 m elevation to sea level (Fig. 1; Ruz and Allard 1994). The river flows into the sea on the southwest side of the delta across a nearshore platform, 1 km wide. The river channel shoals across a shallow (< 2 m) mouth bar (Fig. 1; Longuépée 2000). Offshore of the mouth bar, a single offshore bar, 2.5 m high, with its crest having a minimum water depth of 3.5 m, extends along the outer edge of the subaqeous delta platform, subparallel to the beach, converging slightly at the distal (northeastern) end.

The slope break occurs between 5 and 10 m water depth, and the prodelta slope extends to approximately 40 m water depth, where it merges with the basin floor (Fig. 1). The slope is steepest (3.9°) immediately seaward of the river mouth and becomes gentler (2.0°) alongslope to the northeast. The slope surface is generally smooth, and no evidence for submarine sliding, gullying, or other gravity processes has been found in either sidescan or chirp sonar data (Roberge 1998; Longuépée 2000).

METHODS

Facies information was derived from measured sections in the raised delta deposits exposed on the south wall of the incised Grande-rivière-de-

la-Baleine valley and from short push-cores obtained from the shoreface of the active delta (Fig. 1; Longuépée 2000). The exposed sections are less than 3000 years old, as calculated from their present elevation and known rates of isostatic uplift (Hillaire-Marcel 1976; Allard and Tremblay 1983).

Measurements of waves, currents, and suspended sediment concentrations were made over a 15-day period between 22 September and 6 October 1999 in 10 m water depth, seaward of the channel mouth (Fig. 1). The grain size of sediment in cores from the vicinity of this site ranges from fine (0.18 mm) to very fine (0.09 mm) sand. Waves and currents were measured in three-hourly nine-minute bursts at 2 Hz frequency (giving 1080 measurements per burst) using an InterOcean S4 current meter positioned at 1.0 m above the seabed. Two optical backscatter sensors (OBS), positioned at 30 cm and 100 cm above the seabed, were used to measure suspended-sediment concentration every minute. These data were calibrated for concentration values using a bottom sediment sample from the same water depth. Hourly wind speed and direction were obtained from the Canadian Atmospheric Environment Service, from their weather station at the Kuujjuarapik airport, located on the Grande-rivière-de-la-Baleine delta.

The current-meter data were analyzed to separate the oscillatory and steady components of flow. For each burst, the pressure and instantaneous current measurements were used to compute surface wave parameters (significant wave height, H_s; period, T; and direction) using spectral analysis and maximum near-bed orbital velocities, u_o, using linear wave theory. The
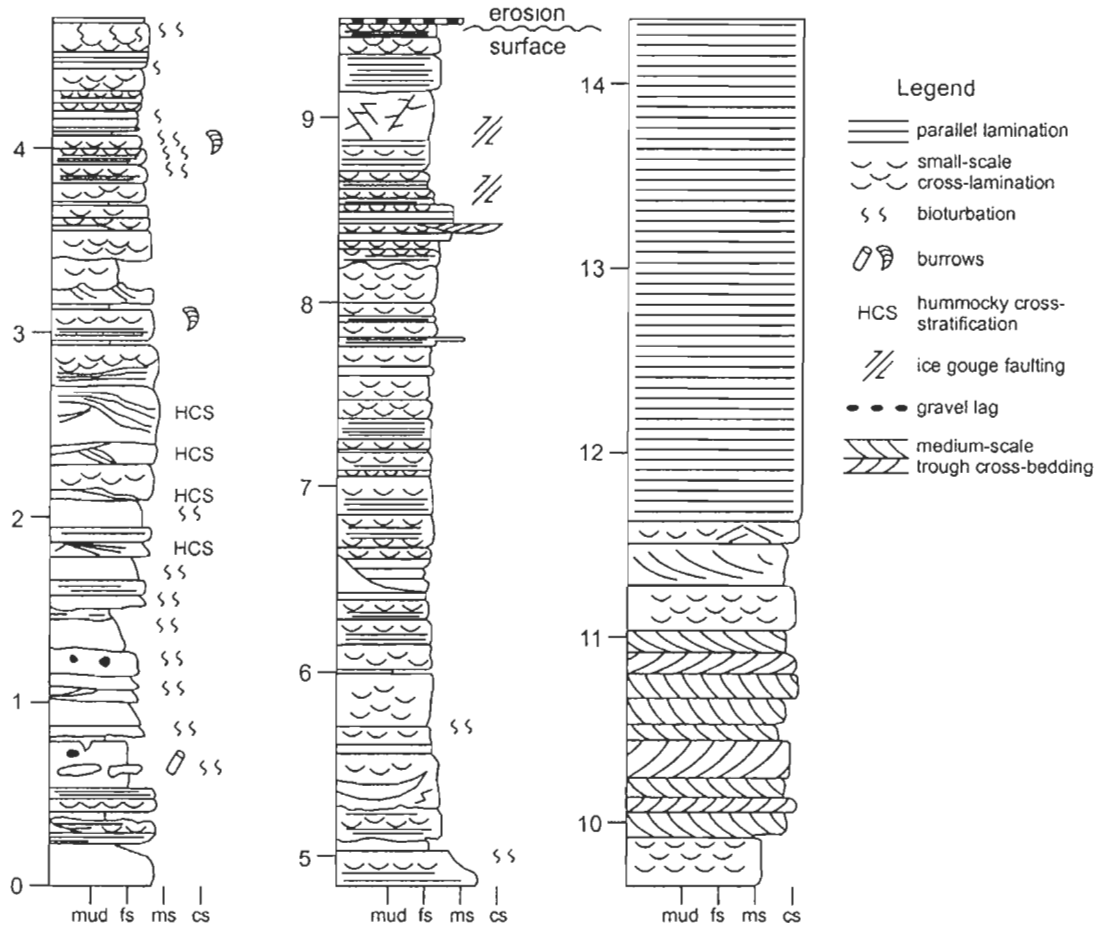
FIG. 2.—Section through deltaic deposits in the incised valley of the Grande-rivière-de-la-Baleine. For location, see Figure 1. Scale in meters above arbitrary datum.

steady current was obtained by filtering out the high-frequency velocity fluctuations (which are assumed to be produced by wave orbital motions) and then averaging the velocity and direction of the residual current over the burst. The coordinate system was corrected for magnetic north, and rotated to obtain a shore-normal x axis with u defined as positive shoreward and a shore-parallel y axis with v defined as positive northward along the shore.

For each burst, the mean water level was obtained from the S4 pressure sensor and compared to the predicted tides. An estimate of the storm-surge setup was thus obtained by comparing the tide prediction and the water level recorded by the pressure sensor.

The recorded data were compared to existing combined-flow bed state and bedform predictors. The first was the stratification-generating diagram of Myrow and Southard (1991), which is based largely on the results of flume tank experiments by Southard et al. (1990) and Arnott and Southard (1990) on 0.09 mm sand. The second predictor was that of Li and Amos (1995, 1998, 1999). This method uses the combined wave and current boundary-layer theory of Grant and Madsen (1979, 1986) to determine the combined-flow skin-friction shear velocity, $u_{*_{cws}}$, which takes into account grain roughness only. Li and Amos (1998, 1999) factor in the feedback of bedform development and bedload transport on the shear velocity by calculating a ripple-enhanced shear velocity over preexisting ripples prior to initiation of movement and the bedload shear velocity for conditions when bedload transport is underway. In this study, the calculations were carried out in a spreadsheet program. The calculations require input of the bedform

dimensions. Using empirical observations from 39 m depth on the Scotian Shelf, Li and Amos (1998) refined a bed-state predictor for medium sand using the ratio of the wave shear velocity, $u_{*_{ws}}$, to the steady-current shear velocity, $u_{*_{cs}}$. These findings were then extended to fine (0.2 mm) sand by Li and Amos (1999) using further empirical observations.

SHOREFACE FACIES

Sections through the deltaic deposits exposed in the incised valley consist of two successions, typically 9–10 m thick, separated by an erosion surface (Fig. 2). Both successions are characterized by seaward-dipping strata. The lower succession, interpreted to be shoreface deposits, coarsens upwards from bioturbated very fine sand and mud to interbedded parallel-laminated and small-scale cross-laminated fine sand (Fig. 3). Bioturbation predominates in the lowest 2 m of the section and persists as minor disruption of the bedding to 5.7 m. Mud interbeds are present to 3 m, and mud flasers are present through most of the lower succession, decreasing in thickness and abundance upwards. The interval between 2 and 3 m contains six beds, 5 to 30 cm thick, with isotropic hummocky cross-stratification (Fig. 4). The HCS beds have erosional bases. Internal truncation surfaces pass laterally into small-scale cross-lamination and both are in places draped with mud flasers.

The interbedded parallel-laminated and small-scale cross-laminated facies predominates from 3 m to the upper bounding surface of the lower succession, where they form an amalgamated sand unit with only very

FIG. 3.—Typical upper prodelta facies consisting of interbedded planar-laminated and ripple-laminated fine sand. Note erosional boundaries between intervals of planar-laminated and ripple-laminated sand. Scale bar is 10 cm long.
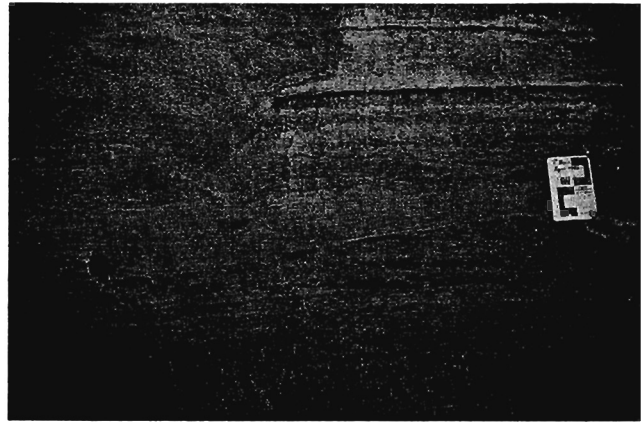

FIG. 4.—Hummocky cross-stratified bed. For scale, the notebook is 18.5 cm long.

minor mud flasers (Fig. 2). The small-scale cross-laminated beds are generally thicker, ranging from 5 to 20 cm thick, with parallel lamination being limited to thin basal units, 1–5 cm thick. The parallel-laminated intervals become thicker upwards, reaching a maximum of 20 cm. Towards the top of the lower shoreface succession, parallel-laminated and small-scale cross-laminated sets pass upwards from one to the other, with only minor and laterally discontinuous erosion surfaces marking the transition. These transitions are interpreted to represent bedform transitions within an apparent depositional continuum rather than discrete event beds as observed lower in the succession.

Ripple forms, where preserved at the tops of small-scale cross-laminated sets, are commonly near symmetric, with slightly rounded crests and bidirectional cross-lamination or unidirectional cross-lamination dipping towards the offshore (Fig. 5). Within the sets of the small-scale cross-laminated fine sand facies, both rounded-crest and symmetrical, concave-upward ripple forms are present. In the latter, the cross-lamination dips in both onshore and offshore directions. Unidirectional-dipping cross-lamination and rounded crests are characteristic of combined-flow ripples (Harms 1969; Yokokawa 1995). The small-scale cross-lamination described here is tentatively interpreted to be formed by wave ripples and wave-dominated combined flow ripples.

The lower succession is truncated by an erosion surface characterized by a gravelly lag deposit and local channels, 1–2 m deep (Fig. 2). This surface is interpreted to be a wave erosion surface, formed in shallow water as the emerging delta passed through the surf zone (Longuépée 2000). The upper succession is coarser-grained, consisting of medium-scale trough cross-bedded, medium to coarse sand, overlain by predominantly parallel-laminated coarse sand. These facies are respectively interpreted as bar and beach deposits (Hill et al. 1998).

On the basis of this interpretation and by analogy with the modern environment, the lower succession was deposited in water depths greater than 5 m on the prodelta slope, which here forms the lower shoreface. Cores taken from the modern shoreface confirm this interpretation (Fig. 6). In approximately 9 m water depth, at the location of the wave and current measurements (core 97-8) and at laterally equivalent stations (97-15, 97-21), the cores are dominated by a similar succession of interbedded parallel-laminated and small-scale cross-laminated fine sand, although some massive and bioturbated beds are also present. Cores from 20 m depth (97-9, 97-16) contain intervals of splaying lamination, resembling HCS or quasi-planar lamination (Arnott and Southard 1990; Arnott 1993).

OCEANOGRAPHIC OBSERVATIONS

General

The two weeks of measurements included two extended periods of fair-weather conditions and three periods of more energetic conditions including one major storm (Fig. 7). The equipment was deployed after two days of stormy weather and recovered on Day 14 during the build up to another significant storm. The time series of mean water depth shows the semidiurnal tidal oscillation with a maximum range of 1.7 m (Fig. 7C). Superimposed on this is a low-frequency signal related to wind direction. The mean water level was raised significantly from day 9 through 12 in response to strong winds blowing from the NW and WNW. This raised water level was a coastal setup, possibly reinforced by the opposition of river outflow to surface waves.

Fair-Weather Conditions (Days 1–5, 7–8)

Periods of light winds occurred for the first three days of the deployment, building to moderate winds from the SSE on Days 4 and 5 (Figs. 7A, B). These conditions generated only local waves with significant heights less than 1 m (Fig. 7D). Under these conditions, the weak (less than 10 cm s^{-1}) mean residual current flowed predominantly alongshore (Fig. 7E, F) but experienced both clockwise and anticlockwise rotation on the semidiurnal tide. Despite the low wave conditions, near-bed oscillatory motions were
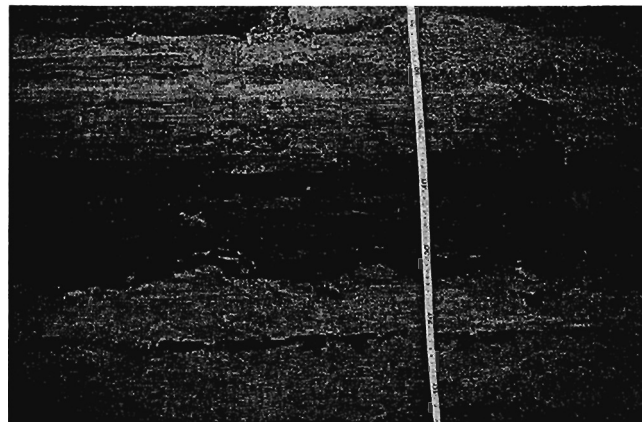

FIG. 5.—Well-preserved combined-flow ripples at the top of a small-scale cross-laminated fine sand interval. For scale, the tape measure is graduated in centimeters.
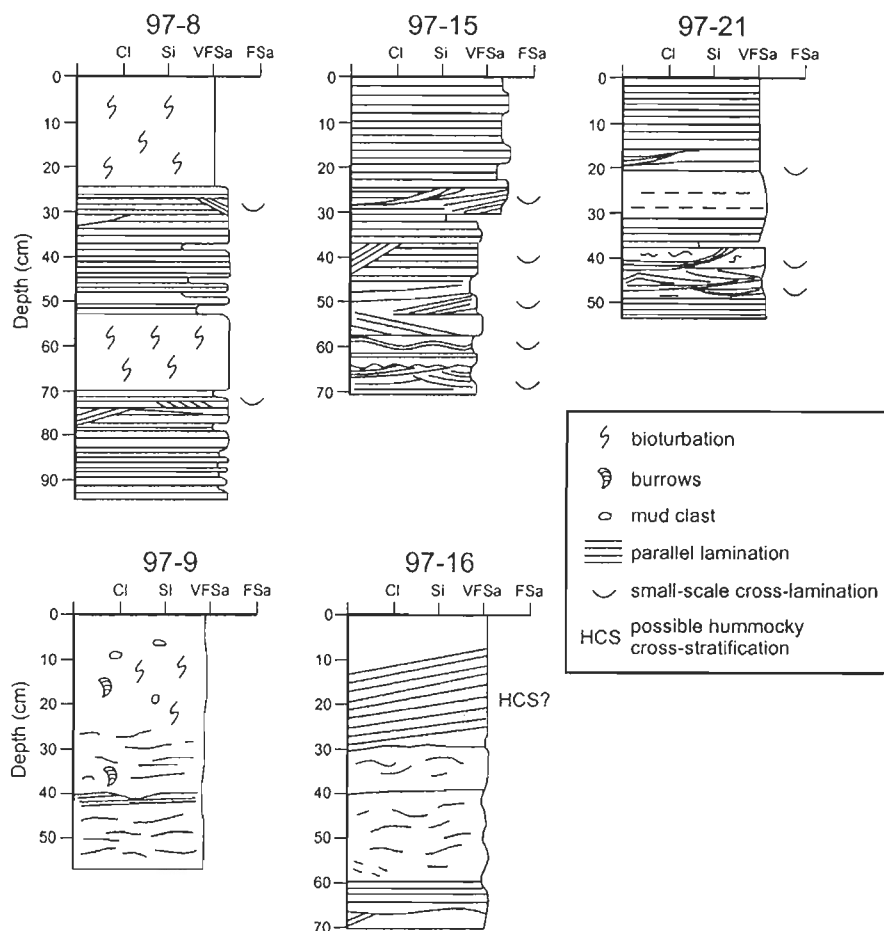
FIG. 6.—Sedimentary structures observed in shallow cores from the prodelta: Cores 8, 15, and 21 were taken in approximately 9 m water depth, Cores 9 and 16 in 20 m water depth. Location of cores is shown in Figure 1.

generally greater than the mean residual current (Fig. 7G). These conditions illustrate the weak nature of the tidal circulation in this microtidal setting. The OBS measurements show little or no sediment in suspension except for minor resuspension events at the 30 cm level, corresponding to slightly higher wave conditions. Similar conditions occurred during Days 7 and 8.

Moderate Storm Conditions (Days 5–6, 11–12)

Wind speeds built through Day 4 and were sustained at over 30 km h^{-1} through Days 5 and 6 (Fig. 7A). Wave heights did not increase until the wind direction switched from the SE to the NW in the middle of Day 6 (Fig. 7B, D). The southeasterly winds of Day 5 were associated with a southwesterly, alongshore mean residual current of 20 cm s^{-1} (Fig. 7E). When the wind turned to northwesterly, the current switched to the northeast with a maximum of 20 cm s^{-1}. This fluctuation was associated with low mean water levels during the periods of southeasterly winds and a rise during the northwesterly winds. With the northwesterly winds, relatively long-period waves ($T = 5.5$–6 s) were generated, reaching a maximum significant height of 1.5 m (Fig. 7D) and giving mean orbital velocities up to 57 cm s^{-1} (Fig. 7G). Significant near-bed suspension of bottom sediment occurred at the peak of the wave conditions (Fig. 7H). The OBS at 30 cm registered concentrations of 0.35 g l^{-1}.

Major Storm Conditions (Days 9 and 10)

Days 9 and 10 were characterized by an intense storm with the wind speeds in excess of 50 km h^{-1} (Fig. 7A). As the winds rose late on Day

8 through Day 9, they turned from the northeast to the northwest over a 24 h period. Significant wave heights exceeded 3 m for 15 consecutive hours (Fig. 7D). The significant wave periods were typically 6–7 s. Orbital velocities as high as 140 cm s^{-1} dominated the near-bottom flows despite the strong mean residual current up to 40 cm s^{-1} (Fig. 7G). Fluctuations in the mean residual current during the storm were out of phase with the tide. During the early part of the storm, late on Day 8 and through most of Day 9, the mean residual current rotated in a clockwise sense, with the net flow to the south and onshore (Fig. 7E, F). After the peak of the storm, the mean residual current switched abruptly to an anticlockwise rotation with the net flow to the north and offshore. This change in rotation correlates with establishment of a 1 m setup of the mean water level (Fig. 7C) that followed the shift in wind direction from northeast to northwest. The anticlockwise rotation lasted just under 24 hours before resuming clockwise rotation.

The strong combined-flow conditions generated throughout the storm caused major suspension of sediment (Fig. 7H). The OBS sensor at 30 cm elevation recorded values that suggest concentrations over 1 g l^{-1}, while suspended concentrations up to 0.2 g l^{-1} were recorded at 1 m above the seabed.

COMPARISON WITH COMBINED-FLOW MODELS

Based on laboratory data (Harms et al. 1982; Arnott and Southard 1990; Southard et al. 1990), the Myrow and Southard (1991) model consists of a bed configuration stability diagram with axes of maximum orbital veloc-
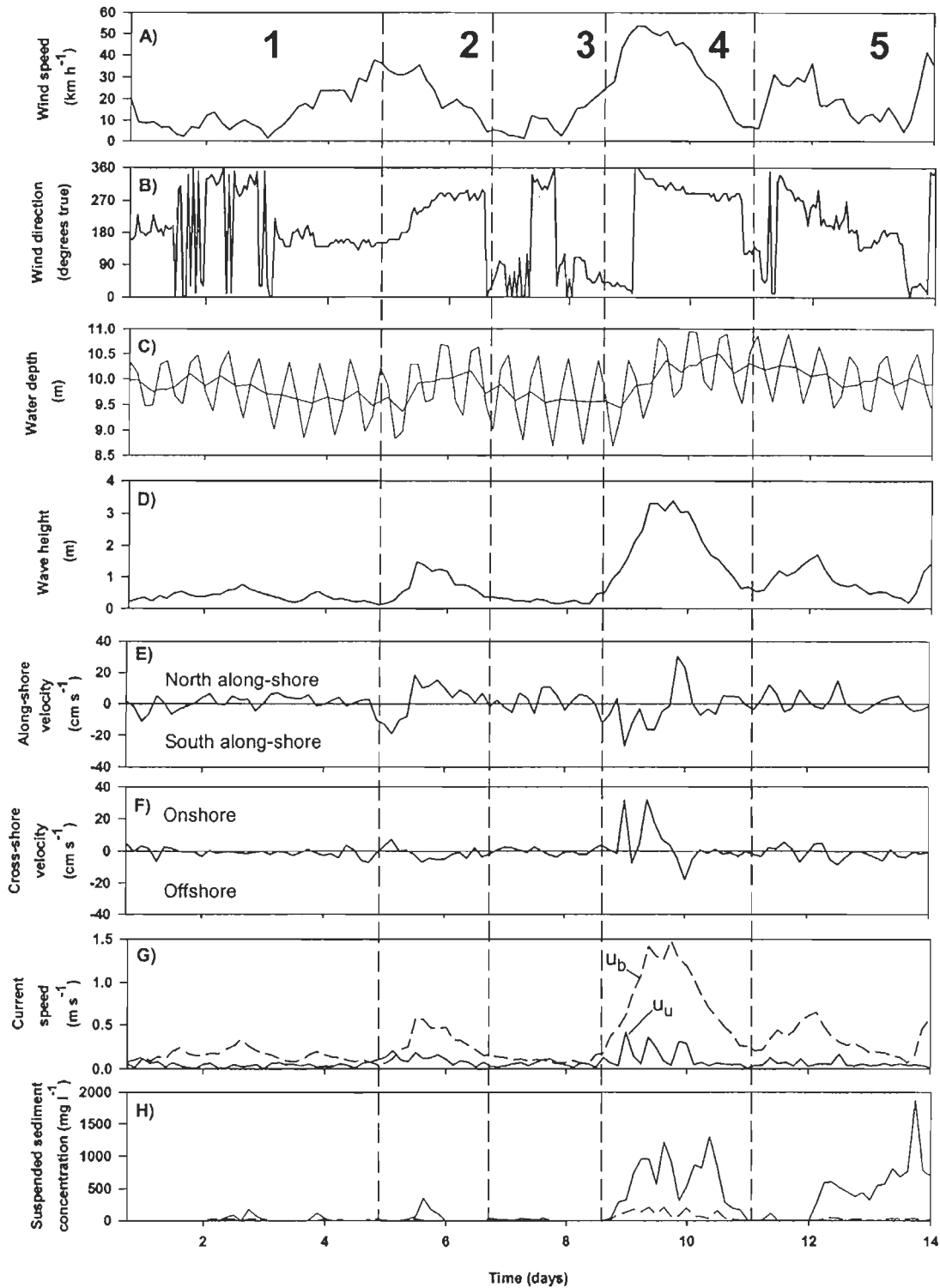
FIG. 7.—Time series of A) wind speed; B) wind direction; C) mean water depth; D) significant wave height; E) mean alongshore current velocity; F) mean onshore-offshore current velocity; G) mean oscillatory (u_o) and steady (u_u) components of the current speed; and H) suspended sediment concentrations. Wind data were obtained from the Canadian Atmospheric Environment Service weather station at Kuujjuarapik airport. The measurement period is divided into five intervals representing fair-weather (1, 3), moderate storm (2, 5), and major storm (4) conditions.

ity (u_o) and unidirectional flow velocity (u_u). The diagram is appropriate for fine to very fine sand and identifies stability fields for small and large 2-D and 3-D ripples as well as plane bed conditions. Myrow and Southard (1991) indicate that the curve representing the transition to upper-plane-bed conditions is generalized and extrapolated beyond the laboratory limits.

The data for fair-weather, moderate-storm and major-storm conditions at Grande-rivière-de-la-Baleine are plotted on this diagram in Figure 8. The calculated oscillatory current is used for u_o and the residual current at 1 m above the bed, averaged over single 9-minute bursts, is used for u_u. Under field conditions, the "unidirectional" current is far from unidirectional and the term "mean residual current" is used to describe u_u. During the fair-weather conditions of Days 2 and 3, the mean residual current was very weak and the oscillatory motions induced by small waves predominated. The velocities plot in the stability fields of small 2-D ripples and small weakly asymmetrical 3-D ripples (Fig. 8A). These conditions would have weakly reworked the seabed to form wave ripples.

Under moderate storm conditions, both oscillatory and mean residual currents increased and the velocities moved briefly into the large, strongly asymmetrical 3-D ripple and plane-bed fields (Fig. 8B). In the waning phase of the storm, the history would have been reversed and the predicted depositional succession would consist of plane bed overlain by large asymmetrical 3-D ripples, small weakly asymmetrical 3-D ripples, and finally small 2-D (wave) ripples.

The major storm was characterized by large excursions in the mean residual velocity (Fig. 8C). These excursions moved the velocities through almost all the stability fields during the buildup of the storm, climaxing in the plane-bed field for approximately 30 hours. During the waning phase of the storm, the mean residual current diminished rapidly and deposition would have occurred under predominantly oscillatory conditions. The predicted bed succession would consist of plane bed, overlain by large weakly asymmetrical 3-D ripples, small weakly asymmetrical 3-D ripples, and small 2-D ripples.

A second approach to predicting sediment transport mode and bedforms follows the method of Li and Amos (1998; 1999). This approach calculates wave, current, and combined-flow shear velocities from the Grant and Madsen (1979) theory and then compares these with existing threshold criteria: the initiation of bedload transport of Miller et al. (1977), the suspension threshold of Bagnold (1956), and the upper-plane-bed criterion of Komar and Miller (1975). The thresholds used were those determined for 0.2 mm sand by Li and Amos (1999). The results shown in Figure 9A are for the skin-friction combined-flow shear velocity with no adjustment made for the effects of ripple and bedload enhancement. They indicate that bedload sediment transport would have been almost continuous and suspended-sediment transport would have been common, even under fair-weather conditions, at this water depth. The observed suspended-sediment concentrations (Fig. 7H) support this prediction only partially; small peaks are observed when wave heights increase slightly, but zero levels are observed at 30 cm above the seabed for extensive periods. However, given the fact that the middle line in Fig. 9A represents the onset (no matter how weak) of suspension and that the suspension concentration in Fig. 7H was measured at 30 cm height, the agreement between Figs. 7 and 9 is reasonable.

Under moderate storm conditions (Days 5 and 6), suspension and upper-plane-bed traction transport is predicted (Fig. 9A). These intervals were characterized by high suspended-sediment concentrations at 30 cm above the seabed (Fig. 7G). Under major storm conditions, the predominant transport modes would have been suspension and traction in upper-plane-bed conditions, giving the strong peak in suspended-sediment concentration, even at 1 m above the seabed (Fig. 7G). When the ripple- and bedload-enhanced shear velocities are used (recall that these are adjusted values that take into account roughness due to the presence of ripples and the thickness of the bedload transport layer; Li and Amos 1999), the model predicts almost continuous suspension and upper-plane-bed traction transport, with bedload-only transport being almost non-existent (Fig. 10).
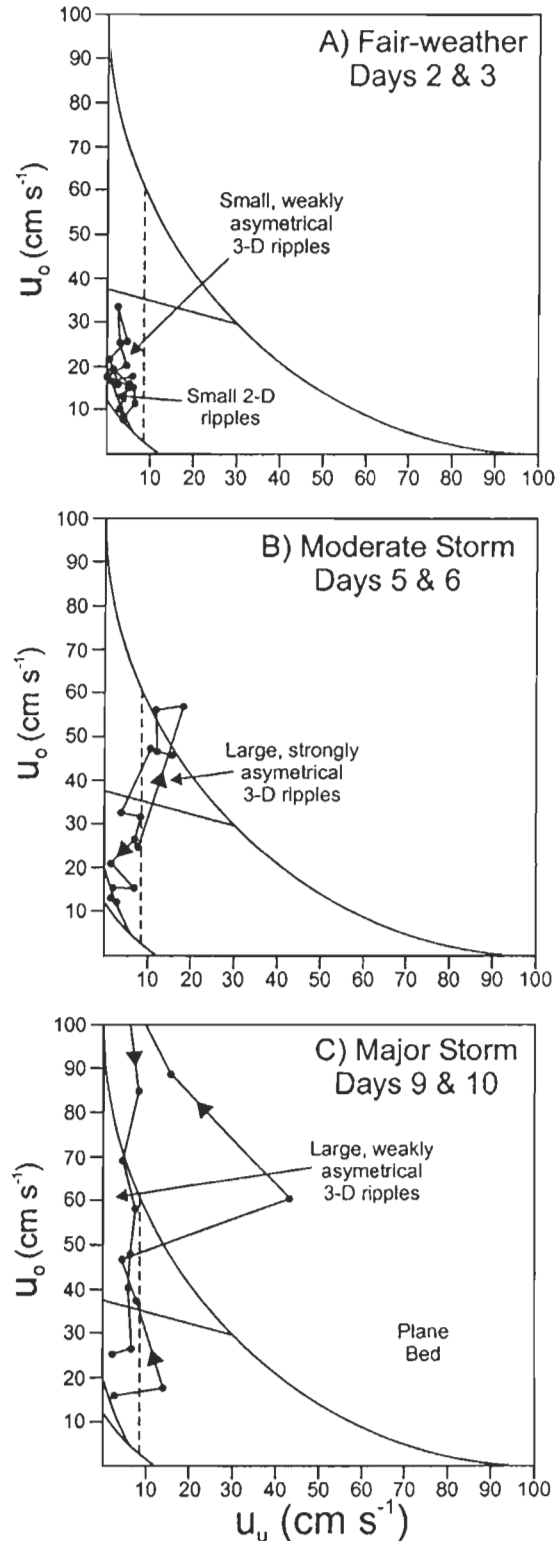

FIG. 8.—Bed-configuration stability diagram of Myrow and Southard (1991), showing flow trajectories for **A)** fair-weather, **B)** moderate storm, and **C)** major storm conditions. Axes are orbital velocity, u_o, and mean residual current velocity at 1 m above the seabed, u_u. In Part C, the u_o values exceed 1 m s^{-1} for more than 24 hours.
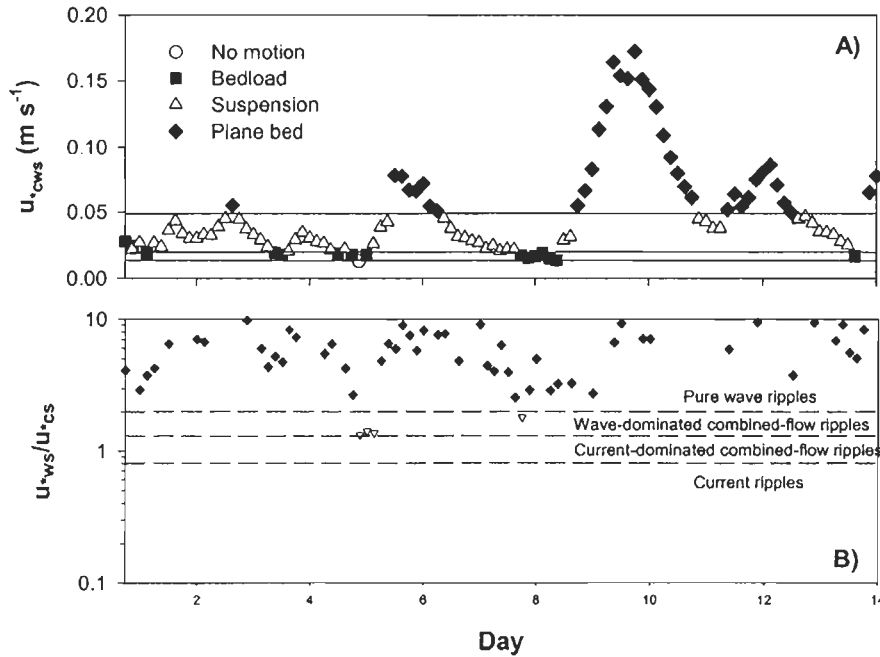
FIG. 9.—**A)** Time-series plot of the skin-friction combined shear velocity u_{*cws}. Computed transport modes are indicated by different symbols. The horizontal lines represent the critical shear velocities for bedload (u_{*cr}), saltation/suspension (u_{*crs}) and plane-bed (u_{*up}) transport respectively. **B)** Time-series plot of u_{*ws}/u_{*cs} and the predicted ripples types based on Li and Amos (1998). In this predictor, current-dominant ripples occur when the u_{*ws}/u_{*cs} ratio is less than 0.8, combined wave-current ripples between 0.8 and 1.3, wave-dominant ripples between 1.3 and 2, and pure wave ripples when u_{*ws}/u_{*cs} is greater than 2.

The Li and Amos (1998) bedform predictor uses the ratio of skin-friction wave shear velocity, u_{*ws}, to skin-friction current shear velocity, u_{*cs} (Fig. 9B). This predictor indicates that the bedforms in this water depth would be almost exclusively "pure wave ripples." Using the criteria established by Li and Amos (1998), combined-flow bedforms would be virtually nonexistent in this shallow-water environment except under conditions of near-calm.

DISCUSSION

Forcing Mechanisms

Before discussing the results, it should be pointed out that this study focused on processes that are active on this shoreface for only a short part of the year. Ice cover precludes significant wave activity for more than six months of the year. While it is not impossible that some of the observed facies, particularly the parallel-laminated and small-scale cross-laminated couplets, may be related to this strong seasonality, winter currents are not generally strong enough to mobilize the bed. Summer observations of the

mean current indicate that the tidal flow is small (Fig. 7D, E). Winter observations suggest that the ice cover attenuates the tidal flow (Ingram and Larouche 1987; Prinsenberg 1988). On the basis of these observations, it is most likely that winter conditions are represented by (if anything at all) mud drapes in the deeper-water facies.

As in most shoreface environments, the varying levels of wave energy control sediment transport and deposition. Both observations and calculations suggest strongly that, over the periods of wave motions, u_o dominates over u_u in controlling sediment mobility at 10 m water depth. Although u_u does increase with wind speed, it remains subordinate to wave orbital velocities at all times, except periods of near calm (Fig. 7F). However, the direction of u_u strongly influences the direction of net sediment transport. Under fair-weather conditions, u_u is weak and fluctuates at the 12.42 hr (semidiurnal) tidal period, but during storms, the amplitude of fluctuations in u_u increases significantly (Fig. 7). This increased amplitude appears to be related to inertial oscillations that, at this latitude, would have a period of approximately 14.6 hr. The 3-hr measurement interval makes separation of tidal and inertial motions difficult in the time-series data. However,
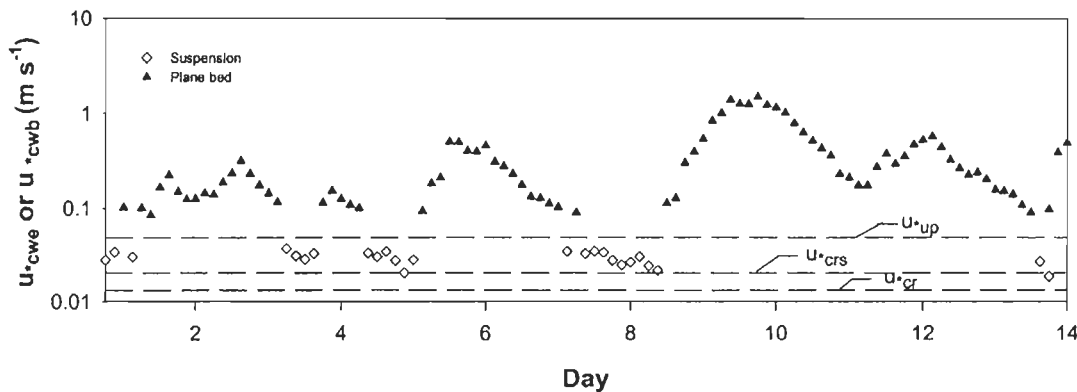

FIG. 10.—Time-series plot of the ripple-enhanced shear velocity u_{*cwe} and bedload shear velocity u_{*cwb}. Computed transport modes are indicated by different symbols. The dashed lines represent the established critical shear velocities for bedload (u_{*cr}), suspension (u_{*crs}) and plane-bed (u_{*up}) transport respectively.

clockwise rotation of u_u during the storm events is consistent with inertial oscillations in the northern hemisphere. During both the moderate storm of Days 5–6 and the major storm of Days 9–10, the high-amplitude current fluctuations lag the wind speed by a few hours. This is probably due to the wind initially acting on a surface brackish water layer that would have been physically decoupled from the underlying layer of marine water. This is seen in the initial southward flow of bottom water in the early stages of the moderate storm on Day 5 when the wind blew from the southeastern quadrant (Fig. 7). As the water column mixed through turbulent exchange, the depth-lagged inertial motion induced by the wind would have penetrated to the bottom, giving rise to the observed clockwise rotation of u_u.

The role of downwelling currents resulting from coastal setup is less clear. By the peak of the major storm, the mean water level had increased by more than 1 m and u_u turned suddenly to obliquely offshore (Fig. 7E, F), raising the possibility of a downwelling flow. However, the offshore flow was maintained for less than 12 hours and a significant quantitative correlation between water level and onshore–offshore current speed for the entire current record was not obtained. In previous studies from comparable environments, the downwelling flow was limited to very shallow depths and was observed to converge with the alongshore coastal current at depths greater than 5 m (Héquette and Hill 1993; Héquette et al. 2001). The influence of downwelling would therefore be difficult to discern in 10 m of water.

Bedforms

On the basis of the semiquantitative comparison possible here, our data give reasonable agreement with the Myrow and Southard (1991) bedform stability diagram (Fig. 8). The raised sections and cores attest to the predominance of small-scale wave-ripples, combined-flow ripples and plane-bed conditions. For the short time series collected, the current conditions would have remained for the greatest period of time in the field for small, weakly symmetrical ripples. During the storms, the current conditions move rapidly into the plane-bed field. Although the rising storm trajectory passes through the fields for small and large, strongly asymmetrical 3-D ripples, the transition is rapid, perhaps leaving little time for bed equilibration with the flow. Any bedforms produced would be unlikely to survive subsequent reworking under plane-bed conditions. The waning storm trajectory under which bedforms would be preserved varies from storm to storm. For the moderate storm, plane-bed conditions are just reached and sustained for 6 hours. The waning storm trajectory then includes 9 hours in the field for large, strongly asymmetrical 3-D ripples, before falling back into the field for small weakly asymmetrical 3-D ripples. For the major storm, the plane-bed condition is retained for considerably longer (> 24 hr) and the waning trajectory spends 12 hours in the field for large weakly asymmetrical 3-D ripples.

Although it is not known how representative these storms are of the wave and current regime at Grande-rivière-de-la-Baleine, the data do suggest that large 3-D ripples should be preserved at the measurement site (10 m water depth) during the waning phase of storms. Hummocky cross-stratified beds (Fig. 4) are preserved in cores from 20 m depth on the modern shoreface (Fig. 6), but no cores are available between 9 and 20 m. Hummocky beds are also present in the lower parts of the land sections, at approximately 6.5 m below the wave erosion surface (Fig. 2). This suggests a depth of deposition somewhat greater than 11 m, depending on the rates of sediment accumulation and relative sea-level fall. Presumably, above this depth, the u_o–u_u trajectories pass too rapidly through the fields for large 3-D ripples to allow their preservation. The upper shoreface is therefore characterized by bimodal conditions: high-energy plane-bed conditions during storms and low-energy, small wave-dominated ripple conditions during waning storm and fair-weather conditions. This produces the interbedded parallel-laminated and small-scale cross-laminated facies in the upper part of the shoreface succession. Combined-flow ripple cross-lami-

nation is most likely to have formed during storms when inertial and downwelling flows increase the mean residual component of flow.

The Li and Amos (1999) model supports these interpretations. Using skin-friction shear velocities, the predictor indicates that plane-bed conditions would predominate during all storms and even some fair-weather conditions when small local surface waves are generated (Fig. 9). However, the predictor seems to underestimate the threshold of suspension because the observed suspended-sediment concentrations do not become significant except during storms (Fig. 7G). Using the ripple-enhanced and bedload shear velocities makes this underestimation worse (Fig. 10). These discrepancies may be due to the nonlinear effects of wave transformation in shallow water or the fact that waves are strongly dominant in the present study, whereas the predictor of Li and Amos is based on mostly combined wave–current data.

The small disparities between the predicted depth of large 3-D ripples and their inferred paleo-depth are minor compared to the uncertainties implicit in the models. For example, the applicability of the Myrow and Southard (1991) diagram may not extend to the natural conditions of Grande-rivière-de-la-Baleine. The diagram is based on laboratory measurements that used a fixed grain size (0.09 mm) and a regular oscillation period (8.5 s) in the same direction as the current. The grain size is at the fine end of the natural range at 10 m water depth on the Grande-rivière-de-la-Baleine shoreface. In terms of wave period, the typical storm wave periods at Grande-rivière-de-la-Baleine were in the 6–7 s range and, of course, much more variable than in the laboratory experiments. The directions of wave oscillation and mean residual current are rarely parallel. Also, the values for u_u used in this paper correspond to values 100 cm above the bed, whereas the Myrow and Southard (1991) diagram is based on net downstream movement of a neutrally buoyant marker at an undefined depth in the flow (Arnott and Southard 1990). Finally, the Myrow and Southard (1991) diagram is generalized and the limit of plane-bed conditions was extrapolated beyond the laboratory data for high values of u_u.

Plotting values from field data (Li and Amos 1995) and from generalized cases produced by the SEDTRANS model (Li and Amos 1997; Davidson 2001) on the diagram suggests that the plane-bed limit should form a steeper curve than the one drawn by Myrow and Southard (1991) (Fig. 11). Inevitably, these data suffer from the same uncertainties as discussed above when compared to the laboratory-based example. Nevertheless, in both cases, the grain size used was larger than that used in the laboratory runs, so there is a case for displacing the plane-bed limit downwards for fine sand and thus significantly limiting the stability fields of the large 3-D ripples. On the other hand, given the probable underestimation of thresholds noted for the Li and Amos (1999) predictor using the ripple-enhanced shear velocity, the suggested plane-bed limit should be viewed with considerable caution.

The Li and Amos (1999) model has great potential as a tool for designing field studies and refining bedform stability diagrams for wave and combined-flow conditions. More field-based studies are, however, badly needed to extend the range of laboratory-based data and validate the model. The present results contain large uncertainties but also raise important questions. What are the best parameters to describe combined-flow conditions and take into account the numerous variables? What is the effect of high suspended-sediment concentrations and fluid density on bedform stability? How do the relative directions of oscillatory and mean residual components influence bedform geometry? Answers to these questions will require both further theoretical development and field work.

CONCLUSIONS

The shoreface at Grande-rivière-de-la-Baleine is a wave-dominated environment with a low tidal influence. The distinctive parallel-laminated and ripple-laminated fine sand facies found in raised deposits and cores results from alternating high-energy storm and fair-weather conditions. Existing
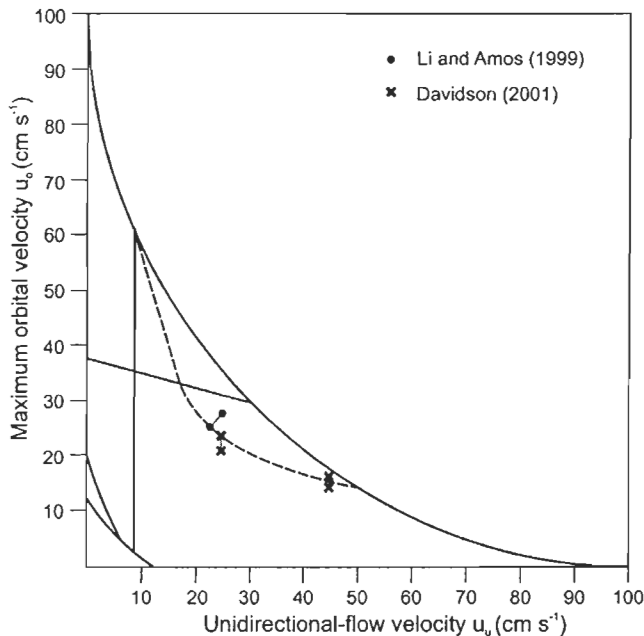
FIG. 11.—Data generated by the SEDTRANS model for conditions of plane-bed sediment transport. These data suggest that the limit of plane-bed conditions should be modified (dashed line). Data from Li and Amos (1999; 0.2 mm sand; 12.8 s wave period) and Davidson (2001; 0.125 mm sand; 5 s wave period).

models simulate this condition but require that the u_o–u_u trajectory of the waning storm pass rapidly through the large 3-D bedform fields to preclude deposition of hummocky cross–stratified beds. The latter occur at paleo-water depths slightly greater than that predicted by the models, but this disparity is minor compared to uncertainties in the models.

REFERENCES

ALLARD, M., AND TREMBLAY, G., 1983, La dynamique littorale des iles Manitounouk durant l'Holocene: Zeitsbrift für Geomorphologie, Supplementband 47, p. 61–95.

ARNOTT, R.W., 1993, Quasi-planar-laminated sandstone beds of the lower Cretaceous Bootlegger member, north-central Montana: evidence of combined-flow sedimentation: Journal of Sedimentary Petrology, v. 63, p. 488–494.

ARNOTT, R.W., AND SOUTHARD, J.B., 1990, Exploratory flow-duct experiments on combined-flow bed configurations, and some implications for interpreting storm-event stratification: Journal of Sedimentary Petrology, v. 60, p. 211–219.

BAGNOLD, R.A., 1956, Flow of cohesionless grains in fluids: Royal Society (London), Philosophical Transactions, v. A249, p. 235–297.

BHATTACHARYA, J.P., AND WALKER, R.G., 1992, Deltas, *in* Walker, R.G., and James, N.P., eds., Facies Models: Geological Association of Canada, p. 157–177.

DAVIDSON, S.H., 2001, Evaluation of the SEDTRANS96 Numerical Model for Scientific Use on the Fraser Delta: Unpublished technical report, SeaScience Inc., Vancouver, B.C., 34 p.

GONTHIER, N., ANGLEJAN B., AND JOSENHANS, H.W., 1993, Seismo-stratigraphy and sedimentology of Holocene sediments off Grande Rivière de la Baleine, southeastern Hudson Bay, Quebec: Géographie Physique et Quaternaire, v. 47, p. 147–166.

GRANT W.D., AND MADSEN, O.S., 1979, Combined wave and current interaction with a rough bottom: Journal of Geophysical Research, v. C84, p. 1797–1808.

GRANT W.D., AND MADSEN, O.S., 1986, The continental shelf bottom boundary layer: Annual Review of Fluid Mechanics, v. 18, p. 265–305.

HARMS, J.C., 1969, Hydraulic significance of some sand ripples: Geological Society of America, Bulletin, v. 80, p. 363–396.

HARMS, J.C., SOUTHARD, J.B., AND WALKER, R.G., 1982, Structures and Sequences in Clastic Rocks: Society of Economic Paleontologists and Mineralogists, Short Course Notes 9.

HÉQUETTE, A., AND HILL, P.R., 1993, Storm-generated current and offshore sediment transport on a sandy beach shoreface, Tibjak Beach, Canadian Beaufort Sea: Marine Geology, v. 113, p. 283–304.

HÉQUETTE, A., DESROSIERS, M., HILL, P.R., AND FORBES, D.L., 2001, The influence of coastal morphology on shoreface sediment transport under storm combined flows, Canadian Beaufort Sea: Journal of Coastal Research, v. 17, p. 507–516.

HILL, P.R., ROBERGE, M., AND LONGUEPÉE, H., 1998, Live from Canada: Forced regression in action; deltaic shoreface sandbodies being formed (Abstract): International Sedimentological Congress, Alicante, Spain, 13–17 April, 1998.

HILLAIRE-MARCEL, C., 1976, La déglaciation et le relèvement isostatique à l'est de la Baie d'Hudson: Cahiers de Géographie du Québec, v. 20, p. 185–220.

INGRAM, R.G., AND LAROUCHE, P., 1987, Variability of an under-ice river plume in Hudson Bay: Journal of Geophysical Research, v. C92, p. 9541–9547.

KOMAR, P.D., AND MILLER, M.C., 1975, The initiation of oscillatory ripple marks and the development of plane-bed at high shear stresses under waves: Journal of Sedimentary Petrology, v. 45, p. 697–703.

LI, M.Z., AND AMOS, C.L., 1995, SEDTRANS92: A sediment transport model for continental shelves: Computers and Geosciences, v. 21, p. 533–554.

LI, M.Z., AND AMOS, C.L., 1997, SEDTRANS96: Upgrade and calibration of the GSC sediment transport model: Geological Survey of Canada, Open File 3512, 139 p.

LI, M.Z., AND AMOS, C.L., 1998, Predicting ripple geometry and bed roughness under combined waves and currents in a continental shelf environment: Continental Shelf Research, v. 18, p. 941–970.

LI, M.Z., AND AMOS, C.L., 1999, Field observations of bedforms and sediment transport thresholds of fine sand under combined waves and currents: Marine Geology, v. 158, p. 147–160.

LI, M.Z., WRIGHT, L.D., AND AMOS, C.L., 1996, Predicting ripple roughness and sediment resuspension under combined flows in a shoreface environment: Marine Geology, v. 130, p. 139–161.

LONGUEPÉE, H., 2000, Distribution des figures et faciès sédimentaires d'un delta en régression forcée, Grande-rivière-de-la-Baleine, Nouveau-Québec [unpublished M.Sc. thesis]: Université du Québec à Rimouski, 181 p.

MILLER, M.C., McCAVE, I.N., AND KOMAR, P.D., 1977, Threshold of sediment motion under unidirectional currents: Sedimentology, v. 24, p. 507–527.

MYROW, P.M., AND SOUTHARD, J.B., 1991, Combined flow model for vertical stratification sequences in shallow marine storm-deposited beds: Journal of Sedimentary Petrology, v. 61, p. 202–210.

NIEDORODA, A.W., AND SWIFT, D.J.P., 1981, Maintenance of the shoreface by wave orbital currents and mean flow: observations from the Long Island Coast: Geophysical Research Letters, v. 8, p. 337–340.

PRINSENBERG, S.J., 1988, Damping and phase advance of the tide in western Hudson Bay by the annual ice cover: Journal of Physical Oceanography, v. 18, p. 1744–1751.

READING, H.G., AND COLLINSON, J.D., 1996, Clastic Coasts, *in* Reading, H.G., ed., Sedimentary Environments: Processes, Facies and Stratigraphy: Blackwell Science, p. 154–231.

ROBERGE, M., 1998, Morpho-stratigraphie d'un delta en régression forcée, Grande rivière de la Baleine, Hudsonie [unpublished M.Sc. thesis]: Université du Québec à Rimouski, 153 p.

RUZ, M.-H., AND ALLARD, M., 1994, Foredune development along a subarctic emerging coastline, eastern Hudson Bay, Canada: Marine Geology, v. 117, p. 57–74.

SOUTHARD, J.B., LAMBIE, J.M., FEDERICO, D.C., PILE, H.T., AND WEIDMAN, C.R., 1990, Experiments on bed configuration on fine sands under bidirectional purely oscillatory flow, and the origin of hummocky cross-stratification: Journal of Sedimentology Petrology, v. 60, p. 1–17.

WALKER, R.G., AND PLINT, A.G., 1992, Wave- and storm-dominated shallow marine systems, *in* Walker, R.G., and James, N.P., eds., Facies Models: Geological Association of Canada, p. 219–238.

WRIGHT, L.D., BOON, J.D., KIM, S.C., AND LIST, J.H., 1991, Modes of cross-shore sediment transport on the shoreface of the Middle Atlantic Bight: Marine Geology, v. 96, p. 19–51.

YOKOKAWA, M., 1995, Combined-flow ripples: genetic experiments and applications for geologic records: Kyushu University, Memoirs of the Faculty of Science, Series D. Earth and Planetary Sciences, v. 29, p. 1–38.
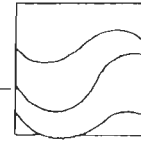
ANNEXE A2

Numerical study of sedimentary impact of a storm on a sand beach simulated by hydrodynamic and sedimentary models

Samuel MEULÉ[a], Christel PINAZO[a]*, Claude DEGIOVANNI[a], Jean-Paul BARUSSEAU[b], Maurice LIBES[a]

[a] Centre d'océanologie de Marseille, université de la Méditerranée, station marine d'Endoume, chemin de la Batterie-des-Lions, 13007 Marseille, France
[b] Centre de formation et de recherche sur l'environnement marin, université de Perpignan, 52, av. de Villeneuve, 66860 Perpignan, France

Abstract – In marine coastal environments, storms have a major morphological impact on sand beaches. This study, part of the French Programme National d'Environnement Côtier, consisted in developing and applying hydrodynamic and sedimentary models to simulate the major processes that modify sand beaches. In order to study sediment dynamics, we developed three models to simulate waves, currents and sediment transport associated with a storm event. The wave model was a Mild Slope Equation model based on the parabolic approximation of the refraction-diffraction equation of Berkhoff. The hydrodynamic model was obtained by the depth-average of Navier Stockes' equations forced by the terms of radiation stresses induced by waves. The sedimentary model SEDSIM developed by Martinez and Harbaugh computed, by using empirical formulations, the transport, sorting, erosion and deposit of sediment. The numerical simulations computed the impact of a realistic storm event on a relatively realistic microtidal beach with wave-formed sand bars. The results show that after 15 h of storm, the beach receded on more than 20 m. Two sedimentary bars and an orthogonal sand structure were removed and levelled. A tendency towards a single bar was observed. © 2001 Ifremer/CNRS/IRD/Éditions scientifiques et médicales Elsevier SAS

Résumé – Études numériques de l'impact sédimentaire d'une tempête sur une plage sableuse simulé avec des modèles hydrodynamiques et sédimentaires. Dans les zones littorales, les tempêtes ont un impact important sur la morphologie des plages sableuses. Cette étude intégrant le Programme national d'environnement côtier avait pour objectif de développer et d'appliquer des modèles hydrodynamiques et sédimentaires afin de simuler les processus dominants qui modifient les plages sableuses. Nous avons donc développé trois modèles pour simuler la propagation de la houle, les courants, et le transport sédimentaire associés à un coup de mer. Le modèle de houle est une approximation parabolique de l'équation de réfraction-diffraction de Berkhoff. Le modèle hydrodynamique est obtenu en intégrant sur la verticale les équations de Navier Stockes forcées par les termes de tension radiative induits par la houle. Le modèle sédimentaire Sedsim développé par Martinez et Harbaugh calcule par des formulations empiriques le transport, le tri, l'érosion et le dépôt des sédiments. Les simulations ont été faites à partir d'un scénario de tempête réelle ayant affecté une morphologie relativement réaliste de plage microtidale à barre d'avant-côte. Elles révèlent qu'après 15 h de tempête, la plage recule de plus de 20 m. Deux barres d'avant côte et une structure sableuse transversale se sont déplacées et ont été aplanies. Une tendance à ce qu'une seule barre d'avant côte subsiste est observée. © 2001 Ifremer/CNRS/IRD/Éditions scientifiques et médicales Elsevier SAS

171

**Correspondence and reprints.*
E-mail address: pinazo@com.univ-mrs.fr (C. Pinazo).

beach modification / numerical models / sediment transport / storm / wave-induced current

modification de la plage / modèles numériques / transport sédimentaire / tempête / courants induits par la houle

1. INTRODUCTION

The present work focused on the impact of storms on non-cohesive sand beaches located in the NW Mediterranean coastal zone. From observations, it resulted that the major modifications of the coastline occurred during storms (Barusseau et al., 1994). The physical processes in a sand beach were very complex. As waves moved towards the shore, the water moved along the seabed. It encountered more friction, allowing transport of sediment. When waves broke, they caused turbulence that suspended, sorted and transported sediment backwards with undertow. Much of the energy released by breaking waves drove longshore-currents and rip-currents. Some energy continued to propagate shorewards in the swash zone, where waves were reflected backwards towards the sea.

The main sedimentary processes, modifying sand beaches morphology during a storm, are well described in the literature (Ottamn, 1965; Ingle, 1966; Zenkovitch, 1967; King, 1972; Barusseau et al., 1991, 1994; Blanc and Poydenot, 1993). The evolution of the topographic profile resulted both from a cross-shore movement and a longshore movement. Hence, we observed a recession of the shoreline, a sand bar movement, and a levelling in the submarine beach topography.

Thus, to simulate these complex processes occurring nearshore, a coupled system of numerical models was developed (*figure 1*). Three models, a wave propagation model, a wave-induced current model and a sediment dynamics model, were integrated. The wave model was a Mild Slope Equation model based on the parabolic approximation of the refraction-diffraction equation of Berkhoff (1972, 1976). The hydrodynamic model solved the equations of Navier Stokes incorporating terms of radiation stresses induced by waves (Longuet-Higgins, 1970). The radiation stress was the excess of momentum flux due to wave propagation, which drove wave-induced currents such as longshore and rip-currents. Martinez and

Harbaugh developed the sedimentary model SEDSIM (Martinez and Harbaugh, 1993). It computed from empirical formulations the transport, the sorting, the erosion and the deposition of sediment.

These models were applied to a theoretical sand beach including the main typical features of the nearshore zones of the Gulf of Lions. Then, the beach presented a stable system of two quasi-continuous shore-parallel wave-formed sand bars and an orthogonal one.

2. MODELS DESCRIPTION

2.1. Wave model

The propagation of a monochromatic wave could be modelled with the elliptic equation of Berkhoff (1972, 1976):

$$\nabla(\,CCg\,\nabla(\,\phi\,)\,) + k^2\,CCg\phi = 0$$

in which C is the phase velocity ($= \omega/k$ with ω the wave angular frequency), k the wave number, ϕ the horizontal velocity potential and Cg the group velocity.

But, it was easier to project the main direction of wave propagation on the x-axis and to solve the parabolic equation of Berkhoff, named Mild Slope Equation:

$$\frac{\partial \phi}{\partial x} = \left(ik - \frac{1}{2\,kCCg}\,\frac{\partial kCCg}{\partial x} \right) \phi + \frac{i}{2\,kCCg}\,\frac{\partial}{\partial y}\left(CCg\,\frac{\partial \phi}{\partial y} \right)$$

in which i is an imaginary number.

However, the use of the model implied some restriction on the direction of the wave propagation. Generally, the angle was less than 60° and for waves propagated from deep water to the coast with directional changes less than 90°.

Due to waves breaking – determined by the Battjes' test with breaking criterion 0.8–1.2 (Battjes, 1982) – the
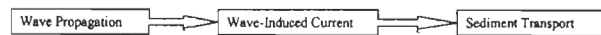

Figure 1. Coupled system of numerical models.

height of waves in surf zone was recalculated from the equation of Stive and Wind (1982).

$$\frac{\partial \eta}{\partial x} + \frac{\eta}{4h}\frac{\partial h}{\partial x} = A\left(\frac{h}{gT^2}\right)^{\frac{1}{2}}\left(\frac{\eta}{h}\right)^2$$

in which η is the surface elevation, h the depth, A the amplitude (= $H/2$, where H is the wave height), g the acceleration due to gravity and T the period.

An implicit Crank-Nicholson numerical scheme was developed to calculate wave propagation.

2.2. Current model

The wave model displayed the wave features as orbital and phase velocities, height, period and surface elevation, allowing the current model to solve the depth-average of Navier and Stockes' equations and to calculate the wave-induced currents from terms of radiation stress (Longuet-Higgins, 1970).

$$\frac{\partial \bar{\eta}}{\partial t} + \frac{\partial \bar{U}}{\partial x} + \frac{\partial \bar{V}}{\partial y} = 0$$

$$\frac{\partial \bar{U}}{\partial t} + U\frac{\partial \bar{U}}{\partial x} + V\frac{\partial \bar{U}}{\partial y} = -g(h+\bar{\eta})\frac{\partial \bar{\eta}}{\partial x} + \frac{1}{\rho}(\tau_{xx} + \tau_{xy} + \tau_{bx} + \tau_{wx}) + \frac{\partial}{\partial x}\left(\upsilon_{xx}\frac{\partial \bar{U}}{\partial x}\right) + \frac{\partial}{\partial y}\left(\upsilon_{xy}\frac{\partial \bar{U}}{\partial y}\right) + f\bar{V}$$

$$\frac{\partial \bar{V}}{\partial t} + U\frac{\partial \bar{V}}{\partial x} + V\frac{\partial \bar{V}}{\partial y} = -g(h+\bar{\eta})\frac{\partial \bar{\eta}}{\partial y} + \frac{1}{\rho}(\tau_{yy} + \tau_{yx} + \tau_{by} + \tau_{wy}) + \frac{\partial}{\partial x}\left(\upsilon_{yx}\frac{\partial \bar{V}}{\partial y}\right) + \frac{\partial}{\partial y}\left(\upsilon_{yy}\frac{\partial \bar{V}}{\partial y}\right) - f\bar{U}$$

These are equations for conservation of momentum and energy in which $\bar{\eta}$ is the mean surface elevation, $\bar{U}$ and $\bar{V}$ the mean horizontal currents, τ_b the bed shear stress and τ_w the wind shear stress. No wind stress was considered. The diffusion $\nu_{ij} = 0.15Hu^*$ was isotropic, homogeneous and effective, calculated by the equation of Fisher with the shear velocity u^*. The small tidal variation in sea-level and the Coriolis effects were negligible at the scale of our study.

The excess of momentum flux $S_{i,j}$ was calculated from a formulation of Longuet-Higgins and Stewart (1964).

$$S_{xx} = \frac{\rho g H^2}{8}\left(\left(2n - \frac{1}{2}\right)\cos^2\theta + \left(n - \frac{1}{2}\right)\sin^2\theta\right)$$

$$S_{yy} = \frac{\rho g H^2}{8}\left(\left(2n - \frac{1}{2}\right)\sin^2\theta + \left(n - \frac{1}{2}\right)\cos^2\theta\right)$$

$$S_{xy} = S_{yx} = \frac{\rho g}{8}H^2\,n\,.\,\cos\theta\,.\,\sin\theta$$

These are components of radiation stress (excess momentum flux) where n is C_g/C, θ the wave angle, g the acceleration due to the gravity, ρ the density and H the mean height of waves.

An upwind and an alternative direction scheme were applied to calculate the current field. We had restricted the coast to an impermeable boundary and imposed Sommerfeld radiation conditions for lateral open boundaries (Sommerfeld, 1949; Miller and Thorpe, 1981).

2.3. Sedimentary model

The sedimentary model SEDSIM was used to calculate the transport, the erosion, the sorting and the deposit of sediment.

First, the model calculated the total transport rate of sediment (Inman and Bagnold, 1963) according to the waves and the wave-induced currents.

$$Q = K(E_b\,C_b)\cos\alpha_b(v_l/u_{max})$$

This represents total longshore transport rate in which Q is the longshore transport rate (immersed weight), K a calibration coefficient (= 0.77), E_b the wave energy density at the breaker zone, C_b the group velocity at the breaker zone, α the angle of wave incidence at the breaker zone, v_l the average longshore velocity and u_{max} the maximum orbital velocity.

Second, at each grid point, a local transport rate $Q_{i,j}$ was calculated in function of the local maximum orbital velocity (Horikawa, 1988).

$$Q_{i,j} = Q\left(\frac{u_{i,j}}{u_{tot}}\right)$$

represents the local transport rate in which $u_{i,j}$ is the maximum orbital velocity at grid location (i,j) and u_{tot} the sum of maximum orbital velocity.

419

Third, the conservation of sediment determined the amount of sediment available to be moved. These thickness of the upper sediment cell (i,j) is the active layer thickness Δz. It changed during simulation to:

$$\Delta z = \frac{Q_{i,j}}{\Delta x \, \Delta y} \Delta t$$

The variation of the thickness Δz was calculated from the local transport rate $Q_{i,j}$ the size of the grid-cell ($\Delta x \, \Delta y$) and the time step Δt.

Fourth, the sorting was calculated from different transport efficiencies determined from respective turbulence effects, fall velocity, critical shear stress and bottom shear stress of different grain sizes (Slingerland and Smith, 1986; Komar, 1989; Martinez and Harbaugh, 1993).

$$Vol = \sum_{ks} Vol \cdot \varepsilon_{ks}$$

in which Vol is the displacement volume, ks a type of grain and ε_{ks} the relative capacity of transport of each grain size.

Finally, after being transported by wave-induced currents, the sediment was deposited on the upper sediment cell.

2.4. Numerical methods

Four grids were used in this work (*figure 2*). Three two-dimensional grids in (x, y)-space represented the bathymetry, the current field and the sediment transport. A three-dimensional grid in (x, y, θ)-space computed the wave field. Each grid could have different resolution and orientation in (x, y)-space as long as the current grid was covered by the wave grid. The values of Δx and Δy were based on the numerical stability criterion of Courant-Friedrichs-Levy (CFL) described by Vreugdenhil (1989).

$$\Delta t \leq \frac{1}{\sqrt{gh}} \left(\frac{1}{\Delta x^2} + \frac{1}{\Delta y^2} \right)^{-\frac{1}{2}}$$

represents the CFL criterion in which g is the acceleration of gravity and h the depth in deep water.
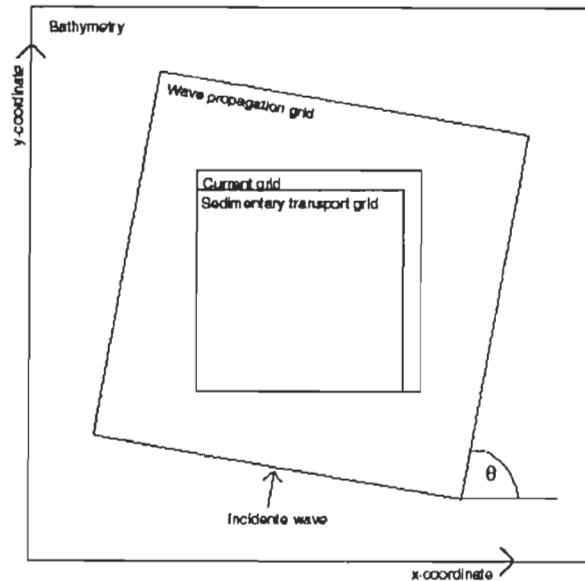

Figure 2. Numerical grid location.

The very high spatial resolution required in coastal areas would demand too many computer capabilities. For reasons of efficiency, the computations were made on regular grids.

To assess the behaviour of the models in regard to hydrodynamics problems, they were applied to a rather basic idealised situation for which the results could be compared with information in the literature (test on a circular bay from the French Laboratoire National d'Hydraulique). These results were deemed satisfying.

3. SIMULATION CONDITIONS

To test the models in relatively realistic geophysical conditions, the models were applied to a stable system of quasi-continuous shore-parallel wave-formed sand bars. This type of area was chosen because it is a common type of beach in the nearshore zone of the Gulf of Lions. The model results could be also compared with the results of a well-documented field. The shape, the number, and the degree of stability of the sand-bars is variable along the coast, following its local exposure to the dominant waves, the proximity of headlands, the slope and grain-size equilibrium, the volume of sediment in movement and the presence of sea defence structures
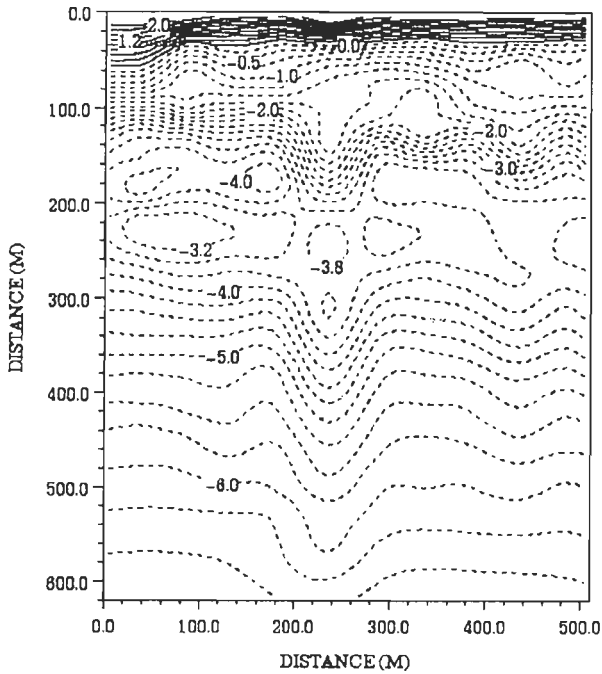
Figure 3. Initial bathymetry of the theoretical beach. Units in meters. The equidistance is 0.25 m.

Figure 4. Phase angles of a wave propagating with an incidence of 80°.

(Ingle, 1966; Zenkovitch, 1967; Barusseau and Saint-Guily, 1981; Barusseau et al., 1991, 1994).

3.1. Initial bathymetry of the beach

We chose to test the models on an initial coastal zone (500 × 610 m) (*figure 3*) with two shore-parallel wave-formed bars developed in the nearshore: an inner-bar at a distance of 80 m from the shoreline and an outer-bar at a distance of 200 m from the shoreline. In addition, there was another sand structure orthogonal to the shore in the middle of the computed field. This sand bar was assimilated to an oblique bar. However, in sand beaches, an orthogonal structure could be present (Barcilon and Lau, 1973). Further, the beach was rather plane with a global slope of 1:80.

The nature of sediments was assessed from studies of sediment core samples. We imposed four grain size characteristics with a coherent spatial distribution. The amount of sediment in each point of the grid was estimated according to the gradual passage from coarse size near the coast towards fine size in deep water.

3.2. Hydrodynamics conditions

For a realistic field situation, we chose to compute for a 15-h storm event. In this work, we changed the features of waves each 4 h. In this way, the model system was run with an increase of the height and the period. The waves penetrated the area in deep water at an incidence angle of $\theta = 80°$.

4. RESULTS

In *figure 4*, we can see the phase angles of the major wave occurring after 12 h of storm. Indeed, the major modifications occurred with this major wave regime. We showed that when wave moved towards the shore, there was a relatively important refraction. Thus, the crest line of wave was fitted with isobaths geometry. The pattern of the wave propagation was modified on the different sand structures, and more especially on the location of the orthogonal structure.

In *figure 5*, arrows show the wave-induced currents for the previous wave regime superimposed on initial
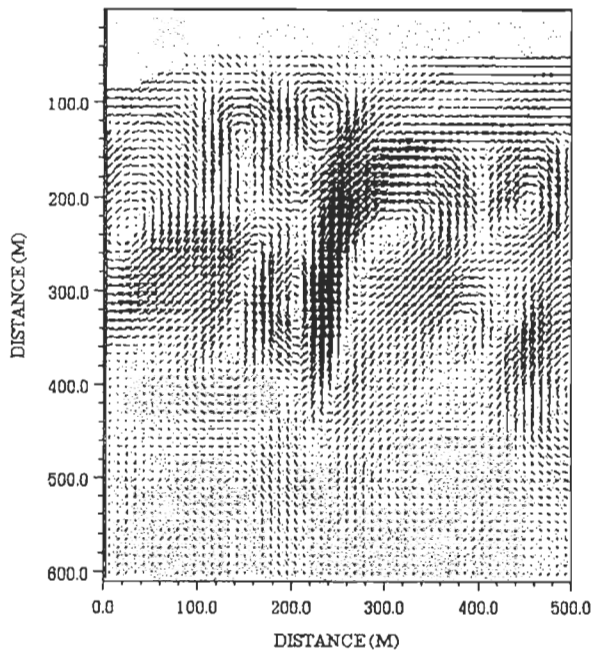
**Figure 5.** Wave-induced current field ($\rightarrow$ = 2.88 m·s⁻¹).
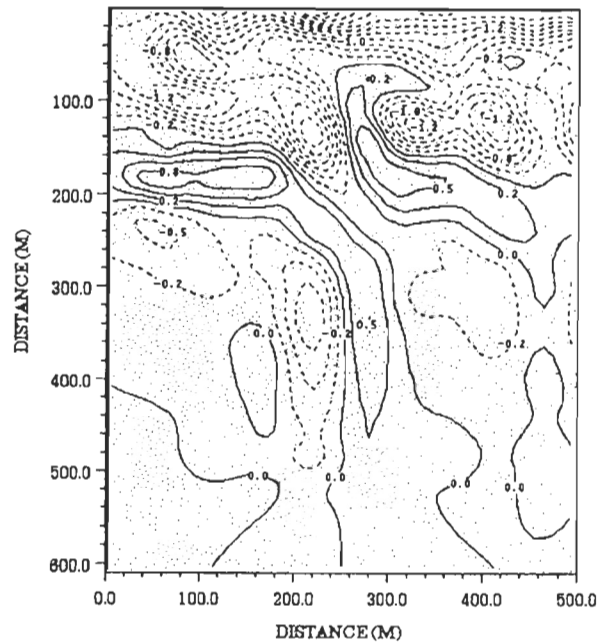
Figure 6. Zones of erosion and deposit after 15 h of simulation. Dashed lines (---) show erosion in meters and solid lines (——) show deposition of sediment in meters.

bathymetry. The currents were more intense in the surf zone. A shore parallel movement was settled in the inner-interbar. However, this wave-generated longshore-current was limited to the right of the computational grid. The presence of the orthogonal structure divided the currents and in this way created disturbance and different cells of secondary circulation.

As a result of sediment transport, it is interesting to examine where the zones of deposit and transport are located. In *figure 6*, dashed lines show erosion and solid lines show deposition of sediment. The coastline and the inner-bar were in erosion. Moreover, the intensive bottom erosion occurred mainly in front of the outer-bar and the orthogonal structure submitted to the waves. There was erosion, transport and deposit behind the outer-bar and the orthogonal structure. But usually, an erosional trend could be observed.

So after these modifications, the bathymetry after 15 h of simulation was considerably reshaped (*figure 7*). The coastline receded on more than 20 m. The inner-bar, the outer-bar and the orthogonal structure were levelled and moved shorewards, in the direction of the wave propagation. Two sand bars remained but a tendency towards a single bar profile seemed to begin.
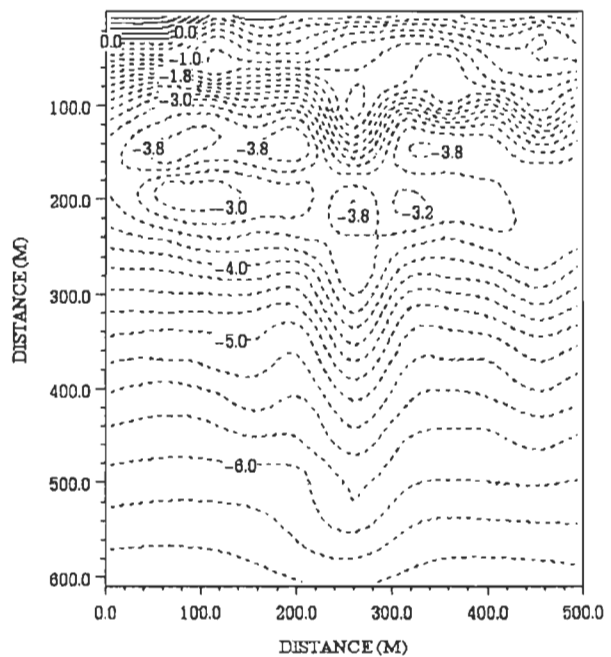

Figure 7. New bathymetry after 15 h of simulation. Units in meters. The equidistance is 0.25 m.

5. CONCLUSION

The wave propagation towards the coast released energy that created longshore-currents and rip-currents. The corresponding sediment movement induced a net longshore sediment transport, a recession of the shoreline, and a sand bar movement. The overall wave-energy distributions induced a topographic feed-back effect complicating the sediment movement patterns. The transport directions inferred from the morphological evolution.

In a qualitative view, the results of this study were in good agreement with the morphological changes, observed in the literature after a storm on a beach with wave-formed sand bars (Ingle, 1966; Ottamn, 1965; Zenkovitch, 1967; King, 1972; Barusseau et al., 1991, 1994; Blanc and Poydenot, 1993).

The model tried to simulate the real phenomena occurring in a beach. Sedimentary models seemed to give goods results at a large scale (Kim et al., 1997; Lou and Ridd, 1997; Zhang et al., 1998). The sand bar formation and theirs movements in the nearshore zone, described by Barusseau and coworkers (Barusseau and Saint-Guily, 1981; Barusseau et al., 1991, 1994), could even be simulated (Boczar-Karakiewicz and Davidson-Arnott, 1987; Mei and Liu, 1993). In this way, we observed that the inner-bars were levelled, and the outer-bars moved towards the sea. In this study, the sedimentary movement toward the sea did not exist. However, we noticed an accumulation of sand offshore, out of the valid numerical grid.

The formation of sand bars (Boczar-Karakiewicz and Davidson-Arnott, 1987) could be caused by breaking waves (Komar, 1976; Barusseau et al., 1994) or by infragravity waves. In this study, the coupled system of numerical models did not compute the infragravity waves. But considering the results, these models were very encouraging. We could imagine as did Wright et al. (1991) that incident waves cause shoreward transport whereas the interactions of incident waves with infragravity waves cause seaward transport.

The presented models may be powerful tools for studying beach modifications, predicting the main tendencies and estimating the optimal features of coastal builds. The next step is the validation of the model. We will apply the model to a realistic field like the Beach of Sète studied in the PNEC.

REFERENCES

Barcilon, A.I., Lau, J.P., 1973. A model of formation of transverse bars. J. Geophys. Res. 78, 2656–2664.

Barusseau, J.P., Saint-Guily, B., 1981. Disposition, caractère et formation des barres d'avant-côte festonnées du Golfe du Lion. Oceanol. Acta 4, 297–303.

Barusseau, J.P., Brisseaux, L., Drapeau, G., Long, B., 1991. Processus hydrodynamiques et morphosédimentaires de l'environnement des barres d'avant côte du littoral du golfe du Lion, Oceanol. Acta, Actes du Colloque International sur l'environnement des mers épicontinentales, Lille, 20–22 mars 1990, Special issue 11, pp. 163–176.

Barusseau, J.P., Radulescu, M., Descamps, C., Akouango, E., Gerbe, A., 1994. Morphosedimentary multiyears changes on a barred coast (Gulf of Lions, Mediterranean Sea, France). Mar. Geol. 122, 47–62.

Battjes, J.A., 1982. A case study of wave height variations due to currents in a tidal entrance. Coast. Eng. 6, 47–57.

Berkhoff, J.C.W., 1972. Computation of combined refraction-diffraction. Proc. 13th Int. Conf. Coast. Eng. Vancouver.

Berkhoff, J.C.W., 1976. Mathematical models for simple harmonic linear water waves, wave diffraction and refraction. Delft Hydraulics Laboratory, Publ. No. 163.

Blanc, J.J., Poydenot, F., 1993. Le rivage de Faraman en Camargue (SE. France): un géosystème côtier en déséquilibre; méthode d'étude, conséquences pratiques. Géol. Médit. XX, 75–87.

Boczar-Karakiewicz, B., Davidson-Arnott, R.G.D., 1987. Nearshore bar formation by non-linear wave processes, a comparison of models results and field data. Mar. Geol. 77, 287–304.

Horikawa, K., 1988. Nearshore Dynamics and Coastal Processes, Theory, Measurement, and Predictive Models. University of Tokyo Press, Tokyo, pp. 1–522.

Ingle, J.C. Jr, 1966. The Movement of Beach Sand. Elsevier, New York.

Inman, D.L., Bagnold, R.A., 1963. Littoral processes. In: Hill, M.H. (Ed.), The Seas: Ideas and Observations on Progress in the Study of the Seas. Wiley & Sons, New York, pp. 529–553.

Kim, S.C., Wright, L.D., Kim, B.O., 1997. The combined effects of synoptic-scale meteorological events on bed stress and sediment transport on the inner shelf of the Middle Atlantic Bight. Cont. Shelf Res. 17, 407–433.

King, C.A.M., 1972. Beaches and Coasts. Edward Arnold, London.

Komar, P., 1976. Beach Process and Sedimentation. Prentice-Hall, Englefield Cliffs, New Jersey.

Komar, P., 1989. Physical processes of waves and currents and the formation of marine placers. CRC Crit. Rev. Aquat. Sci. 1, 393–423.

Longuet-Higgins, M.S., 1970. Longshore currents generated by obliquely incident sea waves 1 and 2. J. Geophys. Res. 75, 6778–6801.

Longuet-Higgins, M.S., Stewart, R.W., 1964. Radiation stresses in water waves – a physical discussion with application. Deep-Sea Res. 11, 529–563.

Lou, J., Ridd, P.V., 1997. Modelling of suspended sediment transport in coastal areas under waves and currents. Estuarine Coast. Shelf Sci. 45, 1–16.

Martinez, P.A., Harbaugh, J.W., 1993. Simulating Nearshore Environments, Computer Methods in the Geosciences. Pergamon Press.

Mei, C.C., Liu, P.L.F., 1993. Surface waves and coastal dynamics. Annu. Rev. Fluid Mech. 25, 215–240.

Miller, M.J., Thorpe, A.J., 1981. Radiation conditions for the lateral boundaries of limited-area numerical models. Quart. J. R. Met. Soc. 107, 615–628.

Ottamn, F., 1965. Introduction à la géologie marine et littorale. Masson, Paris.

Slingerland, R., Smith, N.D., 1986. Occurrence and formation of water-laid placers. Ann. Rev. Earth Planet. Sci. 14, 113–147.

Sommerfeld, A., 1949. Partial differential equations: Lectures in Theoretical Physics, No. 6. Academic Press.

Stive, M.J.F., Wind, H.G., 1982. A study of radiation stress and set up in the nearshore region. Coast. Eng. 6, 1–25.

Vreugdenhil, C.B., 1989. Computation Hydraulics, An introduction. Springer.

Wright, L.D., Boon, J.D., Kim, S.C., List, J.H., 1991. Modes of cross-shore sediment transport on the shoreface of the Middle Atlantic Bight. Mar. Geol. 96, 19–51.

Zenkovitch, V.P., 1967. Processes of Coastal Development. Interscience, New York.

Zhang, Y., Swift, D.J.P., Yu, Z., Jin, L., 1998. Modelling of coastal profile evolution on the abandoned delta of the Huanghe River. Mar. Geol. 145, 133–148.

ANNEXE A3

Swell transformation on a microtidal barred beach

(Sète, France)

Raphaël Certain[a,*], Samuel Meulé[b], Vincent Rey[c], Christel Pinazo[b]

[a,*] *Laboratoire d'Etudes des Géo-Environnements Marins, Université de Perpignan, 52 av. P Alduy, 66860 Perpignan, France. Tel.: (00 33) 4 68 66 17 45. E-mail: certain@univ-perp.fr*

[b] *Laboratoire d'Océanologie et de Bio-Géochimie, Centre d'Océanologie de Marseille, UMR 6535, Université de La Méditerranée, Rue de la batterie des Lions, 13000 Marseille, France. Tel.: (00 33) 4 91 04 16 45. E-mail : samuel.meule@com.univ-mrs.fr*

[c] *LSEET-LEPI, UMR- 6017 du CNRS, Université du Sud Toulon-Var, BP 132, F-83957, La Garde Cedex, France. Tel.: (00 33) 494 14 20 69. E-mail: vincent.rey@lseet.univ-tln.fr*

Abstract

An instrumented field study of the cross-shore evolution of incident waves was conducted on the shoreface of a gentle sloping microtidal barred-beach (Sète, France). A spectral analysis of typical hydrodynamic conditions (storm, waning storm and fair-weather) was performed from a series of pressure sensor data and synchronized horizontal velocities and pressure data. Results highlight the role of sedimentary bars in the dissipation and the spectral redistribution of incident energy. At the approach of the coast, the bars act like regulators to energy arriving at the shore and non-linear energy

transfers were observed from the gravity to infragravity domain, during breaking or non-breaking situations. Consequently, the ratio of infragravity to gravity wave spectral energy density increases shoreward as significant wave height decreases. The study of wave reflection shows that no reflection was observed over the bars. As the part of reflection on the beachface exits but remained weak except during fair-weather conditions, infragravity waves do not seem to have been generated by reflection during the storms.

1. Introduction

Our knowledge about the complex hydrodynamic processes induced by waves in the surf zone has increased through recent improvements in numerical analysis (i.e. Madsen *et al.*, 1997; Herbers *et al.*, 1999; Cadène, 2000; Battjes & Groenendijk, 2000; Herbers *et al.*, 2003; Yu & Slinn, 2003; Ozkan-Haller & Li, 2003; Van Dongeren *et al.*, 2003) and laboratory studies (O'Hare & Davis, 1993; Greenwood & Xu, 2001; Dulou *et al.*, 2000 and 2002). Due to their possible role in the formation of bars and beach cusps, infragravity waves have been the focus of many theoretical and numerical modelling studies (Hasselmann, 1962; Longuet-Higgins & Stewart, 1964; Elgar & Guza, 1985; List, 1992; Herbers *et al.*, 1995; Herbers *et al.*, 1999; Herbers *et al.*, 2003; Booij *et al.*, 1999). Herbers *et al.* (1994) calculated the energy of the secondary forced surface elevation, while Herbers *et al.* (2000) confirmed the dominant role of triad interaction in

181

the spectral energy balance. Dulou *et al.* (2000, 2002) showed that the formation of nearshore bars seems linked to the first harmonic (the most energetic) spatial modulations due to either partially standing waves or to triad wave-wave non-linear interactions. These wave-wave non-linear interactions increase as water depth decreases. For two free waves of frequencies f_1 and f_2, interactions in the shoaling zone lead to bound harmonics ($2f_1$ and $2f_2$) and to super-harmonics ($f_1 + f_2$). Near and after the break point, transfers occur to low frequencies ($f_1 - f_2$) (Elgar & Guza, 1985; Herbers *et al.*, 1995, Dulou *et al.*, 2000 and 2002). In addition, Van Dongeren *et al.* (2003) note that one frequency may be generated by other combination of frequencies. Despite this progress there remain substantial gaps in our understanding of infragravity wave and gravity wave transformation in natural environments (Holman & Sallenger, 1993). Contrary to the spectral evolution of waves due to shoaling, non-linear wave-wave interaction and dissipation, the reflection of wave energy from natural beaches is rarely measured, although it may be of importance for energy flux calculations. Walton (1992) calculated the wave reflection by use of coincident pressure and velocity measurements and found insignificant reflected wave energy. However, numerous laboratory studies on monochromatic wave reflection from either bottom variations or coastal structures have been carried out (see for instance Guazzelli *et al.*, 1992; Rey *et al.*, 2002 and references cited). Indeed, submerged bars could play a role in beach self-protection through partial wave reflection (Yu & Mei, 2000), which can be significant in the presence of periodic bottom topographical changes at Bragg resonance (Rey *et al.*, 1996). As a consequence, an estimate of wave reflection from either the beachface or the submerged sandy bars may be relevant information for wave spectral evolution in the shoaling, breaking and surf zones.

182

3

The aim of this work is to contribute to the understanding of coastal hydrodynamics in the surf zone for a gentle sloping barred beach in microtidal conditions. As well as spectral analyses to assess wave characteristics and energy transfers, the role of reflection is also investigated. Due to the typically normal swell incidence (maximum of 20°) we focus on the cross-shore swell evolution over two bars along 2 instrumented transects. The bar morphology and impacts of the shoreface on the wave characteristics are presented for typical hydrodynamic conditions (storm, waning storm and fair-weather).

2. Field experiment

2.1. Study area

The studied area is located in the vicinity of Sète, in the Gulf of Lions, Mediterranean Sea, France, in front of the Thau lagoon barrier (fig. 1). This site is part of the National French Program of Coastal Environnement (PNEC- ART 7) studying barred beaches. The majority of swell in the region has mean significant height (H_s) between 0 and 2 m, 30% of the values <1 m, predominantly in summer. The directions are 140-220° N (fig. 1) associated to seabrezze. Only 2% of swells have H_s more than 4 m high, associated with SE to E swell directions, with periods from 5 to 10 seconds. These storms typically last only 24 *hr*. The tide does not exceed 30 *cm* (Akouango, 1997; SHOM, 2003). Nevertheless, higher water level variations are observed in response to set-ups and set-downs under the influence of wind and atmospheric pressure fluctuations. In extreme cases, set-ups can reach 50 *cm* at 450 m from the shore during storms (Akouango, 1997) and 1m near the shore (Certain, 2002) under the added action of breaking waves.

The studied area is 500m wide and extends 700m seawards (fig.2) to 7m depth. Several lines of field evidence and a simple calculation show this depth to be the depth of closure. The backshore consists of an erosive dune. The beach is narrow (20 to 50 m) and subject to erosion. The rate of shore retreat is $1m.y^{-1}$. The sand volume lost in the last ten years is approximately 3400 m^3 (Certain, 2002). The nearshore has a slope of 1% and is composed of a system of bars and troughs (fig. 2). The inner system (inner trough and inner bar), between the shore and the outer trough, is 50 to 150 m wide but

184

5

at times disappears by merging of the inner bar to the beach. The inner bar crest is about 1.5 to 2 m deep, whereas the inner trough is 0.5 m deeper. The outer system (outer trough and outer bar) is positioned between the inner bar and the lower-shoreface. It is generally 250 to 300 m width; the outer trough is about 5 m deep, while the top of the outer bar is 4 m deep. Beyond the outer bar, the lower-shoreface has a gentle slope of 0.85%. Bars are linear and the wave-dominated beach may be classified between intermediate barred and dissipative barred in conformity with the conceptual beach model of Masselink and Short (1993) (see also Short & Aagard, 1993; Gourlay, 1968).

The sandy sediment grain size decreases from 320 μm onshore to 130 μm offshore with coarser sand in the troughs and finer sand over the crests (Certain, 2002). Superimposed on this scheme, Akouango (1997) described a variable grain size distribution depending on wave climate. The beach is characterised by fine sand during fair-weather condition of the summer, but following a short autumnal period of transition the beach becomes coarser grained under the more dynamic winter condition. The finer sediment is transported offshore where conditions are less agitated (Barusseau *et al.*, 1994). As a result, sandstone can be seen in the outer trough and on the lower-shoreface.

2.2. Materials and data availability

The experiment took place between November 3rd and December 3rd 2000 (Certain *et al.*, 2001). Two instrumented cross-shore profiles were deployed to study swell conditions in the entrance of the system and its deformation over the bars (fig. 2):

185

6

(1) Three current meters and wave gauge Interocean S4 DW and ADW (Interocean, 1990) were positioned on the lower-shoreface, in the outer and inner troughs (fig. 2) respectively to –6,0, -4,0 and –2,5 m depth. The instruments were programmed to record for 18 or 36 minutes every three hours at a 2 Hz frequency. Fixed on non-magnetic structures, they measured the two horizontal current components at a distance of 0.9 m from the seabed. After each sampling period, the two horizontal current components were averaged and stored in the instrument. Recorded pressures were recorded at a ground distance of 0.8 m.

(2) A pressure sensor array was positioned on the inner bar crest, parallel to the first profile at a distance of 100 m (fig. 2). It was composed of a series of 5 synchronous Hitec Inc. pressure sensors in the cross-shore direction on the inner bar crest on a ballasted cable (fig. 2). Note that sensors don't provide information about the wave directional field. The pressure is converted into an electric signal collected in real time by use of electric cables. The data acquisition system (power supply, converters and computer) is located on the shore. The distances $\Delta x_i = x_i - x_1$ between the more offshore sensor labelled 1 and the sensor labelled i where respectively $\Delta x_1 = 0$m, $\Delta x_2 = 9.5$m, $\Delta x_3 = 19$m, $\Delta x_4 = 27.4$m, $\Delta x_5 = 38$m. The pressure sensors were calibrated for a full scale of 10m in hydrostatic conditions. The sensors were displayed on the bottom in water depths of about 2m. The sampling frequency was 16 Hz and the pressure accuracy in terms of water height was about 1 cm. Records were collected by monitoring from the shore and could cover long measurement periods.

186

3. Data analysis

Raw data were stored and spectral analysis was used to assess wave characteristics, assuming the sea state to be represented by a superimposition of Airy waves (linear approximation). Spectra based on progressive waves may be calculated either through velocity or pressure measurements for the S4 instruments. Comparison of results with those obtained for the incident wave, assuming partially standing waves, may give additional information on the applicability of both methods. While pressure and velocity data give similar spectra in intermediate water, differences are observed in very shallow waters, as shown in figure 3, where calculations assuming either progressive waves, or partially standing waves are made. Since in shallow water, hydrostatic flow can be assumed despite wave nonlinearities, we chose to use the pressure data for the spectral analysis of progressive waves. Pressure measurements were converted to water elevations (Horikawa, 1988) which leads to a necessary cut off imposed at 0.25Hz. A 540s Hanning window with 50% overlap was used for power spectrum and cross-spectrum as proposed by Welch (1967). A linear de-trend replaced the truncated degrees of freedom, hence increasing the reliability of the results. The limit between gravity and infragravity waves domain depends on the incident wave frequency. In short period fetch limited environments this limit may be reasonably fixed at 0.05Hz (Bauer, 1990; Sénéchal, 2001). The lower limit for infragravity waves was fixed at 0.004Hz. Correction relative to atmospheric pressure is not necessary as pressure sensors measure it directly.

187

8

Since classic techniques were used for progressive waves (see for instance Rodriguez *et al.*, 1999), in this section we focus on the algorithms for partially standing waves calculations by use of coincident pressure and horizontal velocity measurements. In the nearshore, we can expect waves to be partially reflected. On this basis, the surface elevation for the wave component of angular frequency $\omega = 2\pi f$ takes the form:

$$\eta(x, y, t) = [a_i \cos(\omega t - k \cos \theta_i x - k \sin \theta_i y + \varphi_i) \qquad (1)$$
$$+ a_r \cos(\omega t - k \cos \theta_r x - k \sin \theta_r y + \varphi_r)]$$

where $\vec{k}$ (k cos θ; k sin θ) is the wavenumber, a and φ are respectively amplitudes and phases, θ is the angle with respect to *x*-axis and the indices *i* and *r* denote respectively the incident and reflected waves.

An assumption must be made for the angle of obliquely incident partially standing waves and reflected waves measured from a single synchronized horizontal velocity and pressure data (see for instance Walton, 1992; Drevard *et al.*, 2003). Walton (1992) assumed a wave incidence angle θ with respect to the beach cross-shore direction, the angle between the wave directions being $\pi - 2\theta$. In the present study for which quasi-normal swell waves were observed, we assumed both incident and reflected waves to be in the same direction but in opposite directions of motions ($\theta_i = \theta$ and $\theta_r = \theta_i + \pi$). No information about beach direction is then required for the energy calculations, although the incident wave direction for each frequency component was given by:

$$\theta = atan \frac{|v|}{|u|} \text{ if } |u| \neq 0 \text{ and } \theta = \frac{\pi}{2} \text{ if } |u| = 0 \qquad (2)$$

For simplicity, we then assume motion in the xOz plane, where the z-axis is oriented upwards, and the x-axis is the direction of propagation. Using complex notations, the velocity potential for a wave of angular frequency ω, propagating in the x-axis may be expressed as:

$$\Phi(x, z, t) = \Phi_i(x, z, t) + \Phi_r(x, z, t) = \frac{a_i\omega}{k} C(z)e^{i(\omega t - kx)} + \frac{a_r\omega}{k} C(z)e^{i(\omega t - kx)} \tag{3}$$

where h is the water depth and $C(z) = \omega \dfrac{\cosh[k(z+h)]}{\sinh(kh)}$. This corresponds to a free surface deformation:

$$\eta(x, t) = \eta_i(x, t) + \eta_r(x, t) = -ia_i e^{i(\omega t - kx)} - ia_r e^{i(\omega t - kx)} \tag{4}$$

where $H = 2a$ is the crest to through amplitude. The wavenumber k is consistent with the dispersion relation

$$\omega^2 = gk \tanh(kh) \tag{5}$$

where g is gravity. Horizontal velocity and pressure at depth z are then given by

$$u = C(z)\,(\eta_i - \eta_r) \tag{6}$$

$$p + \rho g z = \frac{\rho\omega}{k} C(z)\,(\eta_i + \eta_r) \tag{7}$$

Writting $u^{(m)} = |u|\, e^{i\varphi u}$ and $p^{(m)} = |p|\, e^{i\varphi p}$, where exponent (m) denotes the measured values, we obtain

10

189

$$a_i = \frac{1}{2C(z)}\left[|u|^2 + \frac{k^2\ |p|^2}{\rho^2\omega^2} + \frac{2|u|\ |p|\ k}{\rho\omega}\cos(\varphi_p - \varphi_u)\right]^{\frac{1}{2}} \qquad (8)$$

$$a_r = \frac{1}{2C(z)}\left[|u|^2 + \frac{k^2\ |p|^2}{\rho^2\omega^2} - \frac{2|u|\ |p|\ k}{\rho\omega}\cos(\varphi_p - \varphi_u)\right]^{\frac{1}{2}} \qquad (9)$$

The rate R of reflected energy is then given by

$$R(f) = \frac{a_r^2}{a_i^2} \qquad (10)$$

Let us note that if $a_i < a_r$, the direction θ_2 may correspond either to the incident wave if only linear processes are concerned, or to a wave component generated in shallow waters and propagating offshore. For progressive waves, this method overcomes the uncertainty π in the direction when classical analyses are done.

4. Experimental results

4.1. Hydrodynamics conditions

The meteorological and hydrodynamic conditions during the field experiment are presented in figure 4 for each three S4 measurement point: lower-shoreface, outer trough and inner trough. Wave characteristics and general spectral variables are listed in Table 1. During the survey from November 1st to December 1st, four storms occurred on November 6th, November 12th, November 23rd and November 30th as indicated by the large significant heights of the swell recorded (fig. 4e). On the lower-shoreface, the first three storms had similar significant heights (2.7 to 3 m); the fourth storm had smaller

wave height (2 m). In the outer trough, the significant heights were similar (around 1.8 m) for all storms after a first breaking on the outer bar. In the inner trough, landward of a second breaking over the inner bar crest, wave heights were very similar, between 0.7 and 1 m. Peak periods recorded for these storms (fig. 4d) were between 10s for the first and 7.7s for the second (table 1). Wave directions (fig. 4c) were shore normal (150-160°N) and winds were blowing from SE with peaks of 8 m.s^{-1} (fig. 4a-b). On November 17th high wind velocity were from 305° direction. These strong offshore winds did not create any waves on the coast.

In the following part, we described successively storm, storm waning and fair-weather conditions.

4.2. Storm conditions

Figure 5 represents the cross-shore spectral density evolution for each of the four storm peaks (fig. 4 and table 1) from the lower-shoreface towards the outer and inner trough. The first two storms were the most energetic with wave height at 3.1 and 2.7 m and spectral energy density of 21 and 21.7 m^2.Hz^{-1} for the first harmonic on the lower-shoreface. The third and fourth storms presented moderate conditions (respectively 7.4 and 7.3 m^2.Hz^{-1} for the first harmonic). Landward of the outer bar after breaking, the first harmonic energy was found relatively reduced for each storm (noted T$_n$) (T1 = 3.6 m^2.Hz^{-1}, T2 = 10.7 m^2.Hz^{-1}, T3 = 3.9 m^2.Hz^{-1} and T4 = 5.1 m^2.Hz^{-1}). In the inner trough, the spectral energy density for the first harmonic was similar in the inner trough around 1 m^2.Hz^{-1} (T1 = 1.8 m^2.Hz^{-1}, T2 = 1.2 m^2.Hz^{-1}, T3 = 0.9 m^2.Hz^{-1} and T4 = 0.9 m^2.Hz^{-1}). This can be attributed to the filtering effect of the bars (Guza & Thornton, 1982).

In low frequency domain, cross-shore variations were more complex. The peak of spectral energy density for the secondary harmonic during the first storm was 1.1 $m^2.Hz^{-1}$ (table 1). The subsequent storms had weaker peaks (T2 = 0.3 $m^2.Hz^{-1}$, T3 = 0.2 $m^2.Hz^{-1}$ and T4 = 0.3 $m^2.Hz^{-1}$). This is also shown when examining the integral of the infragravity domain instead of the peak (T1= 9.6 $m^2.Hz^{-1}$, T2=2.7 $m^2.Hz^{-1}$, T3= 1.6 $m^2.Hz^{-1}$ et T4= 1.9 $m^2.Hz^{-1}$). The infragravity energy has the same order of magnitude along the cross-shore section (i.e. 0.3 $m^2.Hz^{-1}$ in the lower-shoreface and 0.18$m^2.Hz^{-1}$ in the inner trough during the second storm) whereas the first harmonic decreases. However, the highest infragravity energy during the last 3 storms was encountered in the outer trough and then decreased shoreward (i.e. during the second storm 0.3 $m^2.Hz^{-1}$ in the lower-shoreface, 0.6 $m^2.Hz^{-1}$ in the outer trough and 0.18 $m^2.Hz^{-1}$ in the inner trough). For the first storm, infragravity spectral energy density decreased gradually from the lower-shoreface to the shore. The ratio of the infragravity to gravity wave spectral energy density was calculated (table 1). This ratio was 1.1% to 3% on the lower shoreface, higher in the outer trough (2.9 to 7.8%) and increased to a maximum in the inner trough (7.9 to 20%). This shoreward increase seems to increase by a factor of 2.6 between each compartment. This suggests that energy is being transferred from the first harmonic to the subharmonics.

Figure 6 displays the cross-shore evolution of the sea-surface elevation energy density spectra computed during the third storm at the landward and seaward stations of the sensors line. Energy loss due to wave breaking over the inner bar is well observed, spectral energy density of the first harmonic diminishing brutally (fig. 6). The position

192

13

of wave breaking tends to be focused on the seaward slope of the inner bar. As for the S4 analysis, during agitated events we observed an increase of the amount of infragravity wave energy shoreward compared to the amount of gravity wave energy. Even if this tendency is not clearly visible on figure 6, it can be easily followed using adimensional spectrum (fig.7). Figure 7 illustrates adimensional spectrum evolution for the 5 sensors over the inner bar. The part of the infragravity energy increases onshore, showing non-linear interactions on the sensors and energy redistributed in the frequency band.

The reflected energy during storm conditions was very weak with respect to incident energy. This ratio increased from 2.5-2.8 % on the lower-shoreface, 3.4-6.9 % in the outer trough to 5.5 -12.2 % in the inner trough (Table 1).

4.3. Storm waning condition

At the end of the first storm (situation 1 on table 1, fig. 8.1), the significant wave height was 0.5 m on the lower-shoreface (fig. 4e). The spectral energy of the first harmonic during this waning condition was 10 to 20 times weaker (0.8 $m^2.Hz^{-1}$) than for storm conditions (i.e. 21 $m^2.Hz^{-1}$ for storm 1). Several principal harmonics were observed on the lower-shoreface and the outer trough (0.133 Hz and 0.10 Hz). No wave height transformation was observed in the outer trough (table 1), as no breaking occurred over the outer bar. However, a strong decrease in the spectral energy of the first harmonics was observed in the inner trough (0.29 $m^2.Hz^{-1}$) indicating wave breaking on the inner bar (table 1). The spectral energy density of the infragravity peak was weak (0.028 to

193

14

0.05 m^2.Hz^{-1}) and increased slightly shoreward. The ratio of infragravity to gravity wave spectral energy density was also observed to increase from the lower shoreface (2.6%) toward the coast (3.8% in the outer trough and 8.7% in the inner trough). The frequency range of the second harmonic peak (0.03 Hz) corresponds to the difference in frequency between the two principal free peaks on the lower shoreface.

At the end of the third storm (situation 2: table 1 and fig. 8-2), significant wave height was 1.65 m (fig. 4e). No breaking and no cross-shore attenuation were observed over the outer bar. A strong decrease in the spectral energy density of the first harmonic from the outer trough (11.3 m^2.Hz^{-1} with Hs at 1.54 m) to the inner trough (1.25 m^2.Hz^{-1}with Hs at 0.89 m) suggests wave breaking on the inner bar. The ratio of infragravity to gravity wave spectral energy density was 2.1% on the lower shoreface and increased shoreward with 2.5% in the outer trough and 11% in the inner trough. Two principal harmonics were observed on the lower-shoreface spectra (0.12 Hz and 0.15 Hz). The infragravity peak generated by difference-frequency generation of two principal free peaks was found at 0.3 Hz.

As for the storm conditions, the reflected energy remained very weak, i.e. between 2.8 to 2.9 % on the lower-shoreface for both situations, 3.2 to 6.9 % in the outer trough and 5.5 to 6.0 % in the inner trough (Table 1).

4.4. Fair-weather condition

Fair-weather conditions (Table 1 and fig. 8-3) were characterised by small non-breaking, long period swell (H_s= 0.2 m T=12 s) (fig. 4e); the infragravity energy was weak but the ratio of infragravity to gravity wave spectral energy density increased toward a maximum on the shore (18.9 % on the lower-shoreface, 19.7 % in the outer trough and 26.4 % in the inner trough). This is manifested by a widening of the principal peak (0.084 Hz) over the outer bar (without breaking). The principal harmonic, which developed into two peaks (0.081 and 0.096 Hz) in the outer trough, was related to the peak of the infragravity at 0.013 Hz (difference-frequency generation) and to the two subharmonic peaks at 0.039 Hz and 0.05 Hz. This suggests that there was a transfer of energy between the first harmonic and its subharmonics.

The effect of the shoaling on the spectral energy on the inner bar was well observed on the sensor line data presented in fig. 9. The incident wave propagates towards the beach and its amplitude increases, while energy redistribution is observed.

The reflected energy is quite significant (about 30%), and does not vary significantly from the outer through to offshore (table 1 and fig. 10). Since it is slightly higher in the inner trough (about 45%), we can conclude that reflection is due to the beachface rather than to the bars.

195

16

5. Discussion

The results show the paramount role of the bars for waves propagating through a wide range of water depths over sloping beds of movable sediments. The passage of a wave train from offshore to shallow water involves modifications to the energy spectrum. This energy was relatively broad but appeared to be centred on harmonic frequencies (Elgar *et al.,* 1997, Norheim *et al.,* 1997). Non-linear triad interactions were strong which lead to significant energy transfer, in particular towards the subharmonics by difference-frequency generation between the free harmonics. Masselink (1998) observed decomposition of incident swell into high frequency waves across a one barred –profile with the main implication of wave period decrease. In our study the harmonic transfer occurred mainly into low frequencies, and no period modification was apparent. The ratio of infragravity to gravity wave spectral energy density increased shoreward. The maximum of induced infragravity energy occurred at the coast, in accordance with theory and past observations (Guza & Thornton, 1983; Aagard & Greenwood, 1995; Masselink & Hegge, 1995). Furthermore, the maximum of infragravity energy was not observed during the storm maximum but later, when the significant height decreased.

Breaking on the shoreface was predominated by wave plunging on the outer bar with a second breakpoint located on the inner bar. When wave breaking occurred (waning storm -situations 1 and 2- and storm), the modification of wave spectrum shape was most marked. Even for slight breaking (situations 1 and 2), transfer towards the subharmonics was visible. The energy of the infragravity oscillations is closely related

196

17

to the energy of the incident waves in the surf zone. The breaking swell transferred additional energy to the infragravity band. These results are consistent with those obtained by Russell (1993) and Masselink & Hegge (1995). Ruessink (1998) also shows that wave breaking is associated with a rapid increase in the contribution of free infragravity energy to the total infragravity field.

The sensor line data for the inner bar show that the position of wave breaking tends to be focused on the seaward slope bar. Battjes (1974) suggests wave breaking is initiated when the ratio of wave height to depth exceeds a threshold of $\gamma= 0.8$. However, results from the present study are similar to the observations of Kroon (1994) and Sénéchal *et al*. (2002) ($\gamma= 0.4$). In both cases, the authors revealed the presence of a large amount of infragravity wave energy. After reflection at the shoreline, the released waves propagate in a seaward direction and may either escape into deep water or remain trapped by refraction to the shore. Ruessink (1998) also noted that the free infragravity energy might also be generated in the absence of breaking waves.

Considering the significant heights or the spectral energy density, we noticed that they were about the same order of magnitude for each storm in the outer and inner troughs. Wave heights or wave energy on the lower-shoreface were not determinative of the wave characteristics in the outer trough. They were always of the same height and the first harmonic had about the same level of energy after breaking on the outer bar. The bars act like regulators or transformers of energy. In the case of the first storm, the energy was three times stronger than the fourth storm on the lower-shoreface. However, the height or spectral energy density values of both cases were identical in the outer trough. During the first storm the energy was transformed and a strong attenuation was

197

18

measured between the lower-shoreface and the outer trough. In the other case, the spectral energy density remained quite the same after the bar over-stepping. The same schema is reproducible on the inner bar. Bars regulate the incoming energy arriving at the beach. This filtering effect was also described by (Guza & Thornton, 1982).

Wave reflection from natural beaches and man-made coastal structures influences the hydrodynamics and the sediment transport in front of a reflector. It is then desirable to separate wave train into incident and reflected waves. Some authors had shown the role played by irregular topography on reflection. Recently several authors developed a method for estimating reflection over a sloping beach (i.e. Chang & Hsu, 2003) and varying topography considering also evanescent modes in the case of abrupt water depth change (i.e. Cho *et al.,* 2004). Yu and Mei (2000) showed that artificial longshore bars in front of a beach can provide protection from incident waves, but in certain situations may worsen erosion. They state that the mechanism is essentially a bar-mediated transfer of energy between incident and reflected wave. It was reasonable to expect that reflection might be weak during fair-weather and strong during storm due to the presence of bars and then could contribute in infragravity wave generation. However our results shown that the positions of bars did not affect this process, and no reflection was observed over bars. As reflection was strongest in the inner trough, it can be argued that reflection was produced by the beachfront and not by the bars. Except for fair-weather conditions, it seems that reflection is a minor phenomenon. This confirms that energy was being transferred from the first harmonic to the subharmonics. It also confirms and validates our methodology on progressive waves and moreover on amplitude calculation.

6. Conclusion

An instrumented field study of the cross-shore evolution of incident waves was conducted on the shoreface of a gentle sloping microtidal barred-beach (Sète, France). Spectral analyses were used to characterize dissipation, redistribution and energy transfers from gravity to infragravity field. The role of bars is important in the spectral redistribution of the swell energy at the approach of the coast. When waves cross the bars, non-linear energy transfers occur between the gravity and infragravity domains, whether breaking occurs or not. In the dissipation of energy, the bars act like regulators to energy arriving at the shore. Whatever storm magnitude on the lower-shoreface, the wave height or wave energy in the outer trough or in the inner trough is the same after breaking on the outer bar or the inner bar. Infragravity energy during storms increases from the lower-shoreface to the outer trough and then decreases towards the coast. For weaker agitations, infragravity energy increases towards the coast. In all cases, the ratio of infragravity to gravity wave spectral energy density increases shoreward as significant wave height decreases. Significant reflection is observed on the beachface for calm conditions, however we could expect the bars to play a much more significant role in shore protection through wave energy reflection by topographical changes. This was not however observed during the storms.

199

20

Figures captions

Figure 1 : Location of the study zone, Sète, Gulf of Lions, France.

Figure 2: Subtidal morphology of the beach with the bar and trough system (cross section profile) and position of the instrumental deployment (S4 in the troughs and on the lower-shoreface, and pressure sensors profile on the inner bar).

Figure 3: Spectral energy density from both pressure sensor data (dotted line) and horizontal velocity data (plain line) on the lower-shoreface (1) and in the inner trough (2) during storm 3 (*cf. 4.1 hydrodynamics conditions*).

Figure 4: Meteorological and general hydrodynamic conditions encountered during the measurement experimentation. (a) Wind velocity are in $m.s^{-1}$ and (b) direction are in north referenced degrees. (c) Hs; (d) Tp and (e) wave direction are presented for S4 instruments on the lower shoreface (plain line), in the outer trough (dotted line) and in the inner trough (long dash). Situations analysed are here shaded in gray.

Figure 5: Sea-surface elevation spectra for each storm peak. (1) 6 November; (2) 12 November; (3) 23 November; (4) 30 November. The lower shoreface is in plain line; the outer trough in dotted line and the inner trough in long dash. Data are here expressed in adimensional spectral density, see table 1 for spectral energy density values ($m^2.Hz^{-1}$).

Figure 6: Observed sea-surface elevation spectral energy density for the third storm (23 November) at the sensor line. Dotted line represents the outer sensor and plain line represents the inner sensor.

Figure 7: Adimensional spectral energy density for storm case (the third storm, 23 November) for the 5 sensors over the inner bar. (1) is the outer sensor and (5) is the inner sensor (fig. 1).

Figure 8: Sea-surface elevation spectrum for storm waning condition on (1) 7 November and (2) 23 November and for fair-weather conditions on (3) 18 November. The lower shoreface is plain line, the outer trough in dotted line and the inner trough in long dash.

Figure 9: Observed sea-surface spectral energy density for fair-weather case for the sensors line over the inner bar. Dotted line represents the outer sensor and plain line represents the inner sensor.

Figure 10: Sea-surface elevation spectrum ($m^2.Hz^{-1}$) in the inner trough (1), in the outer trough (2) and on the lower-shoreface (3) for incident (plain line) and reflected (dotted line) waves in fair-weather condition.

Table Captions

Table 1: The different types of hydrodynamic conditions encountered and analysed on the Sète site and principal results obtained from the analysis of the energy spectra (Hs, T, First harmonic (Fh) spectral energy density (SED), infragravity peak SED, total infragravity SED and first harmonic SED versus infragravity SED).

References

Aagard and Grenwood, 1995. Suspended sediment transport and morphological response on a dissipative beach. *Continental Shelf Research*, 15, 1061-1086.

Akouango, E., 1997. *Morphodynamique et dynamique sédimentaire dans le Golfe du Lion. Contribution à l'étude de la zone côtière dans l'actuel et le Quaternaire récent.* Unpublished thesis, Univ. de Perpignan, 200 p.

Barusseau, J.P., Descamps, C., Radulescu, M., Akouango, E., & Gerbe, A., 1994. Morphosedimentary multiyear changes on a barred coast (Gulf of Lions, Mediterranean Sea, France). *Marine Geology*, 122, 47-62.

Battjes, J. A. (1974). *Surf similarity.* Proc 14th International Coastal Engineering Conference.

Battjes, J. A. and Groenendijk, H. W., 2000. Wave height distributions on shallow foreshores. *Coastal Engineering* 40 (3), 161-182.

Bauer, B.O., 1990. Assessing the relative energetics of infragravity motions in lakes and seas. *Journal of Coastal Research*, 6, 853-865.

Booij, N., Ris, C. and Holthuijsen, L. H., 1999. A third-generation wave model for coastal regions. 1. Model description and validation. *Journal of Geophysical Research* 104(C4): 7649-7666.

Cadène, A-L., 2000. *Dynamique des ondes infragravitaires générées par la houle en zone littorale.* Unpublished thesis, Institut national polytechnique de Toulouse, 239 p.

Certain, R., 2002. *Morphodynamique d'une côte sableuse microtidale à barres : le golfe du Lion (Languedoc – Roussillon).* Unpublished thesis, Univ. Perpignan, 209 p., ann.

Certain, R., Barusseau, J. P., Capobianco, R., Meuret, A., Rey, V., Dulou, C., Stepanian, A., Levoy, F. and Howa, H, 2001. Bottom and shoreline evolutions under wave actions at a french Mediterranean site : The beach of Sète. *MEDCOAST01, The fifth International Conference on the Mediterraneen Coastal Environment, 23-27 October 2001, Hamammet, Tunisia*

Chang, H.-K. and T.-W. Hsu (2003). A two-point method for estimating wave reflection over a sloping beach. *Ocean Engineering* 30: 1833-1847.

Cho, Y.-S., Jeong, W.-C., Woo, S.-B., 2004. Finite element method for strong reflection of water waves. *Ocean Engineering* 31(5-6): 653-667.

Drevard, D., Meuret, A., Rey, V., Piazzola, J. and Dolle, A., 2003. Partially reflected waves measurements using Acoustic Doppler Velocimeter (ADV), *Thirteenth*

International Onshore and Polar Engineering Conference ISOPE'03, Honolulu, Hawaii, 25-31 may 2003.

Dulou, C., Belzons, M and Rey, V., 2002. Bar formation under breaking wave conditions: A Laboratory study, *J. Coastal. Res.*, 18 (4), 802-809.

Dulou, C., M. Belzons, and V. Rey, 2000. Laboratory study of wave bottom interaction in the bar formation on an erodible sloping bed. *J. Geophys. Res.*, 105(C8), 19745-19761.

Elgar, S. and Guza, R.T., 1985. Observations of bispectra of shoaling surface gravity waves. *J. Fluid. Mech.* 161, 425-448.

Elgar, S., Guza, R.T., Raubeiheimer, B., Herbers, T.H.C and Gallagher, E.L., 1997. Spectral evolution of shoaling and breaking waves on a barred beach. *J. Geophys. Res.*, 102, 15797-15805.

Gourlay, M.R., 1968. *Beach and dune erosion tests*. Deflt Hydraulics Laboratory, report n°M935/M936.

Greenwood, B. and Xu, Z., 2001. Size fractionation by suspension transport: a large scale flume experiment with shoaling waves. *Marine Geology* 176: 157-174.

205

Guazzelli, E., Rey, V., and Belzons, M. 1992 Higher-order Bragg reflection of gravity surface waves by periodic beds. *J. Fluid Mech.* 245, 301-317.

Guza, R.T., and Thorton, E.B.,1982. Swash oscillations on a natural beach. *J. of Geophys. Research*, 87, 483-491.

Hasselmann, K., 1962. On the non-linear energy transfer in gravity wave spectrum. *I.J. Fluid. Mech. 12*, 481-500.

Herbers, T. H. C., Elgar, S. and Guza, R. T. (1994). Infragravity-frequency (0.005-0.05 Hz) motions on the shelf: I. Forced waves. *Journal of Physical Oceanography* 24: 917-927.

Herbers, T. H. C., Elgar, S., and Guza, R. T. (1995). "Generation and propagation of surf beat," *Journal of Geophysical Research* 100 (C12), 24,863-24,872.

Herbers, T. H. C., Elgar, S. and Guza, R. T., 1999. Directional spreading of waves in the nearshore. *Journal of Geophysical Research* 104(C4): 7683-7693.

Herbers, T. H. C., Russnogle, N. R. and Elgar, S. (2000). Spectral energy balance of breaking waves within the surf zone. *Journal of Physical Oceanography* 30: 3723-2737.

Herbers, T. H. C., Orzech, M., Elgar, S. and Guza, R. T., 2003. Shoaling transformation of wave frequency-directional spectra. *Journal of Geophysical Research* 108(C1, 3013): doi:10.1029/2001JC001304, 1-17.

Holman, R.A. and Sallenger, A.H., 1993. Sand bar generation: a discussion of the Duck experiment series. *Journal of Coastal research*, vol. 87, N°. C1.

Horikawa, K., 1988. Nearshore dynamics and coastal processes: theory, measurement and pedictive models. Tokyo, University of Tokyo Press:1-522

INTEROCEAN, 1990. S4 current meter; user's manual, 3rd eds., 90 p.

Kroon, A., 1994. *Sediment transport and morphodynamics of the beach and nearshore zone, near Egmond, The Netherlands.* Faculteit Ruimtelijke Wetenschappen, Universiteit Utrecht: 1-274.

List, J.H., 1992. A model for the generation of two-dimensional surf beat. *J. Geophys. Res.* 97-C7, 5623-5635.

Longuet-Higgins, M.S. & Stewart, R.W., 1964. Radiation stresses in water waves ; a physical discussion, with application. *Deep-Sea Research*, 11, 529-562.

Madsen P.A., Sørensen O.R. and Schäffer H.A, 1997. Surf zone dynamics simulated by a Boussinesq type model. Part I. Model description and cross-shore motion of regular waves, *Coastal Engineering*, Vol 32, pp 255-287.

Masselink, G., 1998. Field investigation of wave propagation over a bar and the consequent generation of secondary waves. *Coastal Engineering* 33: 1-9.

Masselink, G., and Hegge, B., 1995. Morphodynamics of meso-macrotidal beach from central Qeensland, Australia. *Marine Geology*, 129, 1-23.

Masselink, G. and A. D. Short, 1993. The effect of tide range on beach morphodynamics: a conceptual model. *Journal of Coastal Research* 9: 785-800.

Norheim, C.A.; Herbers, T.H., and Elgar, S., 1997. Nonlinear evolution of surface wave spectra on a beach. *Journal of Physical Oceanography*, 28, 1534-1551.

O'Hare, T.J. and Davis, A.G., 1993. Sand bar formation beneath partially standing waves: laboratory experiment and model simulation. *Cont. Shelf Res.*, 13, pp 1149-1181.

Ozkan-Haller, H. T. and Li, Y., 2003. Effects of wave-current interaction on shear instabilities of longshore currents. *Journal of Geophysical Research* 108(C5, 3139): doi: 10.1029/2001JC001287: 1-19.

Rey, V. , Capobianco, R. and Dulou, C. 2002. Wave scattering by a submerged plate in presence of a steady uniform current, *Coastal Engineering*, 47, 27-34.

Rey, V., Guazzelli, E. and Mei, C. C. 1996. Resonant reflection of surface gravity waves by one-dimensional doubly sinusoidal beds, *Physics of Fluids.* 8 (6), 1525-1530.

Rodriguez, G., Guedes Soares, C. and Machado U., 1999: Uncertainty of the sea state parameters resulting from the methods of spectral estimation, *Ocean Engineering*, 26, 991-1002.

Ruessink, B. G., 1998. The temporal and spatial variability of infragravity energy in a barred nearshore zone. *Continental Shelf Research* 18 (6): 585-605.

Russell, P.E., 1993. Mechanisms for beach erosion during storms. *Continental Shelf Research*, 13, 1243-1265.

S.H.O.M., 2003. Tide Tables, tome1, French harbors. Edition 2003.

Sénéchal, N., Bonneton, P., Dupuis, H., 2002. Field experiment on secondary wave generation on a barred beach and the consequent evolution of energy dissipation on the beach face. *Coastal Engineering*, 46, 223-247.

Sénéchal, N., Dupuis, H., Bonneton, P., Howa, H., Pedreros, R., 2001. Observation of irregular wave transformation in the surf zone over a gently sloping sandy beach on the French Atlantic coastline. *Oceanologica Acta*, 24, 545-556.

Short, A.D. et Aagaard, T., 1993. Single and multi-bar beach change models. *Journal of Coastal Research*, Special Issue 15, 141-157.

Van Dongeren, A., Reniers, A. J. H. M., Battjes, J. A. and Svendsen, I., 2003. Numerical modeling of infragravity wave response during DELILAH. *Journal of Geophysical Research* 108(C9): doi: 10.1029/2002JC001332,2003.

Walton Jr, T., L., 1992: Wave reflection from natural beaches, *Ocean Engineering*, 19, (3), 239-258.

Welch, P., D., 1967: The use of Fast Fourier Transform for the estimation of power spectra: a method based on time averaging over short modified periodograms. *IEEE TRans. on Audio and Electro-acoustics*, 15, 338-341.

Yu, J. and Mei, C. C., 2000. Do longshore bars shelter the shore?. *Journal of Fluid Mech.* 404, 251-268.

Yu, J. and Slinn, D. N., 2003. Effects of wave-current interaction on rip-currents. *Journal of Geophysical Research* 108(3088): doi:10.1029/2001JC001105.
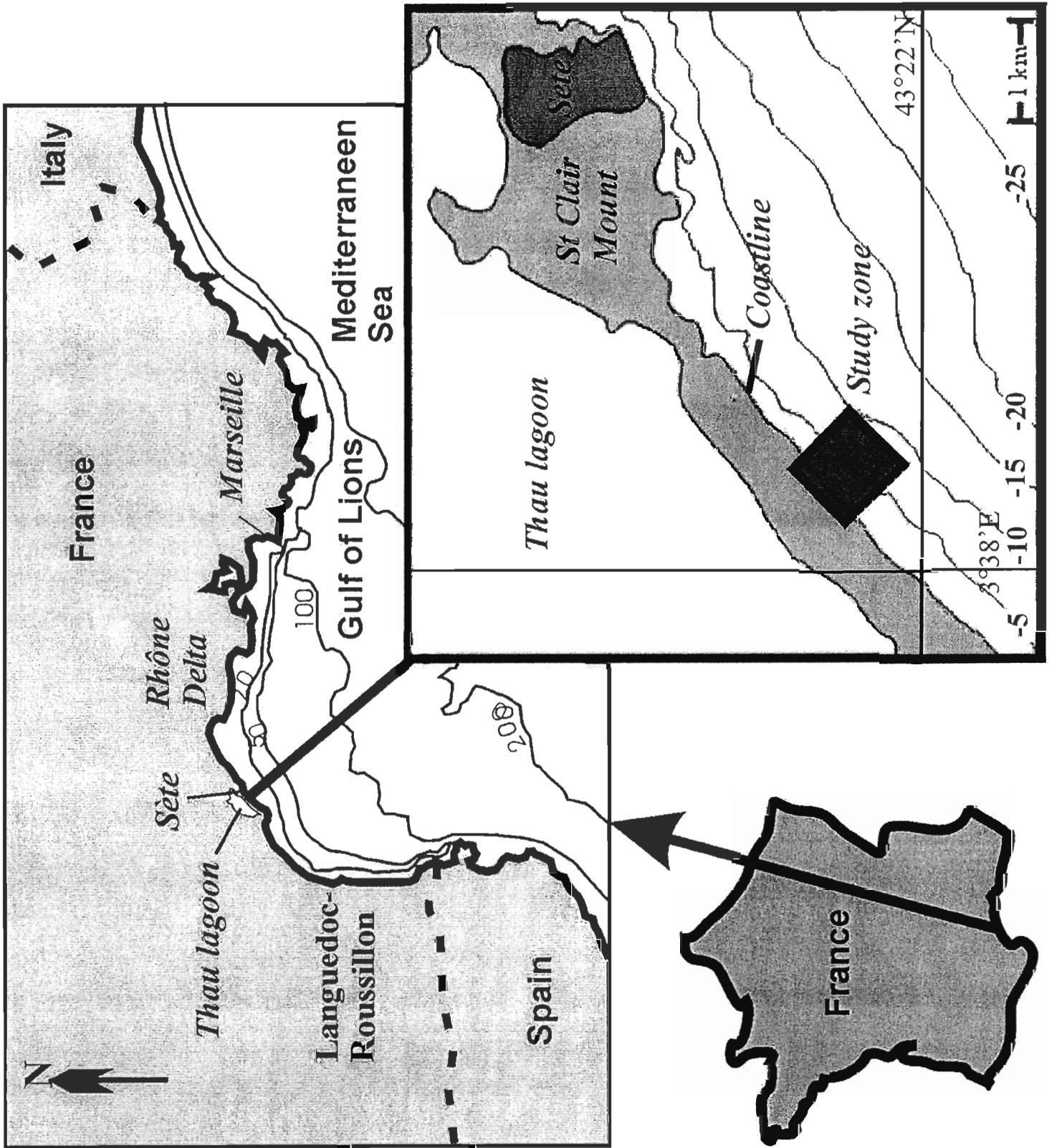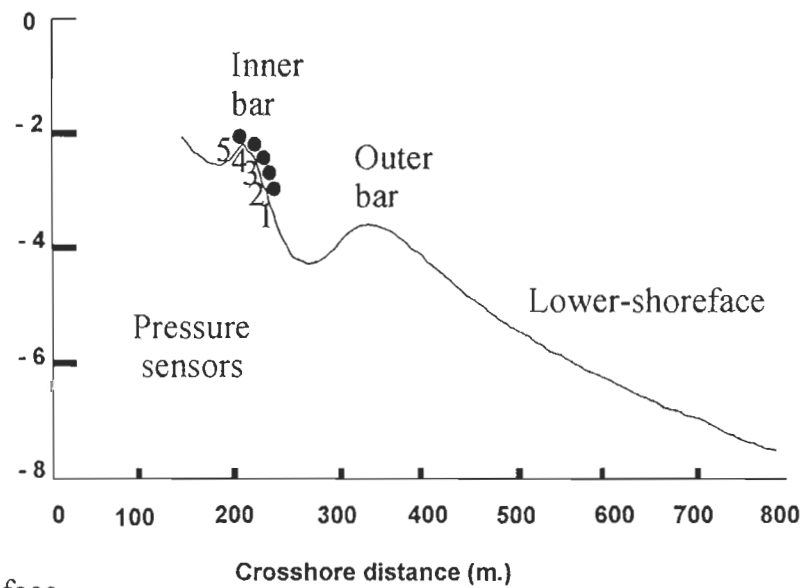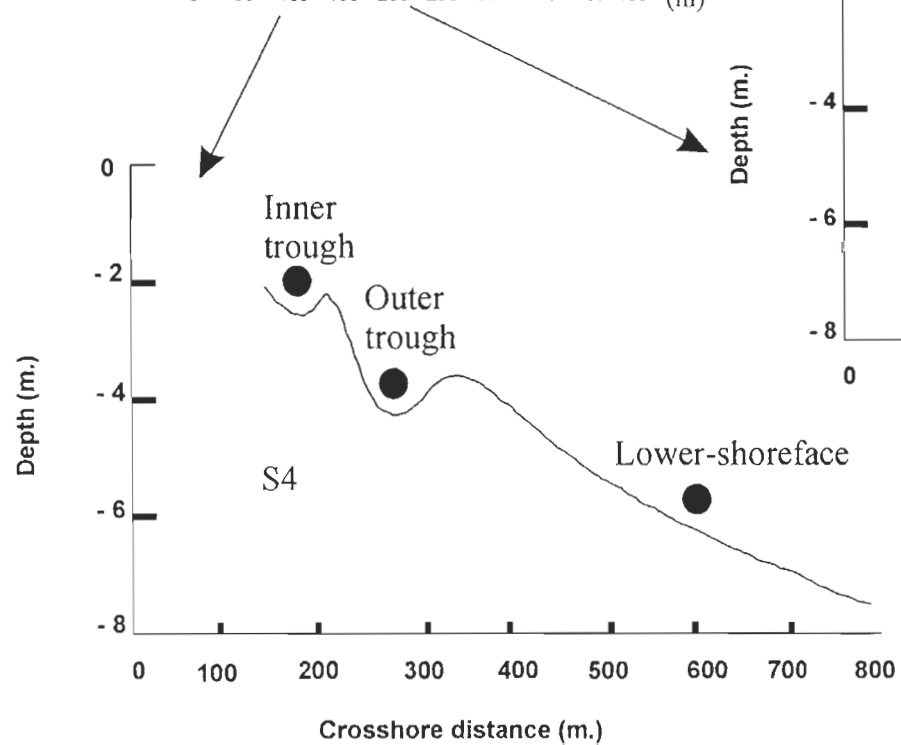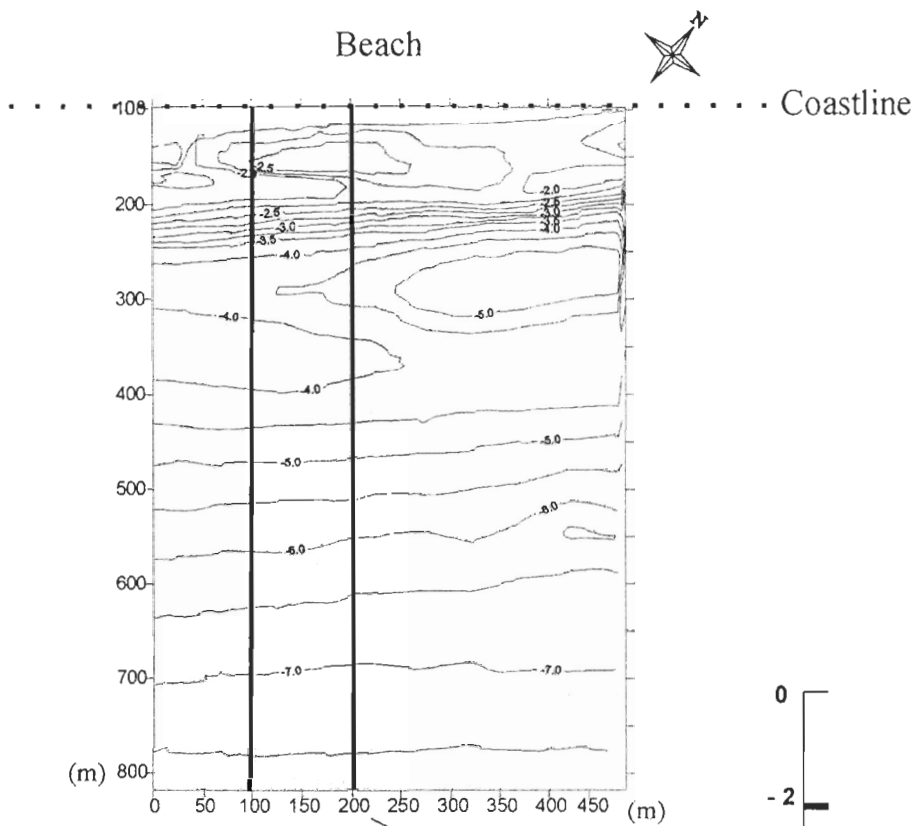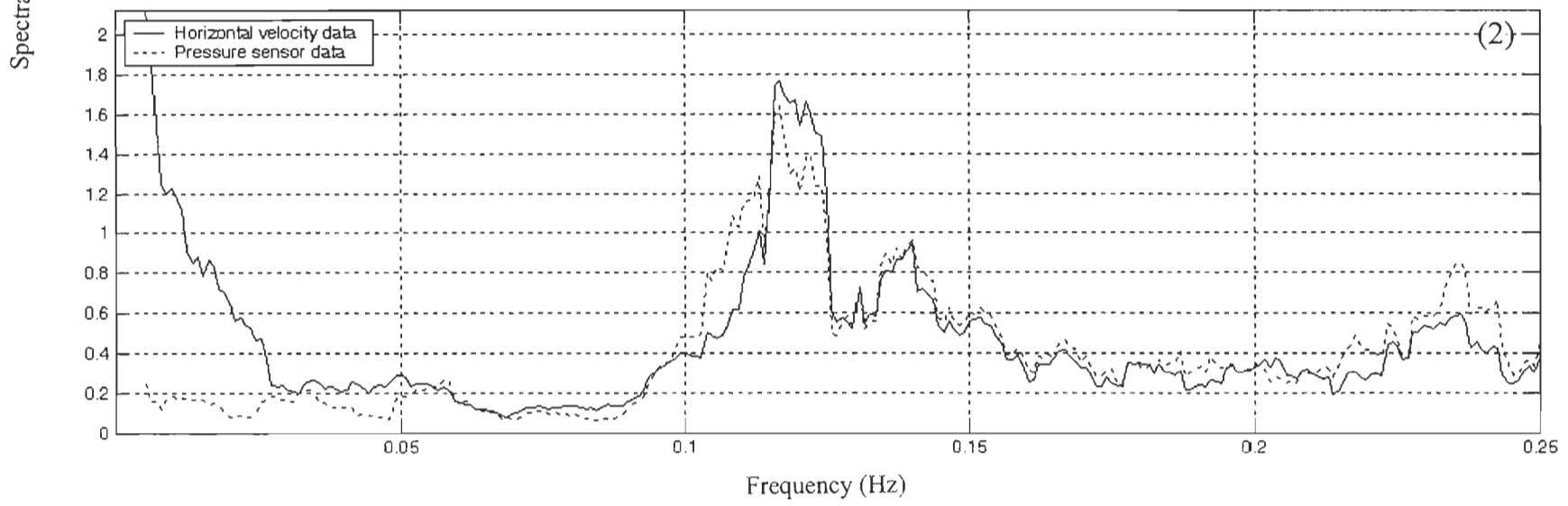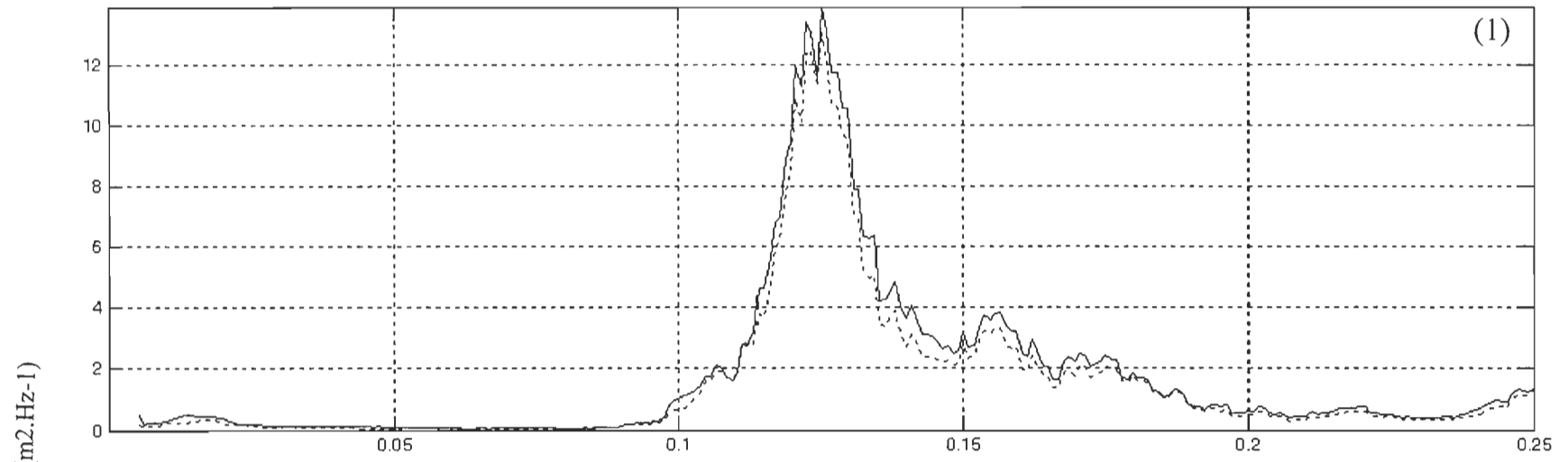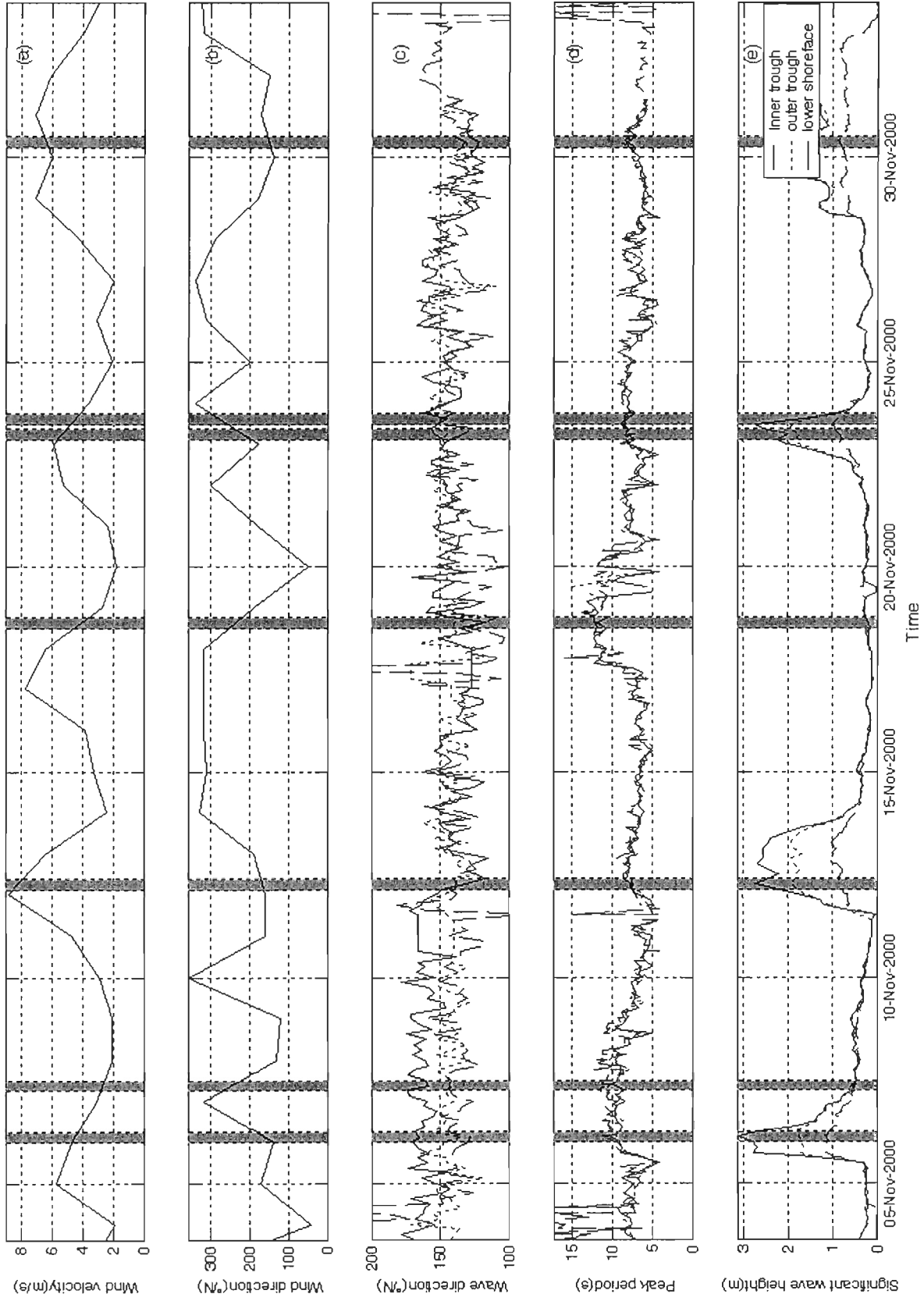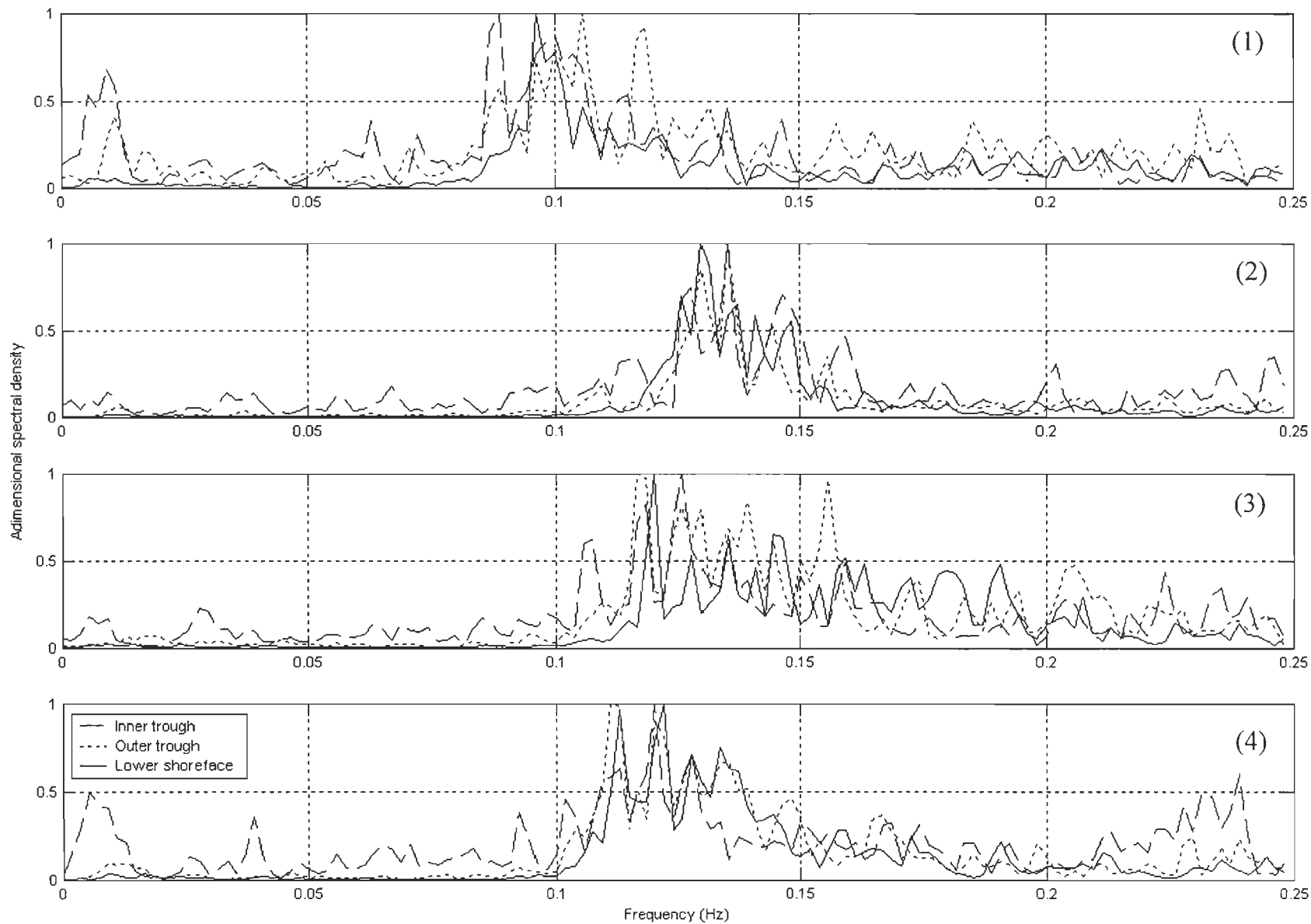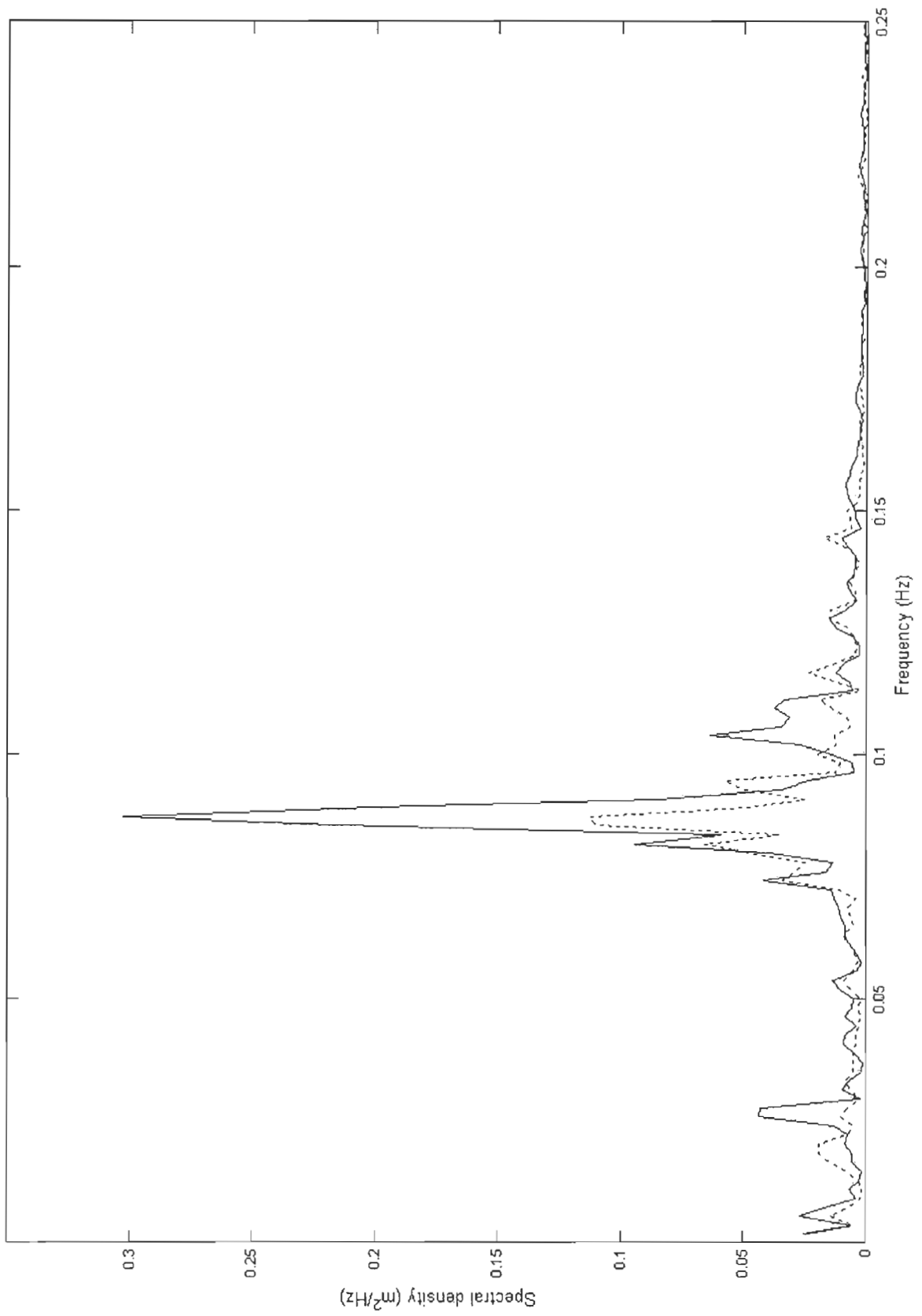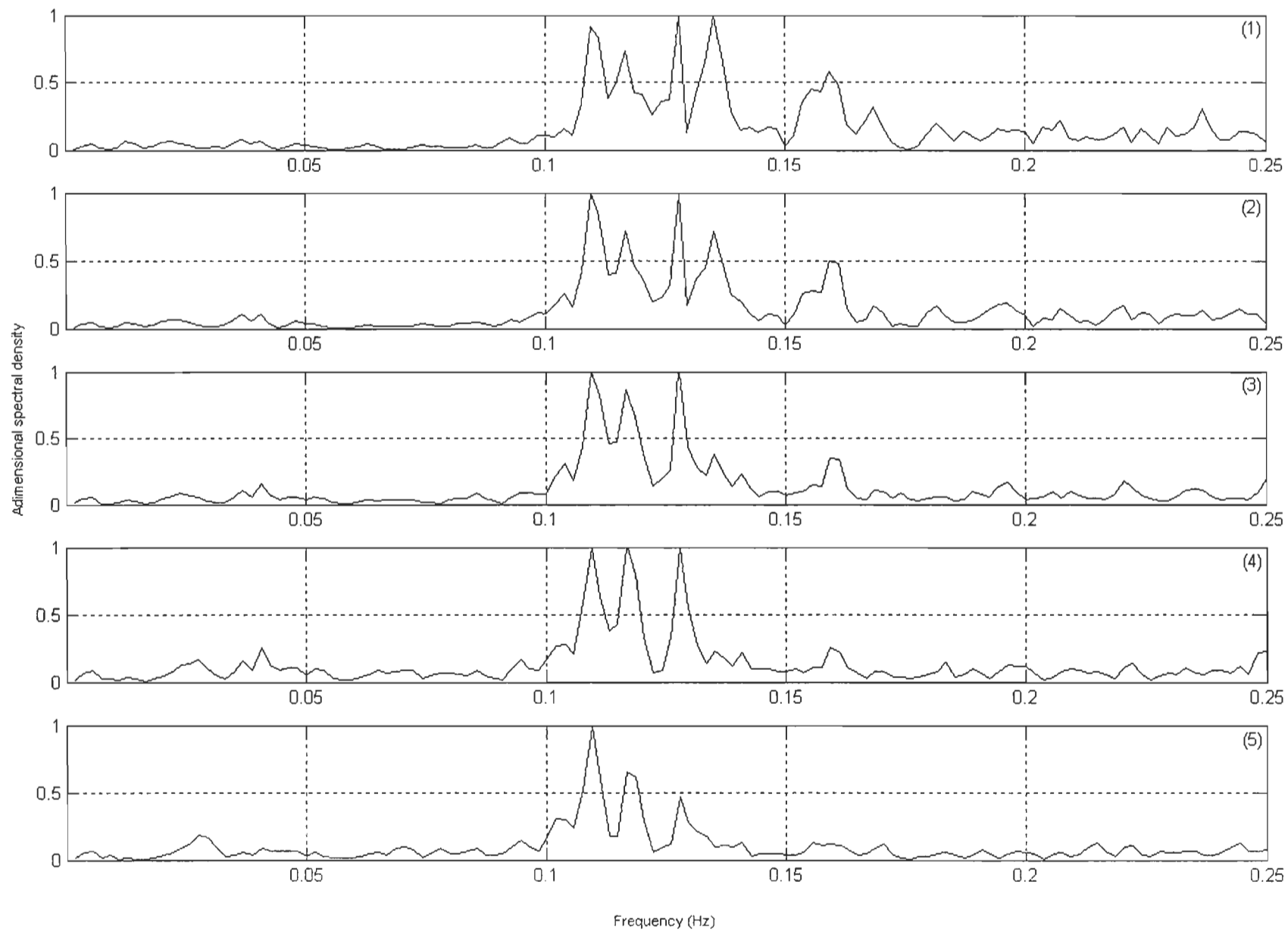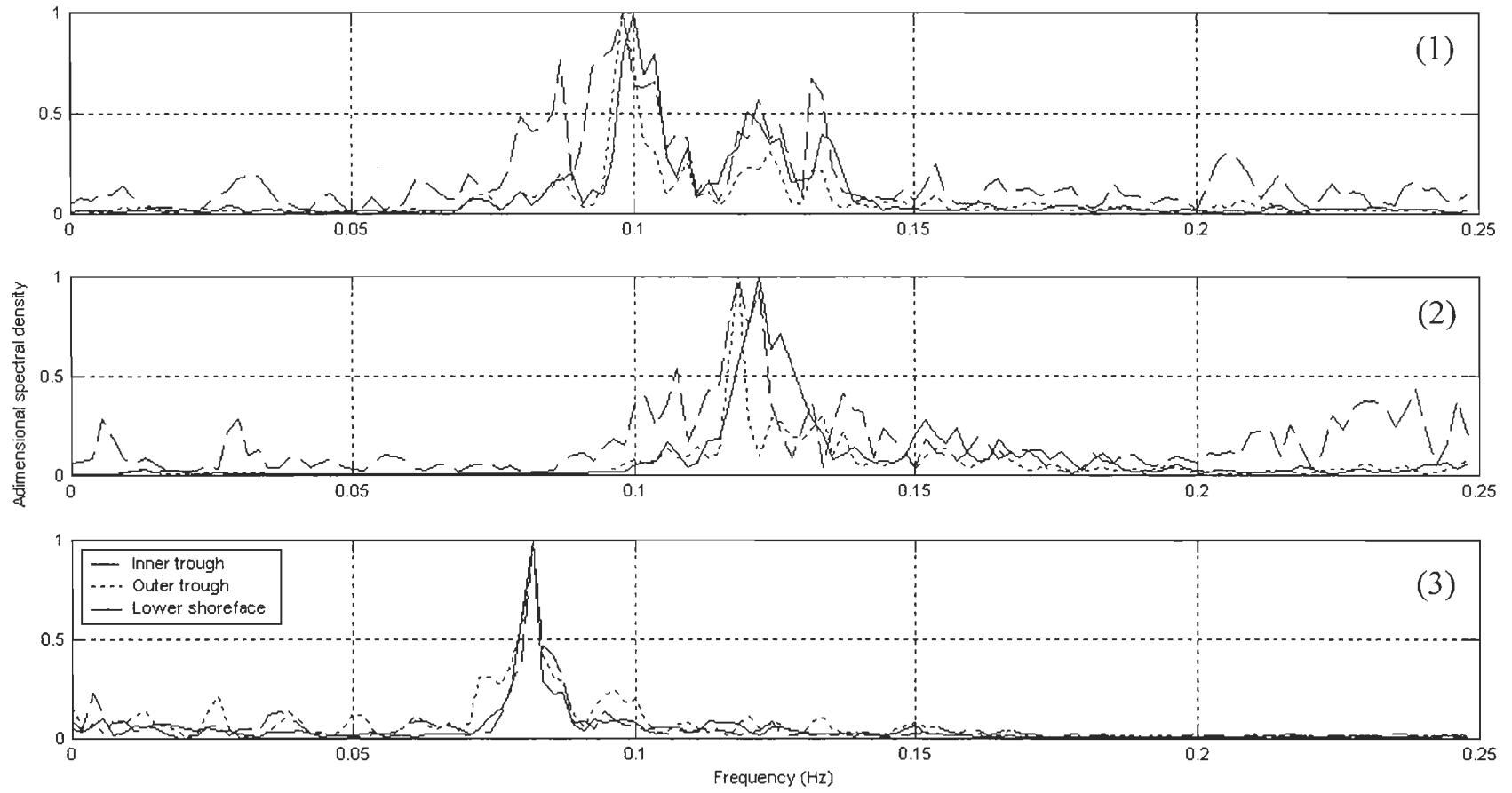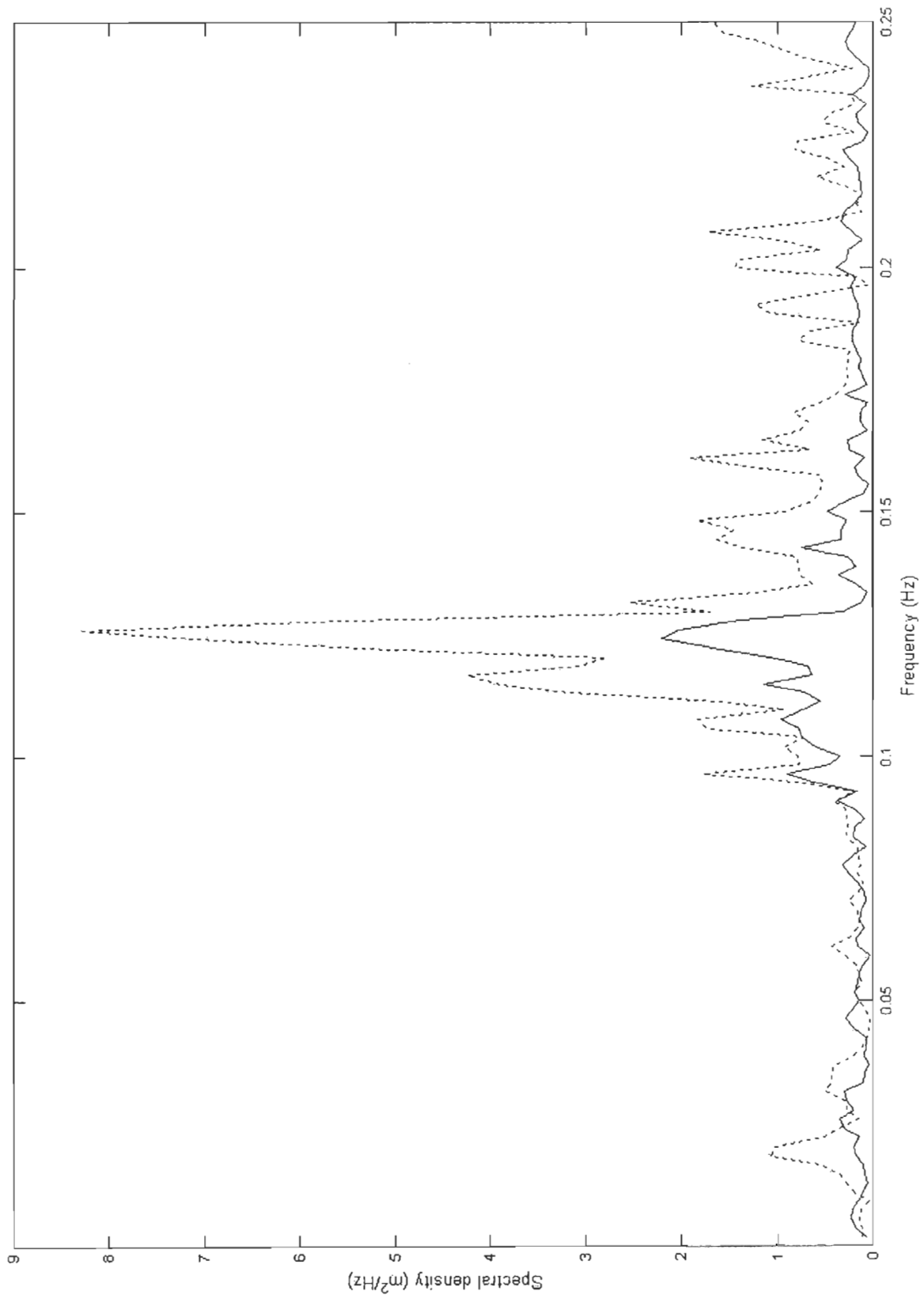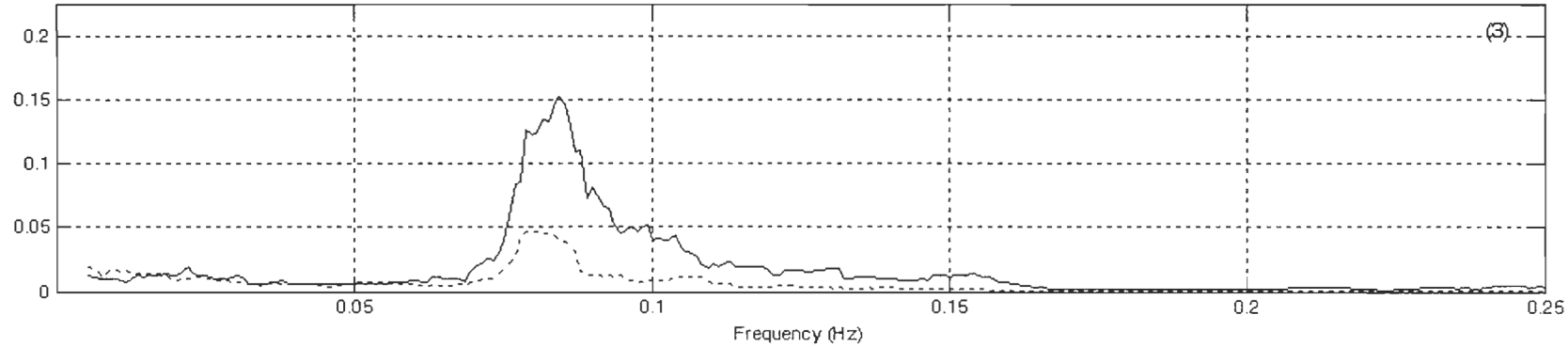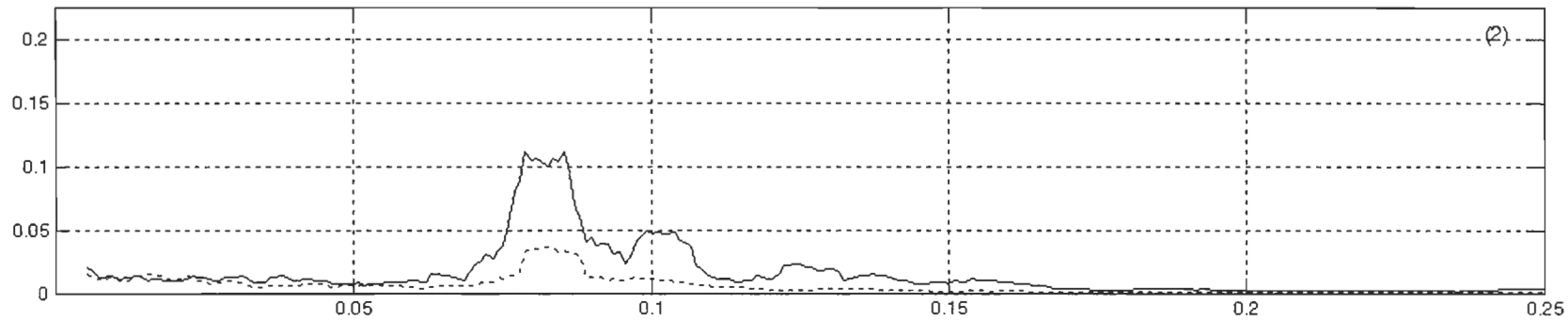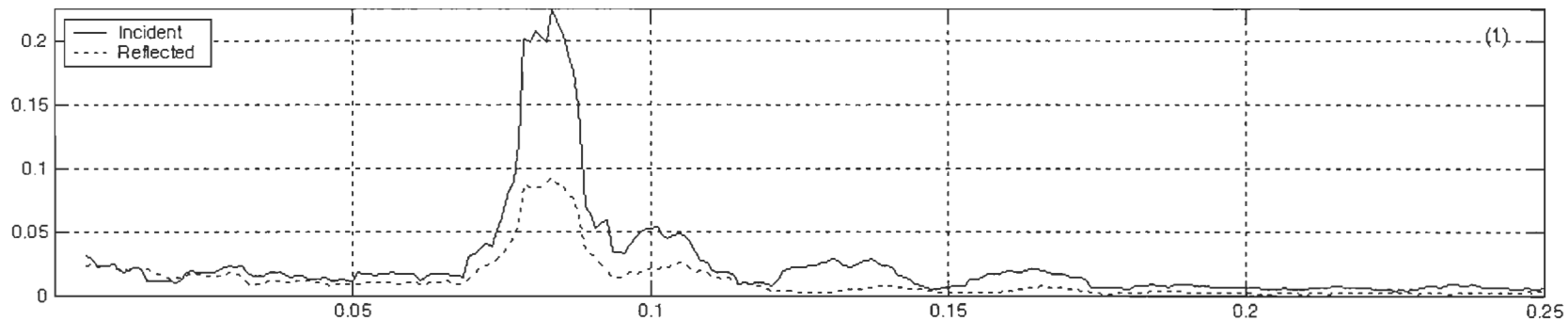
ANNEXE A4

MORPHODYNAMISME DE LA PLAGE DE SETE SOUS L'INCIDENCE DE

HOULE DE TEMPÊTE: EXPERIMENTATION ET MODELISATION

Samuel Meulé[1,2], Raphaël Certain[3], Christel Pinazo[1], Vincent Rey[4]

1: Université de la Méditerranée. Centre d'Océanologie de Marseille. Laboratoire d'Océanologie et de Biogéochimie. Station Marine d'Endoume (Bat 4)- UMR 6535. Rue de la batterie des Lions. F 13007 Marseille. France.
2: Université du Québec à Rimouski. Institut des Sciences de la Mer de Rimouski. 310 allée des Ursulines. Rimouski. Québec. G5L 3A1. Canada.
3: Université de Perpignan. Laboratoire d'Etude des Géo-Environnements Marins. LEGEM – EA. 52 av. de Villeneuve. F 66860 Perpignan.
4: Université de Toulon et du Var. L.S.E.E.T. - BP 132. F 83957 La Garde CEDEX

Le site de la plage de la Corniche à Sète est suivi depuis 1989 par l'Université de Perpignan dans le cadre du Programme National d'Environnement Côtier (Action de Recherche Thématique 7) (Certain, 2002; Certain *et al.*, 2003). Deux barres d'avant-côte sont présentes traduisant l'adaptation d'un fond sableux aux contraintes dynamiques. Les données analysées ici proviennent d'une ligne de 5 capteurs de pression et de 3 S4DW déployées lors de la campagne PNEC-ART7 du 3 novembre au 3 décembre 2000. L'analyse spectrale réalisée permet d'identifier sur l'ensemble de la campagne 4 tempêtes. L'objectif premier du travail présenté ici était de calibrer à partir de mesures effectuées sur le terrain, les paramètres de déferlement inhérents au modèle parabolique de propagation de la houle PARAB utilisé par le COM à Marseille (Meulé *et al.*, 2001). La houle déferle quand $H \geq \gamma h$, avec H la hauteur de la houle, h la hauteur de la colonne d'eau et γ le coefficient de déferlement (Battjes, 1974). Ce dernier est déterminé en fonction du type de déferlement (plongeant, glissant et frontal). L'effet de shoaling simulé par le modèle va légèrement augmenter la hauteur de houle jusqu'à son déferlement. Le modèle simule correctement le déferlement lors du pic de tempête au niveau du revers de la barre interne même lors de la présence d'ondes infragravitaires (fig. 1). Pour des conditions d'après - tempête et en présence d'ondes infragravitaires très énergétiques, le modèle est restreint et nous avons alors simulé la houle en forçant le rapport H/h à 0.5198, ce qui se rapproche des valeurs décrites par (Kroon, 1994). Ce travail a également permis d'obtenir une meilleure compréhension du rôle interactif joué par les barres dans la propagation d'ondes infragravitaires et de gravités, ainsi que le transfert d'énergie entre les différentes harmoniques lors du déferlement de la houle incidente.

Références

Battjes, J.A. (1974). *Surf similarity*. Proc 14th International Coastal Engineering Conference

Certain, R., Barusseau, J.-P., Levoy, F. et Monfort, O. (2003). *Morphodynamics of nearshore bars in the Golfe du Lion under swell obliquity*. Accepted with corrections in Journal of Coastal Research.

Certain , R. (2002). *Morphodynamique d'une côte sableuse microtidale à barres: le Golfe du Lion (Languedoc-Roussillon). PhD. Thesis,* Université de Perpignan: 1-209.

Kroon, A. (1994). *Sediment transport and morphodynamics of the beach and nearshore zone, near Egmond, The Netherlands. PhD. Thesis,* Faculteit Ruimtelijke Wetenschappen, Universiteit Utrecht: 1-274.

Meulé, S., Pinazo, C., Degiovanni, C., Barusseau, J.P. et Libes, M. (2001). *Numerical study of sedimentary impact of a storm on a sand beach simulated by hydrodynamic and sedimentary models*. Oceanologica Acta. 24(n°5): 1-8.
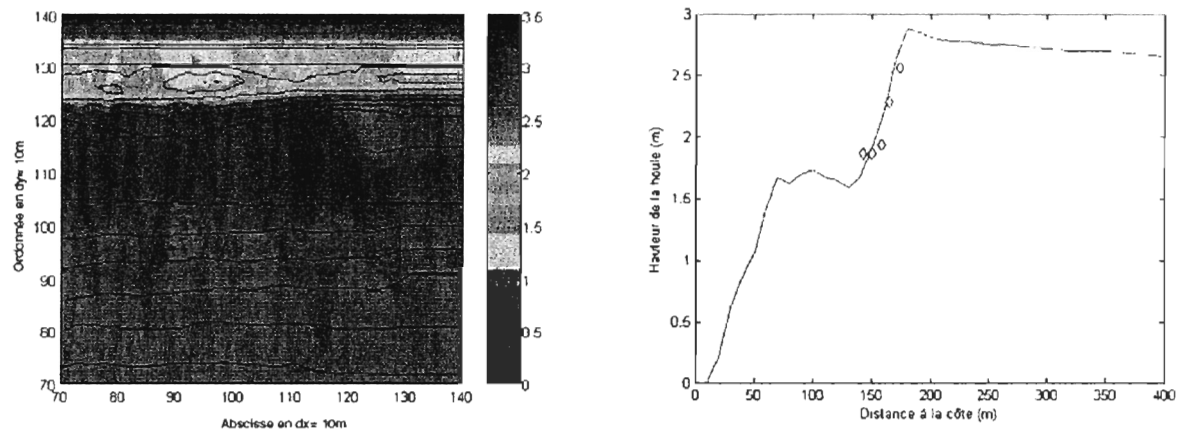
Figure 1 : A gauche, carte des hauteurs de houle (m) simulée par le modèle 2D parabolique de propagation de la houle. La bathymétrie du 16 Novembre 2000 a été surimposée en contour. A droite, surimposition du profil de hauteur de la houle en sortie du modèle(en trait continu) et des hauteurs significatives extraites de l'analyse spectrale des données prélevées par une ligne de 5 capteurs de pression (diamants).Cette ligne de capteurs était déployée au niveau de la barre interne.

RÉSUMÉ

Roberts Bank couvre le delta intertidal entre le bras principal du fleuve Fraser et la pointe du Cap Roberts en Colombie Britannique, Canada. Sous la pression du développement urbain et la modification du régime sédimentaire, cette plage de sable fin est soumise à une érosion significative. L'identification des forces hydrodynamiques, leur importance et leur interaction permettent de déterminer les zones de transport, et donc la stabilité de Roberts Bank. Deux périodes de mesures associées à des phases de modélisation de la houle et des courants ont été effectuées lors de ce travail. La première période de mesure, entre le 29 juin et le 8 juillet 2001, a permis l'identification de processus hydrodynamiques et sédimentaires associés aux forts courants de marée présents le long de Roberts Bank. La seconde phase de mesure, entre le 1er mars et le 26 mars 2002, a permis d'étudier les processus de remise en suspension associés à la houle. Des phases de modélisation ont été menées à partir des connaissances acquises sur le terrain, afin d'affiner la compréhension des processus sédimentaires et notamment les interactions houle - courant - sédiment. Les mécanismes, mis en évidence dans cette étude, participent au façonnage de Roberts Bank, contribuent à son érosion et à la mise en place de nouvelles structures sédimentaires. Les courants de flot de marée vont initier la création de nuages de resuspension de sédiment depuis le fond. En eau peu profonde, la composante "*onshore*" du courant de marée induit un transport à la côte, tandis qu'en eau plus profonde une faible composante "*offshore*" du courant peut favoriser un transport au large le long de la pente. Les chenaux, les dunes subaquatiques et les surfaces d'érosion affleurantes fournissent une rugosité de fond suffisante à la génération de turbulence et donc de nuages de sédiment en suspension. Lors de la marée de jusant, les sédiments resuspendus en eau peu profonde, sont transportés vers le large à partir d'un panache de surface et par les chenaux deltaïques. Une forte turbulence favorisera un processus dit de "sédimentation convective induite par un mélange turbulent " ("*mixing-induced convective sedimentation*"). Le comportement des vagues de tempête qui se propagent sur la partie supérieure de la pente du Delta du Fraser dépend du marnage, de l'incidence de propagation et de la morphologie sous-marine. Ces facteurs contrôlent une divergence dans le transport sédimentaire au niveau de la rupture de pente deltaïque. A marée haute, le transport sédimentaire sera essentiellement "*onshore*". Au contraire, à marée basse, le transport sédimentaire "*offshore*" est favorisé. La génération d'un "*set-up*" de tempête participe avec les courants de jusant à une remise en suspension et un transport "*offshore*". Ce phénomène est également associé aux courants d'arrachement générés par la propagation de la houle à la côte.